UNIVERSITY OF TURKU

VORTICES AND ARTIFICIAL DEFECTS IN HIGH-TEMPERATURE SUPERCONDUCTING THIN FILMS

Increasing the critical current densities via optimization of multilayer structures

Elmeri Rivasto

TURUN YLIOPISTON JULKAISUJA – ANNALES UNIVERSITATIS TURKUENSIS
PUBLICATION SERIES INFORMATION SHOULD GO HERE

University of Turku

Faculty of Science
Department of Physics and Astronomy
Physics
Doctoral Programme in Exact Sciences

Supervised by

Prof. Petriina Paturi
Wihuri Physical Laboratory
Department of Physics and Astronomy
University of Turku
Turku, Finland

Dr. Hannu Huhtinen
Wihuri Physical Laboratory
Department of Physics and Astronomy
University of Turku
Turku, Finland

Dr. Teemu Hynninen
Wihuri Physical Laboratory
Department of Physics and Astronomy
University of Turku
Turku, Finland

Reviewed by

Prof. Judy Wu
Department of Physics
University of Kansas
Lawrence, Missouri, USA

Prof. Nick Long
Robinson Research Institute
Victoria University of Wellington
Lower Hutt, Wellington, New Zealand

Opponent

Prof. Amit Goyal
Laboratory for Heteroepitaxial Growth of Functional Materials & Devices
Department of Chemical & Biological Engineering
State University of New York
Buffalo, New York, USA

The originality of this publication has been checked in accordance with the University of Turku quality assurance system using the Turnitin OriginalityCheck service.

ISBN 978-951-29-9308-6 (PRINT)
ISBN 978-951-29-9309-3 (PDF)
ISSN 0082-7002 (PRINT)
ISSN 2343-3175 (ONLINE)
Painosalama Oy, Turku, Finland, 2023

UNIVERSITY OF TURKU
Faculty of Science
Department of Physics and Astronomy
Physics
RIVASTO, ELMERI: Vortices and artificial defects in high-temperature superconducting thin films
Doctoral dissertation, 190 pp.
Doctoral Programme in Exact Sciences
March 2023

ABSTRACT

This dissertation studies the implications of vortex dynamics in high-temperature superconducting thin films. The combined use of both experimental and computational methods enabled one to draw otherwise unobtainable conclusions regarding the complex pinning mechanisms of the vortices. In particular, this enabled the study of zero field superconducting properties separately from the vortex dynamics governed high-field properties.

A particular interest was the study of vortex pinning within lattices of one-dimensional self-assembled columnar defects, typically referred to as nanorods. Several distinct pinning mechanisms were identified for given configurations of nanorods under specific magnetic environments. The presence of the different pinning mechanisms is manifested as perturbations in the experimentally measured critical current anisotropies. In addition, the limits of vortex pinning within increasingly dense nanorod lattices were rigorously studied.

After obtaining the general knowledge of how the interplay between the vortices and the artificial defects affect the superconducting properties of studied films, the study was focused to superconducting multilayer structures. There are several previous studies where an arbitrary multilayer structure has been associated with increased superconducting properties with respect to corresponding single layer films. Here, such study was repeated and the underlying mechanisms of the critical current improvement for multilayer structures were rigorously studied.

Finally, the optimization of the multilayer structures for specific temperature and field ranges was considered. Firstly, the layer thicknesses within a simplistic bilayer film was optimized based on a theoretical model. After this, in order to efficiently address more broad-scale optimization of the multilayer structures, a new approach taking advantage of state-of-the-art artificial intelligence models is proposed. A set of rigorous experiments is suggested to reliably validate the presented theoretical predictions considering the properties of an optimal multilayer structure.

KEYWORDS: High-temperature superconductor, vortex, artificial pinning center, multilayer thin film

TURUN YLIOPISTO
Matemaattis-luonnontieteellinen tiedekunta
Fysiikan ja tähtitieteen laitos
Fysiikka
RIVASTO, ELMERI: Vortices and artificial defects in high-temperature superconducting thin films
Väitöskirja, 190 s.
Eksaktien tieteiden tohtoriohjelma
Maaliskuu 2023

TIIVISTELMÄ

Tässä väitöskirjassa tutkittiin vorteksidynamiikan seurauksia korkean lämpötilan suprajohtavissa ohutkalvoissa. Kokeellisten ja laskennallisten menetelmien samanaikainen käyttö mahdollisti muuten saavuttamattomien johtopäätösten tekemisen vorteksien lukkiutumismekanismeista. Tämä mahdollisti erityisesti suprajohteen nollakentän ominaisuuksien tutkimisen erillään vorteksidynamiikan määrittelemistä korkean kentän ominaisuuksista.

Erityinen mielenkiinnon kohde on ollut vorteksien lukkiutumisen tutkiminen yksiulotteisten itserakantuvien kolumnaaristen defektien hilassa, joita kutsutaan tyypillisesti nano-kolumneiksi (engl. nanorods). Työssä tunnistettiin useita eri lukkiutumismekanismeja eri eri nano-kolumnien konfiguraatioilla ja magneettikentissä. Erilaisten lukkiutumismekanismien läsnäolo ilmenee eroina kokeellisesti mitatuissa kriittisen virran anisotropioissa. Tämän lisäksi, vorteksien lukkiutumisen rajoja tutkittiin perusteellisesti suurilla nano-kolumnien hilojen tiheyksillä.

Kun yleinen ymmärrys vorteksien ja nano-kolumnien välisen vuorovaikutuksen seurauksista tutkittujen kalvojen suprajohtaviin ominaisuuksiin oli saavutettu, mielenkiinto suunnattiin suprajohtaviin monikerrosrakenteisiin. Useissa aikaisemmassa tutkimuksissa mielivaltaisten monikerrosrakenteiden suprajohtavien ominaisuuksien on havaittu olevan parempia suhteessa suhteessa vastaaviin yksikerroskalvoihin. Tässä työssä samankaltainen tutkimus on toistettu ja monikerrosrakenteiden kohentuneen kriittisen virran taustalla olevia mekanismeja on kokonaisvaltaisesti tutkittu.

Lopuksi käsiteltiin monikerrosrakenteiden optimointia tietylle lämpötila- ja kenttäalueille. Ensin optimoitiin yksinkertaisen kaksikerrosrakenteen kerrospaksuudet teoreettista mallia hyödyntäen, minkä jälkeen ehdotetaan uutta tekoälymalleja hyödyntävää lähestymistapaa käytettäväksi laaja-alaiseen ja tehokkaaseen monikerrosrakenteiden optimointiin. Ehdotan myös kokeita todentamaan teoreettiset ennusteet optimaalisten monikerrosrakenteiden ominaisuuksista.

ASIASANAT: Korkean lämpötilan suprajohde, vorteksi, synteettinen lukkiutumiskeskus, monikerrosohutkalvo

Acknowledgements

I am honored for having the distinguished Professor Amit Goyal as my opponent. Thank you also for Prof. Judy Wu and Prof. Nick Long for reviewing my thesis and providing me with constructive feedback.

I wish to thank all of my supervisors for the priceless skills and knowledge that I have acquired during my studies. I thank Prof. Petriina Paturi for providing an environment that has supported my innovative thinking. I am grateful for having Dr. Hannu Huhtinen as my closest supervisor in daily research as he has provided me with precious advice related to both life and research. Thank you also to Dr. Teemu Hynninen for his professional advice and support on computational problems that I faced during my studies.

I wish to thank my parents for providing me with the upbringing that has solely led me to where I am today. I am extremely grateful for my beloved wife who has provided me with care and support. Thank you to all of my friends and colleagues for the fun times in and out of the office. You have all been a valued part of my journey and I will never forget the experienced good times at Wihuri!

The research associated with this thesis was done between the years 2018–2022 at the Wihuri Physical Laboratory in University of Turku. I acknowledge financial support for the Doctoral Program of University of Turku Graduate School along with the generous Jenny and Antti Wihuri Foundation. The computer resources required by the studies within this thesis were provided by the Finnish IT Center for Science and the FGCI project (Finland).

8.1.2023
Elmeri Rivasto

Table of Contents

Abbreviations

AI	Artificial Intelligence
APC	Artificial Pinning Center
BHO	$BaHfO_3$
BSO	$BaSnO_3$
BZO	$BaZrO_3$
GBDT	Gradient Boosted Decision Tree
GL	Ginzburg-Landau
HP	Hyperparameter
HTS	High-Temperature Superconductor
MD	Molecular Dynamics
ML	Multilayer
PLD	Pulsed Laser Deposition
(BF-)TEM	(Bright-Field-) Transmission Electron Microscopy
XRD	X-Ray Diffraction
YBCO	$YBa_2Cu_3O_{6+x}$
λ	Magnetic penetration depth
ξ	Superconducting coherence length
ψ	Order parameter
J_c	General critical current density
$J_\mathrm{c,v}$	Vortex dynamics limited critical current density
$J_\mathrm{c,0}$	Zero field critical current density
B	Magnetic field
R	Nanorod radius
P_pin	Pinning probability of a vortex
P_cross	Crossing probability between vortex and pinning site

List of Original Publications

This dissertation is based on the following original publications, which are referred to in the text by their Roman numerals:

I E. Rivasto, M. Z. Khan, M. Malmivirta, H. Rijckaert, M. M. Aye, T. Hynninen, H. Huhtinen, I. Van Driessche and P. Paturi, Self-assembled nanorods in YBCO matrix – a computational study of their effects on critical current anisotropy, Scientific Reports, 2020; 10, 3169

II M. M. Aye, E. Rivasto, M. Z. Khan, H. Rijckaert, H. Palonen, H. Huhtinen, I. Van Driessche and P. Paturi, Multilayering BZO nanocolumns with different defect densities for YBCO high field applications, New Journal of Physics, 2021; 23, 113031

III M. M. Aye, E. Rivasto, H. Rijckaert, H. Palonen, H. Huhtinen, I. Van Driessche and P. Paturi, Optimized $BaZrO_3$ nanorod density in $YBa_2Cu_3O_{6+x}$ matrix for high field applications, Superconductor Science and Technology, 2022; 35, 075006

IV E. Rivasto, H. Huhtinen, T. Hynninen and P. Paturi, Vortex dynamics simulation for pinning structure optimization in the applications of high-temperature superconductors, Journal of Physics: Condensed Matter, 2022; 34, 235902

V E. Rivasto, T. Hynninen, H. Huhtinen and P. Paturi, Optimization of high-temperature superconducting bilayer structures using a vortex dynamics simulation, Journal of Physics: Condensed Matter, 2023; 35, 075701

VI E. Rivasto, M. Todorović, H. Huhtinen, and P. Paturi, Optimization of high-temperature superconducting multilayer films using artificial intelligence, New Journal of Physics (submitted)

Articles relevant to this work but not included in the thesis

VII M. M. Aye, M. Z. Khan, E. Rivasto, J. Tikkanen, H. Huhtinen and P. Paturi, Role of columnar defects size on angular dependent flux pinning properties in YBCO thin films, IEEE Transactions on Applied Superconductivity, 2019; 29, 8000805

VIII M. Z. Khan, E. Rivasto, J. Tikkanen, H. Rijckaert, M. Malmivirta, M.O. Liedke, M. Butterling, A. Wagner, H. Huhtinen, I. Van Driessche and

P. Paturi, Enhanced flux pinning isotropy by tuned nanosized defect network in superconducting $YBa_2Cu_3O_{6+x}$ films, Scientific Reports, 2019; 9, 15425

IX M.Z. Khan, E. Rivasto, Y. Wu, Y. Zhao, C. Chen, J. Zhu, H. Palonen, J. Tikkanen, H. Huhtinen, P. Paturi, Modifying the critical current anisotropy of YBCO films via buffering layers on IBAD-MgO based templates, Journal of Physics: Conference Series, 2020; 1559, 012037

X E. Rivasto, M. Z. Khan, Y. Wu, Y. Zhao, C. Chen, J. Zhu, H. Huhtinen, P. Paturi, Lattice defect induced nanorod growth in YBCO films on an advanced IBAD-MgO template, Superconductor Science and Technology, 2020; 33, 075008

XI A. Beiranvand, E. Rivasto, H. Huhtinen and P. Paturi, Strain-induced domain structure and its impact on magnetic and transport properties of $Gd_{0.6}Ca_{0.4}MnO_3$ thin films, ACS Omega, 2021; 6, 34572–34579

XII M. M. Aye, E. Rivasto, M. Z. Khan, H. Rijckaert, E. Salojärvi, C. Haalisto, E. Mäkilä, H. Palonen, H. Huhtinen, I. Van Driessche and P. Paturi, Control of the nanosized defect network in superconducting thin films by target grain size, Scientific Reports, 2021; 11, 6010

XIII E. Rivasto, J. Kim, L. M. Tien, J-H. Kang, S. Park, W. S. Choi, W. N. Kang and T. Park, Growth optimization of $CeCoIn_5$ thin films via pulsed laser deposition, Progress in Superconductivity and Cryogenics, 2021; 23, 3

XIV M. Z. Khan, E. Rivasto, H. Rijckaert, Y. Zhao, M. O. Liedke, M. Butterling, A. Wagner, I. Van Driessche, H. Huhtinen and P. Paturi, Strongly enhanced growth of high-temperature superconducting films on an advanced metallic template, Crystal Growth and Design, 2022; 22, 2097–2104

XV M. M. Aye, E. Rivasto, H. Rijckaert, S. Granroth, H. Palonen, H. Huhtinen, I. Van Driessche and P. Paturi, Role of Deposition Distance on Nanorod Growth and Flux Pinning in BZO Doped YBCO Thin Films: Implications for Superconducting Tapes, Applied Nano Materials, 2022; 5, 18159–18167

XVI M. M. Aye, E. Rivasto, T. Vaimala, Y. Zhao, H. Huhtinen and P. Paturi, Improved crystalline quality and self-field J_c in sequentially multilayered YBCO thin films on buffered metallic templates, IEEE Transactions on Applied Superconductivity, 2023; 33, 1-6

1 Motivation

The HTS materials have been of great interest for both fundamental and application driven research ever since their discovery in 1986 [1; 2]. This results from the possibility to obtain a superconducting state via easily accessible liquid nitrogen cooling along with the exceptional tolerance for external magnetic fields. Unfortunately, the characteristic brittle ceramic structure of the HTS materials have turned out to be a major challenge for the manufacture of HTS-cables required for practical usage. Moreover, the magnetic vortex induced power losses have prevented the large-scale use of the HTS materials, in particular for applications operating under high magnetic fields.

Only during the past decade, commercial applications of the HTS materials have started appearing in increasing extent [3]. This has been enabled by the long lasting development of coated conductor technology along with the advances in vortex pinning via introduction of APCs within the HTS lattice [4; 5; 3; 6; 7]. In particular, the discovery of self-assembled nanorods is seen as the major single advance in the field of HTS films [8; 9; 10]. The associated progress has extended the applicability of HTS materials into higher field ranges, most prominently required for HTS magnets desired to be used in state-of-the-art fusion reactors [11; 12]. Furthermore, the developments in the deposition of high quality HTS thin films has increased their potential as candidates for several microwave applications associated with quantum technology and search for dark matter [13; 14].

Due to the large number of applications operating under very different environments, the superconducting properties of the applied HTS films evidently need to be tuned for the operation field and temperature associated with the application. As a general rule, increasing the size and density of the APCs increases the current carrying capability of the HTS film under high-field range via enhanced vortex pinning [6]. However, the zero field intrinsic superconducting properties are simultaneously decreased. Thus, the fine tuning of the superconducting properties can be done by adjusting the APC morphology accordingly. As a consequence, particularly extensive research has been done on the engineering of the nanorod lattices [4]. To date, the processes governing the nanorod formation within the HTS lattice are fairly well understood which has resulted in possibilities to individually vary the nanorod diameter, length and areal density to a relatively good extent [15; 16; 17; 4].

The pinning mechanisms of the vortices into various intrinsic and artificial de-

fects have been theoretically investigated in [18; 19; 20; 21; 22; 23] among many other studies. These models are able to explain several experimentally observed features in particular for critical current anisotropy curves [24; 25; 26; 27; 28; 29]. However, these rigorous models correspond to highly idealized situations and are difficult, if not impossible, to generalize for different field ranges and complex pinning structures. In particular, these models are ineffective for addressing the vortex pinning within complex APC morphologies associated with the emerging HTS ML films. For such systems, a more generalized pinning model is required. Such a general model of pinning is evidently prone to be rather qualitative and lack mathematical accuracy, but could enable the efficient design of APC morphologies for specific magnetic environment.

We consider the ML structures to be the next generation of the HTS coated conductors. There is strong evidence that ML structures could increase the overall current carrying capability of the HTS conductors as several arbitrary ML structures have provided improved superconducting properties when compared with single layer films even without any systematic optimization of APC morphology within the associated structures [30; 31; 32; 33; 34]. Thus, a rigorously optimized ML structure can be expected to improve the superconducting properties significantly. This is in particular under mid-field range, that is roughly between 0.1–2 T, where the effects of both zero-field superconducting properties and vortex pinning efficiency plays a major role.

Finding the optimal ML solution for a given environment is extremely difficult task due to extensive number of possible APC morphologies and associated layer thicknesses which results in practically infinite search space. Thus, the broad-scale optimization of the HTS ML structures has to be addressed using new theoretical and computational methods that balance between physical accuracy and computational efficiency. Since the ML structures are the most viable way to significantly increase the performance of the HTS film, the development of such computational methods that could be used for efficient on-demand ML structure optimization is of great importance.

2 Introduction

2.1 General aspects of superconductivity

Superconductivity is one of the few known macroscopic quantum phenomena, which is manifested in various materials as zero resistance and perfect diamagnetism below critical state parameters. These parameters include critical temperature (T_c), magnetic field (B_c) and current density (J_c). The superconducting state emerges as the electrons form pairs that are able to condense into the lowest energy state where a sufficiently high energy gap prevents their scattering from impurities [2].

The superconductors can be divided into two distinct classes, generally referred to as type-I and type-II superconductors. The type-I superconductors are typically simple materials, such as pure metals, with very low T_c. The type-II superconductors, on the other hand, have typically more complex structures and they are associated with significantly higher T_cs when compared with type-I superconductors. However, the main difference between the two types of superconductors is illustrated in the T-B-phase diagrams presented in Figure 1a–b. As the temperature and field is lowered below their associated T_cs and B_cs, the type-I superconductors shift from normal to so called Meissner state in which the applied magnetic field is completely excluded from the interior of the superconductor. For the type-II superconductors, however, there exist two distinct critical magnetic fields, that are the lower critical field ($B_{\mathrm{c}1}$) and the upper critical field ($B_{\mathrm{c}2}$). Below the $B_{\mathrm{c}1}$, the type-II superconductors behave similarly to type-I as they are in the Meissner state. The key difference comes apparent between the $B_{\mathrm{c}1}$ and $B_{\mathrm{c}2}$, where the so called mixed state emerges. In the

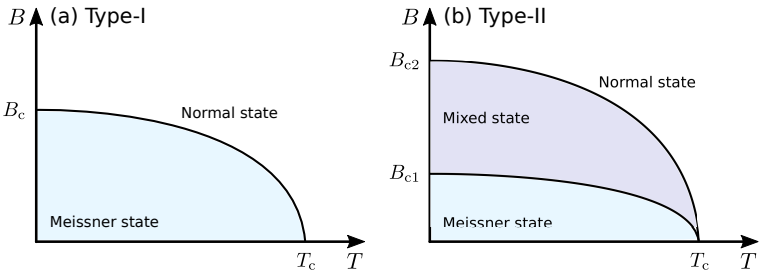

Figure 1. Schematic illustrations of the temperature-magnetic field phase diagrams for (a) type-I and (b) type-II superconductors.

mixed state, the magnetic field penetrates the superconductor as discrete magnetic flux tubes, typically called vortices, each of which is associated by a magnetic flux equal to a single flux quantum $\Phi_0 \approx 2.067 \cdot 10^{-15}$ Wb [2].

An important subclass of the type-II superconductors are the so-called high-temperature superconductors (HTS), that are characterized with overwhelmingly high T_cs well above liquid nitrogen temperature (77 K). Moreover, HTS materials are associated with practically unreachable $B_{\mathrm{c}2}$ [35]. Contrary to the other low-temperature superconductors, the HTS materials are still lacking a solid theoretical foundation. Despite the absence of microscopical quantum mechanics based theory, the HTS materials have been ever widely studied in particular from a practical point of view. The HTS materials indeed enable several applications with both commercial and scientific potential. One of the most widely studied HTS material is $YBa_2Cu_3O_{6+x}$ (YBCO), which has also been the main interest of this thesis.

2.2 Theoretical aspects of superconductivity

While the HTS materials are still lacking microscopic quantum theory, their general behaviour, among other superconductors, can be well understood by the phenomenological Ginzburg-Landau (GL) theory [36]. The GL theory is based on the assumption that near the transition temperature Gibbs energy density can be written as [2; 37]

$$\begin{aligned} G =& G_0 + \frac{1}{V}\int dV \frac{1}{2m}(-i\hbar\nabla + q\mathbf{A})\psi^* \cdot (i\hbar\nabla + q\mathbf{A})\psi + \frac{\nabla^2\mathbf{A}^2}{2\mu_0} \\ &+ a\psi\psi^* + \frac{1}{2}b\psi\psi^*\psi\psi^* + ..., \end{aligned} \tag{1}$$

where i is the imaginary unit, $\mathbf{A}$ is the magnetic vector potential defined as $\mathbf{B} = \nabla\times\mathbf{A}$ and $a = a(T)$ and b are phenomenological parameters. Most importantly, $\psi = \psi(\mathbf{r})$ is the complex order parameter that resembles the collective quantum mechanical wave function of the paired electrons. Thus, the ansatz for the order parameter is generally written as $\psi(\mathbf{r}) = \psi_0(\mathbf{r}) \cdot \mathrm{e}^{i\theta(\mathbf{r})}$, where θ is the phase of the wave function. It is further assumed that $|\psi(\mathbf{r})|^2$ equals to the carrier density, which in this case evidently refers to the density of the electron pairs.

By varying the integrand of Eq. (1) with respect to ψ^* and $\mathbf{A}$, one obtains a system of two differential equations [2; 37]

$$\begin{cases} \frac{1}{2m}\left(\hbar^2\nabla^2\psi - 2i\hbar q\mathbf{A}\cdot\nabla\psi - q^2\mathbf{A}^2\psi\right) - a\psi - b|\psi|^2\psi = 0 \\ \mu_0\mathbf{J} = -\frac{i\hbar q}{2m}\left(\psi^*\nabla\psi - \psi\nabla\psi^*\right) - \frac{q^2}{m}\mathbf{A}|\psi|^2 \end{cases}, \tag{2}$$

referred as the GL-equations for energy and current, respectively. These equations can be further solved to quantitatively understand various properties of the superconductors using different initial conditions corresponding to specific situations.

An important solution of the GL-equations is obtained when considering a superconductor under a homogenous magnetic field. Assuming that the order parameter remains constant within the superconductor, that is $\nabla\psi(\mathbf{r}) = 0$, the GL equation for current can be solved for the vector potential resulting in $A_y(x) = A_0 \exp(-x/\lambda)$. Here, we have abbreviated $\lambda = \sqrt{m/\mu_0 q^2|\psi|^2}$ and defined it as the magnetic *penetration depth* [2]. The physical interpretation of λ comes clear when looking at the obtained solution, that is λ determines the distance up to which the applied magnetic field can penetrate into the superconductor. The λ is one of two characteristic lengths of a superconductor.

Another important solution of the GL-equations is obtained under zero field. Inserting $\mathbf{A} = 0$ to the GL equation for current one can deduce that ψ has to be a real-valued. It follows, that the GL equation for energy has a 1-dimensional solution $\psi(x) = \sqrt{|a|/b}\tanh(x/\xi\sqrt{2})$, where $\xi = \hbar/\sqrt{2m|a|}$ [2]. Here, the ξ is the defined as the superconducting *coherence length*, that is considered as the other characteristic length of the superconductor. By looking at the associated solution, ξ determines the length scale over which the value of the order parameter can vary significantly.

The importance of the above introduced characteristic length scales of a superconductor becomes apparent as it can be shown that their ratio, $\kappa = \lambda/\xi$, determines the type of the superconductor. In particular, if $\kappa < 1/\sqrt{2}$ the superconductor is type-I and if $\kappa > 1/\sqrt{2}$ the superconductor is type-II [2].

2.2.1 Vortices

In the mixed state of type-II superconductors, the magnetic field penetrates through the superconducting material in the form of quantized vortices [38]. The existence of the vortices can be deduced from the the GL-equations by considering uniform carrier density concentration, that is by setting $\nabla\psi_0(\mathbf{r}) = 0$. This time, however, we allow the phase θ of the wave function $\psi(\mathbf{r}) = \psi_0(\mathbf{r}) \cdot \mathrm{e}^{i\theta(\mathbf{r})}$ to vary with respect to position. Inserting this wave function to the GL-equation for current under the given assumptions and taking a line integral from both sides of the equation one obtains [2; 37]

$$\frac{\mu_0 m}{q^2|\psi|^2}\oint \mathbf{J}d\mathbf{l} + \oint \mathbf{A}d\mathbf{l} = \frac{\hbar}{q}\oint \nabla\theta d\mathbf{l}\,. \tag{3}$$

According to well know result, a closed line integral of the phase of a quantum mechanical wave function has to equal to an integer multiple of 2π [37]. The right hand side of Eq. (3) can be thus written with the help of magnetic flux quantum ($\Phi_0 = h/q$) as $n\Phi_0$, where $n \in \mathbb{Z}$. This suggests that the left hand side of Eq. (3), that is the magnetic flux through the superconductor, is quantized. As the energy of the magnetic field is proportional to B^2, it is evident that the field penetrates the superconductor by forming maximum number of individual flux quanta equal to Φ_0. It is these flux quanta we refer to as vortices.

The Eq. (3) can be further used to study the magnetic field profile of a single vortex. Consider a vortex at the center of cylindrical coordinate system and assume that the associated magnetic field is oriented perpendicular to the r-coordinate. We further assume that the superconductor is in normal state for $r < \xi$, that is considered as the core of the vortex. As we have previously shown that the magnetic field decays exponentially when moving from normal to superconducting region, one can further assume that $B(r) \to 0$ as $r \to \infty$. With the given assumptions, the line integrals become easy to solve and after some vector algebra one results in a well known Helmholtz equation

$$\mathbf{B} = \lambda^2 \nabla^2 \mathbf{B}\,. \tag{4}$$

Solving Eq. (4) in cylindrical coordinate system for $B(r)$ one obtains [37]

$$B(r) = \frac{n\Phi_0}{2\pi\lambda^2} \cdot \begin{cases} \mathrm{K}_0\left(\frac{\xi}{\lambda}\right), & \text{when } \; r < \xi \\ \mathrm{K}_0\left(\frac{r}{\lambda}\right), & \text{when } \; r \geq \xi \end{cases} \tag{5}$$

where K_0 is the zeroth-order modified Bessel function that describes the field profile of a vortex.

2.2.2 Vortex interactions

It is rather obvious that two vortices repel each other as we have previously deduced that their individual number has to be maximized. The interaction potential can be rigorously derived by considering the formula for energy per unit length [37]

$$\epsilon = \frac{1}{2\mu_0} \int_S \mathbf{B} \cdot \mathbf{V} dS + \frac{1}{2\mu_0} \int_C \mathbf{B} \times \mathbf{J} \cdot d\mathbf{l}, \tag{6}$$

where $\mathbf{V} = \mathbf{B} + \nabla \times \mathbf{J}$ is defined as the vorticity. In Eq. (6), the surface S is parallel to $\mathbf{B}$ and the line C is the associated contour. With the help of Maxwell's equations and vector calculus identities, Eq. (6) can be converted back to the classical volume integral for field energy. The convenience in defining the vorticity comes apparent as, with the help of Eq. (3), it can be shown that for a vortex located at $\mathbf{r}'$ one can write $\mathbf{V}(\mathbf{r}) = n\Phi_0\delta(\mathbf{r} - \mathbf{r}')$, where δ is the Dirac delta function. As the surface S is arbitrary, the line integral in Eq. (6) can be neglected and the energy per unit length can be easily solved by simply inserting the sum fields of a vortex ensemble according to Eq. (5) to the surface integral. For a system of two vortices, this results in [37; 2]

$$\epsilon(r) = \frac{\Phi_0^2}{2\pi\mu_0\lambda^2} K_0\left(\frac{\xi}{\lambda}\right) + \frac{\Phi_0^2}{2\pi\mu_0\lambda^2} K_0\left(\frac{r}{\lambda}\right). \tag{7}$$

The latter term of Eq. (7) can be interpreted as the interaction energy between two vortices [37; 39]. As the vortices try to minimize the total energy by maximizing the distances between them, they are ideally expected to form a symmetric vortex lattice.

As an external current ($\mathbf{J}_{\mathrm{ext}}$) is applied through the superconductor, the vortices experience the classical Lorentz force

$$\mathbf{f}_{\mathrm{L}} = \mathbf{J}_{\mathrm{ext}} \times \hat{\Phi}_0, \tag{8}$$

that drives the vortices in motion. Unfortunately, the motion of the vortices creates power loss in the superconductor according to the famous Faraday's induction law. Thus, despite the existence of the superconducting state, by applying a current through the superconductor one is prone to obtain vortex motion induced power losses, the magnitude of which increases as a function of the applied magnetic field.

The vortices also experience an attractive interaction towards any type of lattice defects in the vicinity of which superconductivity is suppressed. This can be easily deduced from Eq. (6), by separating the surface (or generally volume) integral into parts corresponding to superconducting (V_{sc}) and defect regions (V_{df}) resulting in the following magnetic field energy

$$E = \frac{1}{2\mu_{\mathrm{sc}}} \int_{V_{\mathrm{sc}}} \mathbf{B}^2 dV + \frac{1}{2\mu_{\mathrm{df}}} \int_{V_{\mathrm{df}}} \mathbf{B}^2 dV\,. \tag{9}$$

As the superconductivity is suppressed inside V_{df}, we can assume that $\mu_{\mathrm{df}} > \mu_{\mathrm{sc}}$. Thus, it is apparent that the energy is minimized when the field of the vortex within V_{df} is maximized. This implies attractive interaction between vortices and lattice defects. The commonly used formula for the vortex-defect interaction energy per unit length as a function of their separation is given by [21; 40; 29]

$$\epsilon_{\mathrm{vp}}(\mathbf{r}) = -\frac{\epsilon_0 R^2}{2 \cdot (|\mathbf{r}|^2 + 2\xi^2)}, \tag{10}$$

where R is the radius of the associated defect and $\epsilon_0 = \Phi_0^2/(2\pi\mu_0\lambda^2)$ is an energy constant.

The critical current of a HTS films is determined by the collective behaviour of the vortices. The nature of the vortex lattice is governed by the magnetic field and temperature ranges under which various phases can be recognized. In particular, at high-temperature range the vortex lattice is in a liquid phase associated with substantial power dissipation due to non-localized nature of the associated vortices [41]. As the temperature is lowered, the vortex lattice becomes increasingly localized ultimately transitioning into Bose-glass or Mott-insulator phases [42].

2.3 $YBa_2Cu_3O_{6+x}$

The $YBa_2Cu_3O_{6+x}$ (YBCO) is a high-temperature superconductor that is part of the cuprate family, characterized by the presence of the CuO_2-planes along which the

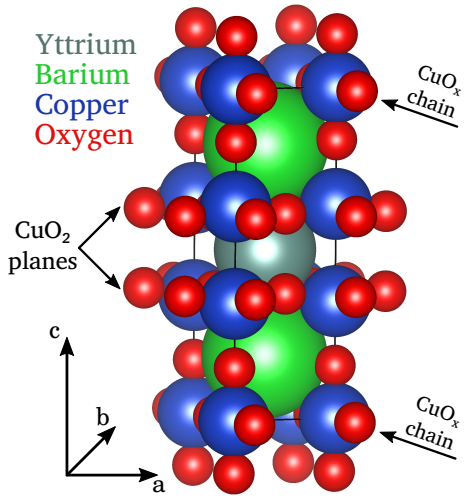

Figure 2. Illustration of the orthorhombic unit cell of YBCO. The figure is drawn with the help of VESTA [43].

supercurrent is carried. These planes within the unit cell of YBCO is illustrated in Figure 2. The structural and superconducting properties of YBCO are determined by the average amount of oxygen (x) within the unit cell. As the overall oxygen concentration is increased above $x \approx 0.4$, the added oxygen starts to be situated in the CuO_x chains, illustrated in Figure 2, inducing a structural phase transition from tetragonal to orthorhombic unit cell. Superconductivity is manifested only for the orthorhombic structure with lattice parameters $a \approx 3.82\,\text{Å}$, $b \approx 3.89\,\text{Å}$ and $c \approx 11.68\,\text{Å}$ [44; 45; 46]. Moreover, the critical temperature of YBCO is determined by the associated oxygen concentration with a maximum of $T_\text{c} \approx 92\,\text{K}$ obtained for $x \approx 0.9$ [45]. The highly anisotropic unit cell of the YBCO results in substantial variation of the characteristics length scales between different directions. In particular, for YBCO along the ab-plane $\lambda_{ab} \approx 150\,\text{nm}$ and $\xi_{ab} = 1.5\,\text{nm}$, while in the c-direction $\lambda_c \approx 450\,\text{nm}$ and $\xi_c = 0.3\,\text{nm}$ [2].

The applicability of YBCO, along with all the other known HTS materials, is limited by its brittle ceramic structure. In particular, this complicates the manufacture of practically implementable flexible YBCO cables required for various important power applications. This problem has been addressed by the development of coated conductors, where YBCO has been applied as a thin film grown on a buffered metallic substrates [7; 3]. Thus, this thesis focuses on studying the properties of YBCO in the form of thin films.

2.4 Vortex pinning

As concluded above, the vortices experience an attractive interaction towards any type of defects within the superconducting lattice in the vicinity of which the superconducting order parameter is decreased. The substantial presence of defects within a crystal lattice is typically associated with poor sample quality and the associated properties, such as low transition temperature and zero field J_c, but for type-II superconductors under high magnetic fields this typically improves the critical current density of the superconducting by reducing the vortex motion via pinning them.

The deposited YBCO thin films contain various natural unavoidable defects that act as pinning centers [7]. Most commonly, these include point-like vacancies and interstitials. There also exists more complex planar defects, such as YBCO (110)-plane oriented twin boundaries that delimit two regions of the YBCO lattice where the unit cell a- and b-axes are oriented differently. Another common types of planar defects are YBCO c-axis oriented stacking faults, where the layering of the unit cells has been perturbed. The pinning efficiency of the natural defects is rather poor at low-temperature range, but gradually improves as the temperature is increased [47]. Near the transition temperature the natural defects can effectively pin the vortices even under substantial magnetic fields. However, at high-temperature range the magnetic field cannot be increased to a sufficient magnitude required by the applications without driving the superconductor into normal state due to the T-B relation illustrated in the superconducting phase diagram in Figure 1(b). Consequently, the high-field performance of the HTS films can be only addressed at sufficiently low temperatures, where the effect of natural defect on vortex pinning is unfortunately diminished.

The vortex pinning can be enhanced, particularly at the low-temperature range, by adding non-superconducting dopant materials within the superconducting matrix typically referred to as artificial pinning centers (APC). The APCs can be generally divided into two sub-categories. Firstly, there are uncorrelated APCs, such as that form randomly distributed spherical pinning centers within the superconducting lattice. These defects are similar to the naturally occurring vacancies, but are remarkably larger in effective diameter and thus have increased pinning efficiency as suggested by Eq. (9). The commonly used uncorrelated APC materials used along with YBCO include Y_2O_3 [48] and $BaCeO_3$ [49].

Secondly, there are correlated APCs consisting of systematically organized groups of impurity particles or defects. Most notably, these include materials where the associated unit cells prefer to stack on top of each other during the deposition process ideally forming a lattice of parallelly oriented nanorods penetrating through the whole superconducting film. The formation of coherent nanorods requires both precisely optimized deposition conditions and suitable size of the APC unit cell relative to the surrounding lattice [15]. Materials that have had a great success when ap-

plied with YBCO include Ba_2YNbO_6 [50], Ba_2YTaO_3 [51], $BaSnO_3$ (BSO) [52], $BaHfO_3$ (BHO) [53] and $BaZrO_3$ (BZO) [8; 9], all of which form nanorods oriented along the c-axis of YBCO unit cell. The pinning performance of the nanorods highly depends on the orientation of the magnetic field which determines the orientation of the vortices. From Eq. (23) it is obvious that the greatest pinning performance is achieved when the direction of the applied field is parallel to the nanorods and vice versa. This can be directly observed as substantially increased J_c for magnetic fields oriented along the c-axis of YBCO, that is parallel to the surface vector of the film. Such modification of the intrinsic anisotropy of YBCO is typically referred to as the c-peak and is considered as the hallmark for nanorods [9]. Since various applications require good performance for the HTS films under magnetic fields oriented along this particular direction, the nanorod have become an essential component of the manufactured HTS films [54; 11; 6].

Due to their importance in the field, the mechanisms of nanorod formation within YBCO lattice has been widely studied. This enables the engineering of pinning structures suitable for specific needs. The diameter of the nanorod, which ultimately scales the pinning force, has been shown to be determined by the the lattice mismatch between the unit cells of the superconductor and the APC material [15; 55]. Thus, the diameter of the nanorods can be controlled by choosing the APC material with respect to the superconductor. The diameters of the formed nanorods within the lattice of YBCO range from smallest of $\sim 4\,\text{nm}$ (BHO) [53] to the largest $\sim 10\,\text{nm}$ (BSO) [52]. Since the pinning force is proportional to the square of the nanorod radius, the pinning properties between the nanorods formed from the aforementioned materials vary immensely. Another important controllable parameter is areal density of the nanorod lattice. This can be tuned independently from the nanorod radius by varying the initial dopant concentration in the deposition target [56; 15]. The areal density of the nanorod lattice ultimately determines the matching field, defined as the field where the number of vortices equals to the number of effective pinning centers, above which the vortex dynamics limited J_c gradually decreases.

Despite substantially improving the J_c of under the high-field range, the introduction of APCs within the superconducting lattice always degrades the J_c in the low-field range ($B < 0.1\,\text{T}$), as schematically illustrated in Figure 3 [30; 57; 7], **[III, VII]**. This is simply because the APCs reduce average cross-sectional area for the supercurrent to pass through. Moreover, the APCs induce strain fields within the superconducting lattice that disturb electron pairing and thus degrade the intrinsic properties of the superconductor. In particular, this is manifested as the lowering of the superconducting transition temperature for more prominent doping [58; 59; 57; 56; 30; 60]. Lately, the effect of nanorod induced strain has been succesfully addressed by doping films with two different dopants that have opposite lattice mismatches with respect to the superconducting matrix [61; 62; 63; 64]. As a drawback, such double-doping further decreases the superconducting cross-sectional with

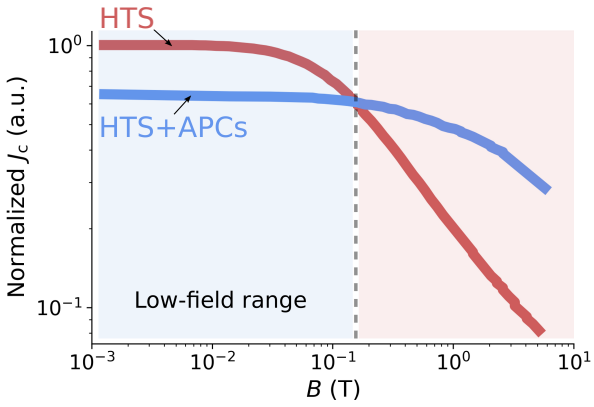

Figure 3. A schematic illustration of the typically measured critical current densities at low-temperature range as a function of applied magnetic field for pure superconducting films and doped films introduced with APCs.

the cost of pinning performance.

In summary, Figure 3 illustrates how prominent doping is a necessity for applications working under high-field range ($B > 2$ T), and vice versa the doping should be completely avoided for low-field applications. Thus, the optimal pinning structure evidently depends on the field range associated with the specific application and obtaining the best performance requires meticulous tailoring.

2.5 Zero field properties

The zero field J_c, that is ideally the J_c in the absence of vortices, is determined by the electron mean free path that is directly linked with the overall crystalline quality of the superconducting lattice [65; 66]. Despite the name, the concept of zero field J_c also applies under magnetic field. In particular, the zero field J_c limits the overall J_c of the superconductor in the low-field range and remains constant as the applied magnetic field is increased [65; 66].

The only possibility to increase the zero field J_c is to improve the overall crystalline quality of the superconducting film. This is affected by several factors, such as choice of substrate and various parameters associated with the deposition process. A particular problem related to the bad crystalline of the HTS films occurs when growing thick films (thickness>1 μm) utilized in the coated conductor industry. The crystalline quality of the deposited film is found to decrease drastically when the thickness of the film is increased. This results in exponential decay of the zero field J_c as a function of films thickness [67]. Thus the thickness of the film turns out to be the limiting factor.

Surprisingly, the vast decay of the crystalline quality as a function of film thick-

ness can be reduced via the addition of nanorods within the superconducting lattice [68; 69; 70; 71]. However, the drawback of this method is that the addition of the nanorods reduces the J_c in the low-field range and thus zero field J_c remains far from optimal despite the improvement for thick films. A more convenient approach is to apply HTS-insulator ML structures, where a thin layer of some insulating material, such as CeO_2 or $SrTiO_3$, is deposited between adjacent superconducting layers. These kinds of ML structures have been widely studied and provided substantial improvement in the superconducting properties of the associated films [72; 73; 74; 75; 76; 77; 78; 79; 80; 81; 82; 83; 84]. The observed improvement of zero field superconducting properties have been associated with decreased surface roughness after the deposition of the insulating layer. This provides better growth conditions for the upcoming deposition of the superconducting layer resulting in improved overall crystalline quality [73; 77]. The insulating layer has also been associated with the presence of coherent small diameter precipitates that are acting as effective pinning centers, thus also improving the J_c under substantial magnetic fields [77; 81]. Recently, the superconducting properties of BZO doped YBCO films have been substantially increased by deposition of thin spacer layers of Ca-doped YBCO within the film. The strain driven diffusion of Ca out of the spacer layers results in reduced lattice mismatch between BZO and YBCO manifesting as more coherent interface between the two phases [85; 86].

2.6 Superconducting multilayer films

As concluded in the previous sections, the best performance for the HTS films under high- and low-field ranges can be evidently achieved with prominent and inconspicuous doping, respectively. However, in the mid-field range ($0.1\,\mathrm{T}<B<2\,\mathrm{T}$) one could potentially increase the J_c by applying specifically tailored ML structures consisting of two or more superconducting layers with alternating APC sizes and concentrations thus compromising between the good pinning performance and zero field properties. There has been several experimental realizations of such ML structures, where substantial improvement of the current carrying properties of the associated ML films have been reported [76; 87; 88; 30; 32; 33; 34]. However, in none of these works is the studied ML structure comprehensively justified. As the systematic approach to find the optimal ML structure is still lacking, there still could be significant improvement to be achieved for the current carrying properties of the HTS films. We see the investigation of the these ML structures as the most potential way to further enhance the properties and applicability of the HTS films.

3 Methods

3.1 Pulsed laser deposition

The pulsed laser deposition (PLD) is the most effective technique to grow epitaxial thin films from complex oxide materials, such as YBCO [89]. The general operation principle of PLD is quite simple. A bulk target of the material to be grown is shot with high energy laser pulses. The energy of the laser pulse is absorbed within the target causing it to evaporate near the surface. This repeated surface evaporation creates a plasma plume that is directed to a heated substrate on the surface of which the ablated atoms and ions recombine forming the epitaxial film under optimized conditions [90].

The YBCO thin films studied in this thesis were grown on $SrTiO_3$ substrate that was heated up to 750 °C temperature before the ablation. The YBCO targets were shot by $\sim$1.3 J/cm^2 laser pulses with 5 Hz frequency generated by 308 nm wavelength XeCl excimer laser. The ablation was performed under 0.175 Torr oxygen circulation. The typically used 2000 laser pulses result in roughly 200 nm thick epitaxial YBCO films. After the ablation, an oxygen treatment was performed by lowering the substrate/film temperature down to 725 °C and filling the deposition chamber with 750 Torr oxygen. The oxygen is then diffused within the lattice of the deposited YBCO film causing a transition from tetragonal to the superconducting orthorhombic phase. After 10 minutes of the oxygen treatment, the substrate/film temperature was lowered down to room temperature at 25 °C/min rate and the deposited film was removed from the chamber.

3.2 X-ray diffraction

The structural properties of the deposited films were studied with x-ray diffraction (XRD) method. The principle of the XRD method is based on illuminating the epitaxial sample with x-rays in different incident angles (θ) and measuring the intensities of the reflected x-rays [91]. Depending on the θ and the distance of the between adjacent lattice planes (d), the x-rays reflected from the bottom and top planes interfere with each other creating a diffraction maximum when the d equals to an integer multiple (n) of the used wavelength (λ). This is expressed with Bragg's law [92]

$$2d\sin(\theta) = n\lambda. \tag{11}$$

By measuring the diffraction maxima as a function of θ, one is able to calculate the average distances between the desired lattice plains using Eq. (11). This measurement is referred to as the θ-2θ scan and, in this work, was used to calculate the length of the YBCO c-lattice parameter. Moreover, by measuring the widths of the diffraction peaks one is able to compare the quality of the crystalline structure between the samples. In particular, the widths of the (005)-peak can be used to compare the strains between different films. The coherence of the the c-lattice parameter can be probed by measuring the s.c. rocking curve, that is by fixing 2θ to the intensity maximum of the (005)-peak and rocking the sample along the direction of the beam.

The XRD measurements were done using the Empyrean x-ray diffractometer manufactured by Panalytical. All of the measurements used the 1.54 Å wavelength x-rays resulting from Cu K_α excitation. The non-parallel components of the x-rays were filtered using either 0.02 or 0.04 rad soller slits among others.

3.3 Transmission electron microscopy

The transmission electron microscopy (TEM) enables the probing of the structural properties of the sample in atomistic scale [93]. In this work, the desired accuracy is however in the nanometer-scale, as the TEM was mainly used to study the assembly of the various nanorods within the YBCO lattice of the thin film. Despite being a highly informative method to characterize the structural properties of the films, obtaining the TEM images is a rather laborious task. This is because the films to be measured have to be carefully prepared for the measurement by creating a thin cross-sectional lamella of the film *in-situ* lift-off procedure. After the sample preparation, the actual measurement takes place. In TEM measurement, the prepared sample is irradiated with an electron beam typically generated by tungsten filament and precisely focused using various electromagnetic lenses. The transmission probability of the electrons depends on the atomic structure in the vicinity of the focused beam. By collecting and measuring the number of the transmitted electrons as a function of position, one is ultimately able to create a detailed image of the film microstructure. This mode of operation is typically referred to as scanning-TEM (STEM).

3.4 Magnetic measurements

The studied superconducting thin films were measured using the AC measurement system (ACMS) of the Physical Property Measurement System (PPMS) manufactured by Quantum Design. The superconducting transition temperatures were measured using the AC-mode of the device, in which the sample is held stable inside a two-coil system. AC current is applied though the outer coil creating an alternating magnetic field (H) that perturbs the sample. The resulting magnetization of the sample (M) is further recorded by the inner pick-up coil, the obtained signal of which is

proportional to the derivative dM/dH. The measurements were performed using a 113 Hz excitation field with 0.1 mT amplitude.

The magnetic hysteresis loops, from which the $J_c(B)$ can be further calculated, were measured using the DC-mode of the PPMS. The DC-measurements are performed by vibrating the sample inside pick-up coils while applying external magnetic fields. The vibrating sample induces a voltage in the pick-up, the amplitude of which is directly proportional to the magnetization of the sample according to the Faraday's induction law.

3.5 Transport measurements

In order to perform the standard four-probe transport measurements for the superconducting thin films, the samples were first patterned accordingly using photolithography. In particular, photoresist was first spin-coated on the surface of the film. Once dry, a mask resembling to the pattern to be etched was placed on top of the sample which was then exposed to UV light. After this, the pattern was developed by first rinsing the sample in NaOH solution and then etching the pattern using H_3PO_4 solution. Finally, the samples were cleaned using aceton and isopropyl alcohol. In this work, the width of the patterned stripes was fixed to 50 μm.

Once patterned, the sample was connected to the sample holder with Al wire using the TPT wire bonder. The angular dependence of the critical current was measured using the PPMS horizontal rotator option. The value of the critical current was determined by probing the sample with various different currents and measuring the associated voltage losses across the film (IV-curve). The critical current was then determined as the current for which the voltage exceeds a specific threshold value.

3.6 Simulations

3.6.1 Molecular dynamics

Molecular dynamics (MD) simulation is a method that is used to calculate the dynamics of a particle ensemble based on their interactions according to Newtonian mechanics. The MD method is based on the leapfrog algorithm according to which the dynamic evolution of the system, in terms of particles positions (**r**), velocities (**v**) and accelerations (**a**), can be solved by iterating the following set of rules using a sufficiently small timestep (Δt) [94]:

i) Update velocites by half time step:

$$\mathbf{v}(t + \Delta t/2) = \mathbf{v}(t) + \frac{\Delta t}{2} \cdot \left(\mathbf{a}(t) - \frac{\eta}{m} \mathbf{v}(t + \Delta t) \right) . \tag{12}$$

ii) Update the positions by full time step:

$$\mathbf{r}(t + \Delta t) = \mathbf{r}(t) + \Delta t \cdot \mathbf{v}(t + \Delta t/2)\,. \tag{13}$$

iii) Update forces and the corresponding accelerations according to previously updated positions.

iv) Update the velocities again by half time step according to $\mathbf{v}(t + \Delta t) = \mathbf{v}(t + \Delta t/2) + \Delta t/2 \cdot (\mathbf{a}(t) - \eta \mathbf{v}(t + \Delta t/2)/m)$. Solving for $\mathbf{v}(t + \Delta t)$ gives

$$\mathbf{v}(t + \Delta t) = \left(\frac{1}{1 + \frac{\eta \Delta t}{2m}} \right) \cdot \left(\mathbf{v}(t + \Delta t/2) + \frac{\Delta t}{2} \mathbf{a}(t + \Delta t) \right) . \tag{14}$$

The 3D vortex dynamics simulation

The presented simulation model is based on the above described MD method, where the vortex lines are discretized into chains of individual particles fixed together by an artificial spring force as illustrated in Figure 4. The vortex particles are subject to various forces presented in Figure 4, including the repulsive interaction force between two vortex lines (F_{vv}), the pinning force between vortex and pinning site particle (F_{vp}), the line-tension that strives to orient the vortex along the YBCO c-axis (F_{ten}), the magnetic force striving to orient the vortex parallel to the applied magnetic field (F_{mag}) and the Lorentz force resulting from the applied critical current that drives the vortices into motion (F_{Lor}). The various APCs are modelled by arranging the immobile pinning site particles into corresponding configurations, an example of which in the case of nanorods is presented in Figure 4.

Due to the classical nature of the leap-frog algorithm, one has to assign the vortex particles with fixed masses (m). The concept of mass is not well defined in the context of the vortices. However, for the purpose of our simulation the mass of the vortex particles can be chosen arbitrarily along with the drag coefficient (η) given that the terminal velocity of the vortices is reached in a smaller distance when compared with average distance between the nanorods [29].

The simulation grid was designed to model YBCO thin films by defining the associated xy-plane parallel to the ab-plane of the YBCO unit cell, along which periodic boundary conditions were applied. The grid size along the z-direction along with the number of particles corresponding to a single vortex line (n) are somewhat arbitrary quantities that can be chosen depending on the situation. The total number of vortex lines (N_{v}), on the other hand, was determined based on the grid area along

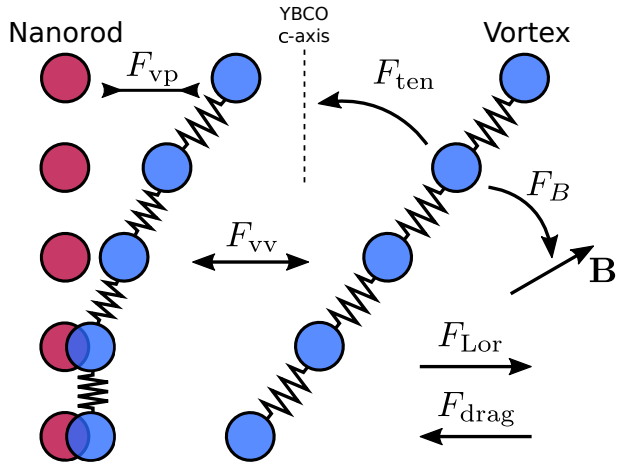

Figure 4. A schematic illustration of the MD method based simulation model. The vortices are subjects to repulsive vortex-vortex force ($F_{\rm vv}$), attractive pinning force ($F_{\rm vp}$), line-tension force striving to orient the vortices parallel to the YBCO c-axis ($F_{\rm ten}$), magnetic force (F_B) striving to orient the vortices parallel to the applied magnetic field (**B**) and Lorentz force resulting from the applied current that drives the vortices in motion along with the dissipative drag force ($F_{\rm drag}$). Figure from **[IV,V]**.

the xy-plane (A) and the desired applied magnetic field according to formula $N = BA/\Phi_0$.

The repulsive vortex-vortex interactions are taken into account by applying the previously derived formula, Eq. (7), for the potential between two c-axis oriented vortices separated by a distance $r = |\mathbf{r}_{xy}|$. Differentiating Eq. (7) with respect to $|\mathbf{r}_{xy}|$ gives the corresponding total force as

$$F_{\rm vv} = \frac{L\epsilon_0}{\lambda} \cdot \mathrm{K}_1\left(\frac{|\mathbf{r}_{xy}|}{\lambda}\right) \approx L\epsilon_0 \frac{1}{|\mathbf{r}_{xy}|}\,. \tag{15}$$

The Eq. (15) cannot, however, be directly used in the simulation because the discretization of the vortex line would lead to larger total force when iterated over every pairs of particles. In order to calculate the interaction correctly, the following ansatz has been proposed

$$F^*_{\rm vv} = W \int_0^L \int_0^L \frac{\cos\phi_{ij}}{d_{ij}} dz^2, \tag{16}$$

corresponding to the continuous vortex limit ($n \to \infty$) where the separations between the adjacent vortex particles approaches to zero. The parameters d_{ij} and ϕ_{ij} are illustrated in Figure 5(a), while W is the scaling constant (units J/m^2) to be determined so that Eqs. (15) and (16) output the same total force for the geometry

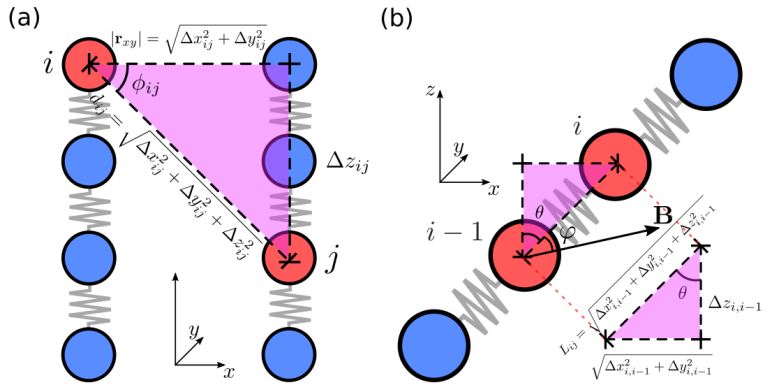

Figure 5. (a) The geometry of the two-vortex system used to deduce formula for the vortex-vortex interaction. (b) The geometry of the vortex when calculating the line tension and the magnetic forces. Figure from **[IV,V]**.

illustrated in Figure 5(a). For practical reasons, the expression of every equation implemented in the simulation in terms of cartesian coordinates is desired. In the case of Eq. (16), one can easily deduce from Figure 5(a) that $\cos\phi_{ij} = \sqrt{\Delta x_{ij}^2 + \Delta y_{ij}^2}/d_{ij}$ and $d_{ij} = \sqrt{\Delta x_{ij}^2 + \Delta y_{ij}^2 + \Delta z_{ij}^2}$. It should be noted, that the $\Delta x_{ij} \equiv x$ and $\Delta y_{ij} \equiv y$ are constants under the chosen geometry, with $\Delta z_{ij} \equiv z$ being the only varying parameter. The Eq. (16) can be written with the previously defined expressions as

$$\begin{aligned} F_{\mathrm{vv}}^{*} &\approx W \int_0^L \int_0^L \frac{\sqrt{x^2+y^2}}{x^2+y^2+z^2} dz^2 \\ &= WL \tan^{-1}\left(\frac{L}{|\mathbf{r}_{xy}|}\right). \end{aligned} \tag{17}$$

The obtained expression can be further simplified by using the approximation $\tan^{-1}(L/|\mathbf{r}_{xy}|) \approx L/|\mathbf{r}_{xy}|$. Equating this with Eq. (15) yields $W = \epsilon_0/L$. Consequently, one is motivated to define the force per unit length between two discrete vortex particles i and j in separate vortex lines as the integrand of Eq. (17) scaled by the above solved W. That is,

$$f_{\mathrm{vv},ij} = \frac{\epsilon_0 \sqrt{\Delta x_{ij}^2 + \Delta y_{ij}^2}}{n(\Delta x_{ij}^2 + \Delta y_{ij}^2 + \Delta z_{ij}^2)}, \tag{18}$$

where continuous length of a vortex L has been replaced with its discrete counterpart n. The direction of $f_{\mathrm{vv},ij}$ is evidently parallel to the line connecting the associated vortex particles.

The attractive interaction between a vortex particle i and a pinning site j is taken into account via the pinning potential presented in Eq. (10). Differentiating this with respect to $|\mathbf{r}_{ij}| = \sqrt{\Delta x_{ij}^2 + \Delta y_{ij}^2 + \Delta z_{ij}^2}$ gives the pinning force per unit length

$$f_{\mathrm{vp},ij} = \frac{\epsilon_0}{n} \frac{|\mathbf{r}_{ij}| R^2}{\left(|\mathbf{r}_{ij}|^2 + 2 \cdot \Lambda(\theta)^2 \xi^2\right)^2}, \tag{19}$$

where the intrinsic anisotropy of the material has been taken into account by scaling ξ with the Blatter scaling equation [21]

$$\Lambda(\theta) = \sqrt{\frac{\sin^2\theta}{\gamma^2} + \cos^2\theta}, \tag{20}$$

where θ is the angle between the direction of the applied magnetic field and the YBCO c-axis. Notice, that Eq. (19) has also been scaled by the number of vortex particles similarly to what was done for the vortex-vortex interactions. As with the previously calculated vortex-vortex interaction, the direction of the $f_{\mathrm{vp},ij}$ is along the line connecting the two associated particles.

The magnetic line-tension strives to minimize the volume of magnetic fields within the superconductor by orienting the vortex lines along the YBCO c-axis. The associated potential is given by [21; 29]

$$E_{\mathrm{ten}} = \epsilon_0 L \cdot \ln\left(\frac{\lambda}{\Lambda(\theta)\xi}\right), \tag{21}$$

where ξ is again scaled with the Blatter scaling function given by Eq. (20). In the case of our discretized vortex model, the particle i is affected by the potentials created by the adjacent particles $i-1$ and $i+1$. Figure 5(b) illustrates how the parameters of Eq. (21) can be expressed in terms of cartesian coordinates as $L_{i,i+j} = \sqrt{\Delta x_{i,i+j}^2 + \Delta y_{i,i+j}^2 + \Delta z_{i,i+j}^2}$, $\cos\theta = \Delta z_{i,i\pm1}/L_{i,i+j}$ and $\sin\theta = \sqrt{\Delta x_{i,i+j}^2 + \Delta y_{i,i+j}^2}/L_{i,i+j}$, where $j = \pm 1$. The associated force can be further calculated as

$$\mathbf{F}_{\mathrm{ten},i} = -\sum_{j=-1,1} \left(\partial_{\Delta z_{i,i+j}} E_{\mathrm{ten}}, \partial_{\Delta y_{i,i+j}} E_{\mathrm{ten}}, \partial_{\Delta z_{i,i+j}} E_{\mathrm{ten}}\right). \tag{22}$$

The steady-state tilt of the vortex is determined by the ratio between the previously mentioned line-tension and the magnetic force that strives to orient the vortex line parallel to applied magnetic field ($\mathbf{B}$). The energy of a vortex line differing for an angle φ from $\mathbf{B}$ is given by [29]

$$E_{\mathrm{B}} = \frac{\Phi_0 B}{\mu_0} \cos\varphi\,. \tag{23}$$

For the discretized vortex lines, the potential experienced by particle i is calculated by considering the angle between the line that connects the adjacent vortex particles $\mathbf{r} = (\Delta x_{i,i-1}, \Delta y_{i,i-1}, \Delta z_{i,i-1})$ and $\mathbf{B} = (B_x, B_y, B_z)$. The cosine of this angle can easily be expressed by the dot-product formula $\cos\varphi = \mathbf{B} \cdot \mathbf{r}/(|\mathbf{B}| \cdot |\mathbf{r}|)$. The associated force can further be calculated as

$$\mathbf{F}_{\mathrm{B},i} = -\left(\partial_{\Delta x_{i,i-1}} E_{\mathrm{B},i}, \partial_{\Delta y_{i,i-1}} E_{\mathrm{B},i}, \partial_{\Delta z_{i,i-1}} E_{\mathrm{B},i}\right). \tag{24}$$

The vortex lines are made mobile by the Lorentz force, given by Eq. (8), resulting from the applied current through the superconductor. Since the output vortex pinning limited J_c of the simulation is expressed in arbitrary units, one can simply write

$$F_\mathrm{Lor} \sim J, \tag{25}$$

where the direction of F_Lor is chosen according to desired direction of current. The J_c is determined to be the J for which the vortices fulfil a given stability condition after the system has been evolved by a total time $t = n\Delta t$, where n is the number of iterations of the leap-frog algorithm.

The continuity of the vortex lines was applied by restricting the movement of the outermost particles of the vortex lines into xy-plane oriented layers. An artificial spring force has been further applied between the vortex particles preventing the mixing of the order of particles within the single vortex line. The total force experienced by particle i was calculated as

$$F_{k,i} = k \cdot |\mathbf{r}_i - (\mathbf{r}_{i-1} + \mathbf{r}_{i+1})/2|, \tag{26}$$

which was further projected onto the line $\mathbf{r}_{i-1} - \mathbf{r}_{i+1}$. The force constant was adjusted so that the spring force manages to keep the vortex particles in order without significantly affecting the other aspects of the simulation.

Perhaps the biggest uncertainty related to the physical accuracy of the proposed simulation is the relative magnitudes of the different forces. The numerical value of ϵ_0, in particular, has to be addressed based on theoretical calculation with the complete lack of empirical basis. Regardless, the vortex-vortex and the pinning forces are always scaled similarly, which is arguably the most important aspect regarding the physical accuracy of the simulation. Consequently, the simulation is expected to produce the most reliable results when the vortex line-tension and the magnetic forces can be neglected, that is when the vortices are aligned along the z-direction corresponding to $\theta = 0$.

In the end, there are no incorrect models for physical phenomena, but the quality of the model can be disputed. The presented model has been able reproduce the key experimentally observed features for the evolution of J_c as a function of both B and θ **[IV, V]**. Consequently, it can be considered to capture the essential aspects of vortex dynamics in HTS thin films.

3.6.2 Metropolis-Hastings simulations

The Metroplois-Hastings algorithm belongs to the wide class of Markov Chain Monte Carlo methods [95; 96]. Unlike the MD method, the Metropolis-Hastings algorithm based simulations rely on random sampling of probability distributions. Consequently, using them to simulate the evolution of certain physical systems can result in substantially reduced computational cost when compared with alternative simulation methods. This holds true particularly for systems consisting of large numbers of vortices and columnar defects oriented parallel to each other, where the energy of a single vortex can be effectively calculated. The Metropolis-Hastings algorithm addresses the evolution of such system by iterating the following set of rules: i) Determine the total energy of the system in *initial state* (E_0). ii) Create an *excited state* by changing the position of randomly chosen vortex by Δr in random direction. iii) Calculate the total energy of the system after the displacement in the excited state (E_1) iv) If $E_1 < E_0$, accept the excited state to be the new initial state for next iteration. Else, accept the excited state with probability $p = \exp(-(E_1 - E_0)/kT)$. Otherwise, the system remains in the initial state.

3.6.3 Artificial intelligence models

The use of various artificial intelligence (AI) models has become increasingly more prominent over the recent years even from a layman's perspective. AI will arguably continue to have revolutionary implications in the field of engineering and technology, but it also has a huge potential to be used for fundamental research. This is particularly enabled by the widely accessible open source libraries which enable the easy use of the highly developed state-of-the-art AI models even for people who are not familiar with the underlying complex algorithms.

The basic principle underlying all of the *supervised* AI models is quite simple. The AI model is first *trained* with a given dataset. This *training set* is formed by data points consisting *descriptors* and *features* that the AI is supposed to learn how to associate with each other. If the training is sufficient, the AI model should be able to reliably predict the feature corresponding to an unseen descriptor outside the training set. That is, the AI *learns* to associate the descriptors with the features in a generalized manner. The evident requirement for the use of AI is to have a sufficiently large dataset for adequate training of the model.

To date, there are several different available supervised AI models associated with a wide range of complexity. The complexity of an AI model is reflected in the number of the associated *hyperparameters* (HP), which are the model's internal parameters that have a great effect on its learning capability [97; 98]. Consequently, the HPs should be rigorously optimized for the specific learning task in order to achieve good results. While the HPs of simple models can be efficiently optimized

with brute-force trial and error based *grid search*, the optimization of more complex models have to be addressed with more advanced techniques, such as *random search* or *Bayesian optimization*.

In this thesis three different AI models are considered. These include, in increasing levels of complexity, *kernel ridge regression* (KRR), *gradient-boosted decision trees* (GBDT) and *neural networks* (NN). A detailed description of the used AI models is presented in the supplemental information of **[VI]**.

4 Results and discussion

4.1 Columnar defects within YBCO matrix

4.1.1 Pinning mechanisms

As already discussed in section 2.4, the pinning of the vortices within columnar defects, such as nanorods, significantly modulates the intrinsic anisotropy of the J_{c}. The modulated anisotropy can be addressed by measuring the angular dependence of the critical current density ($J_{\mathrm{c}}(\theta)$), that is by determining J_{c} under a magnetic field tilted at an angle θ with respect to the c-axis of YBCO. Moreover, the shapes of the $J_{\mathrm{c}}(\theta)$ curves, in particular, can be addressed via simulations [29] providing microscopical information about the pinning mechanisms taking place in the associated pinning structure. Comparison between experimentally measured and simulated $J_{\mathrm{c}}(\theta)$ curves allows one to make conclusions about the underlying pinning structure without access to TEM images.

In [**I**] the $J_{\mathrm{c}}(\theta)$ for various nanorod lattices with different areal densities (σ), diameters and applied fields has been simulated using the model originally introduced in [29]. Such systematic study has enabled the identification of various pinning mechanisms associated with specific ranges of σ and θ. More importantly, the obtained microscopical information inspires one to consider the vortex dynamics limited $J_{\mathrm{c,v}}$ to be ultimately probabilistic in nature. In particular, one can propose that

$$J_{\mathrm{c,v}} \sim P_{\mathrm{cross}} \cdot P_{\mathrm{pin}} \tag{27}$$

where P_{cross} is the probability that a vortex crosses a pinning site and P_{pin} is the probability that a vortex gets pinned after it has encountered a columnar defect.

The proposed probabilistic pinning model is in line with the available experimental evidence. Firstly, the relation between the $J_{\mathrm{c,v}}$ and P_{cross} implies that the $J_{\mathrm{c,v}}$ increases as the pinning potentials of the nanorods are deepened via increasing their radii [21; 99]. This conclusion is fairly obvious for which there exists extensive experimental evidence. The best reference for is [**VII**], where the effect of nanorod radius and associated dopant concentrations on J_{c} have been systematically studied. In particular, the $J_{\mathrm{c}}(\theta = 0)$ of 6% BZO doped YBCO film at 10 K under 1 T field was concluded to be significantly greater when compared to BHO doped film with corresponding dopant concentration. Since the dopant concentrations for these samples

were the same, one may assume that the effect of zero field current for the samples is similar regardless of the different dopant materials, at least when in comes to the reduced superconducting cross-sectional area. Moreover, both of these systems can be considered to have similar P_{cross}, as the density of the vortices ($n = B/\Phi_0$) is significantly smaller than the associated areal densities of the nanorods due to the relatively high 6% dopant concentrations. Thus, the only attributable origin for the increased J_{c} is from the enhanced P_{pin} via increased nanorod radius.

In order to validate the relation between $J_{\mathrm{c,v}}$ and P_{pin}, contrary to the previous case, one must consider lattices of nanorods with fixed radius but altering areal densities. A correspoding study has been presented in [100], where the areal density of BZO nanorod had been optimized within the high-temperature limit associated with thermal activated flux flow. The experimentally determined effective pinning potentials were observed to increase as a function of BZO concentration. Assuming that the radius of the BZO nanorods remains constant as a function of dopant concentration, the only plausible reason for the increasing effective pinning potential originates from dynamical behaviour of the vortices associated with P_{cross}.

The proposed pinning model evidently lacks quantitativity. However, as a benefit it can be conveniently used to associate the complex pinning mechanisms in wide magnetic field magnitude and angular ranges to the experimentally determined critical current anisotropies for various pinning structures. As an example, for $\theta = 0$, that is when the vortices are oriented parallel to the nanorods, the P_{pin} is proportional to the pinning force (or potential) determined by the radii of the associated nanorods [21; 99]. The P_{cross}, on the other hand, is determined by the number of available pinning centers. Under typical circumstances for $\theta = 0$, a single nanorod can occupy only a single vortex at a time. Thus, P_{cross} decreases as a function of applied magnetic field when the areal density of the vortex lattice ($n = B/\Phi_0$) increases with respect to σ gradually reducing the number of available pinning sites. The limit $n = \sigma$ defines the *matching field* (B_ϕ), under which all of the nanorods are occupied by a vortex as illustrated in Figure 6(a). Above B_ϕ, the P_{cross} becomes zero by definition and ideally $J_{\mathrm{c}} = 0$. However, in reality the vortices can stabilize outside the nanorods via vortex-vortex interactions or by pinning weakly into the natural defects within YBCO lattice as illustrated in Figure 6(b). Nevertheless, above B_ϕ both the P_{cross} and P_{pin} become small and the J_{c} can be experimentally observed to decrease rapidly as the field is increased [101]. It should be pointed out that for $\theta \gg 0$ the concept of B_ϕ is ill-defined due to the peculiar pinning mechanisms associated with this angular range that will be described below.

In particular, for $\theta \gg 0$ the vortices can experience either partial or multicolumn pinning [102; 103]. In the case of partial pinning, the magnetic force overcomes the line tension and the pinning force resulting in partially pinned vortices illustrated in Figure 6(c) [104; 105]. Partial pinning typically occurs for nanorod lattices with low σ at intermediate θ ($\approx$20–60°). The partially pinned vortices are evidently weakly

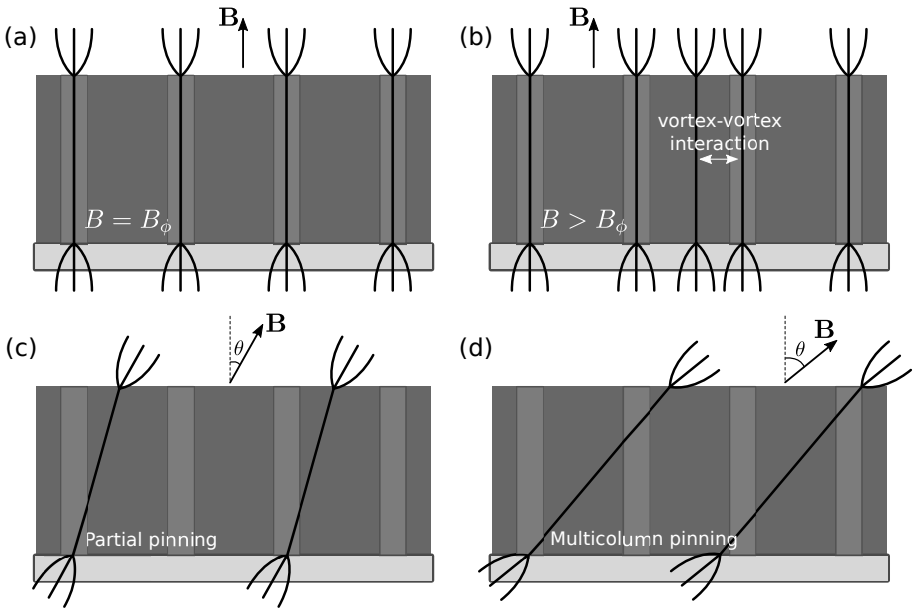

Figure 6. Schematic illustrations of various pinning mechanisms, including (a) typical pinning for $\theta = 0$ at the limit of matching field, (b) pinning above matching field via to vortex-vortex interactions and natural defects within YBCO lattice, (c) partial pinning where only a fraction of the vortex core is inside the nanorods and (d) multicolumn pinning where a single vortex is simultaneously pinned into several nanorods.

trapped and can be associated with significantly decreased P_{pin}. On the other hand, the angles at which partial pinning occurs is associated with increased P_{cross} due to larger interaction area of the vortex along the ab-plane. The multicolumn pinning refers to a single vortex getting pinned simultaneously into two or more nanorods as illustrated in Figure 6(d) [103]. Multicolumn pinning is favored, in particular, for nanorod lattices with high σ at high θ. The presence of multicolumn pinning increases both P_{pin} and P_{cross} and can thus result in the absence of the c-peak in particular for dense nanorod lattices.

With the above presented background one is easily able to understand the effects of nanorods on the shape of $J_{\mathrm{c}}(\theta)$. In particular, it is typically quite easy to estimate which of the probabilities, P_{cross} or P_{pin}, dominate under specific conditions and use this as the basis for explaining the shape of $J_{\mathrm{c}}(\theta)$.

4.1.2 Effect of nanorod diameter

Here, the effect of nanorods on the $J_{\mathrm{c}}(\theta)$ curve will be discussed. As already stated in section 2.4, the typical hallmark of the nanorods is considered to be the c-peak, that is the modulation of the $J_{\mathrm{c}}(\theta)$ along the c-axis of YBCO ($\theta = 0$). The main panel

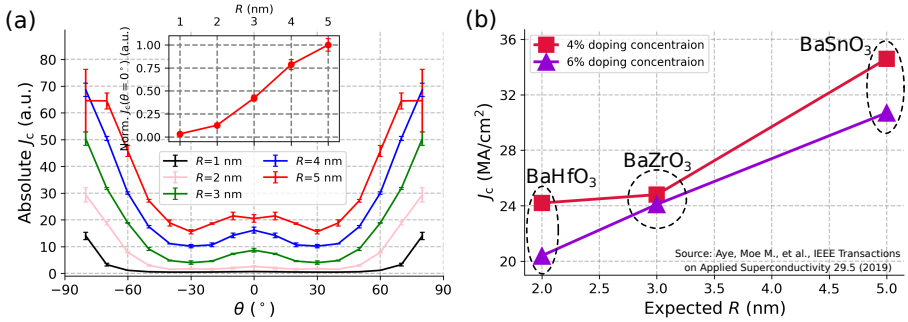

Figure 7. (a) Main: The simulated critical current angular dependencies for nanorod lattices with of constant areal densities but varying radii (R =1–5 nm) in the low-temperatture range under 1 T applied magnetic field. Inset: The normalized simulated $J_c(\theta = 0)$ as a function of the nanorod radius. (b) The magnetically measured $J_c(\theta = 0)$ under 1 T field for different nanorod densities as a function of the expected radius of the used nanorods. The data is extracted from [**VII**]. Both figures are from **[V]**.

of Figure 7(a) presents the simulated $J_c(\theta)$ curves, using the model presented in section 3.6.1, for lattices of nanorods differing by the value of associated radii within the range $R = 1$–$5\,\mathrm{nm}$. The simulations were performed in the low-temperature limit with $\lambda = 150\,\mathrm{nm}$ and $\xi = 1.5\,\mathrm{nm}$ using a $150{\times}150{\times}20\,\mathrm{nm}^3$ sized grid with constant number of 50 nanorods under $B = 1\,\mathrm{T}$ field so that $B < B_\phi$. Both the individual nanorods and the vortices consisted of 5 adjacent equidistant particles. As expected, the c-peaks can be observed for all of the performed simulations despite being barely visible for nanorod lattices with $R < 2\,\mathrm{nm}$ due to scaling of the figure. More interestingly, the absolute values of J_c increases as a function of R in the full angular range. In order to address this feature more comprehensively, the evolution of $J_c(\theta = 0)$ as a function of R has been illustrated in the inset of Figure 7(a). The shape of the simulated $J_c(\theta = 0, R)$ curve has slight exponential features for low R but seems to increase somewhat linearly for higher R. As discussed in the previous section, $J_c \propto P_{\mathrm{pin}}$, where the P_{pin} is proportional to the Boltzmann factor associated with the pinning potential. In conclusion, one can write

$$J_c \propto \mathrm{e}^{E_{\mathrm{vp}}/kT}, \tag{28}$$

where k is the Boltzmann constant, T is temperature and $E_{\mathrm{vp}} \sim R^2$ is the effective pinning potential expressed by Eq. (10). The exponential function can be approximated by a linear function at any point. The first-order term in the associated Taylor expansion is thus simply R^2 resulting in the relation

$$J_c \propto R^2, \tag{29}$$

which applies regardless of the temperature. This proportionality seems to apply particularly for small R, while for large values additional effects related to P_{cross}

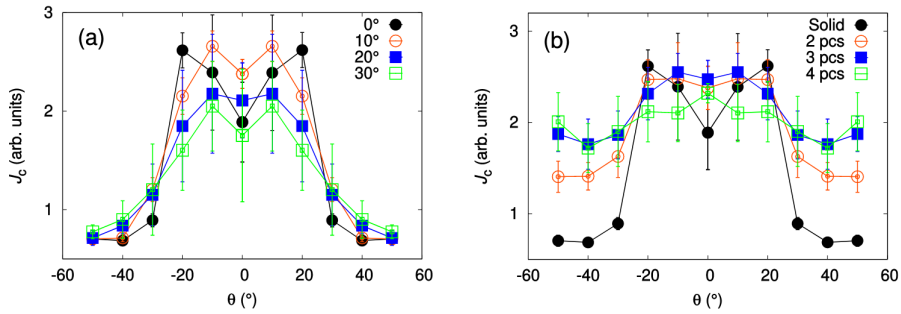

Figure 8. (a) The simulated c-peaks for differently tilted nanorods. (b) The simulated c-peaks for differently fragmented nanorods. Both figures are from **[VIII]**.

start to take place making the simulated $J_c(\theta = 0, R)$ curve more linear, perhaps even sublinear.

Figure 7(b) illustrates the experimentally observed $J_c(\theta = 0)$ for nanorod lattices consisting of different materials originally presented in [**VII**]. Based on previous works, the associated nanorods are expected to have different radii expressed by the horizontal axis in Figure 7(b). Given the uncertainties associated with the experimental measurements with respect to the idealized simulation model and assumptions regarding proposed Eq. (28), the experimental results coincide with the theoretical treatment.

4.1.3 Effect of disoriented nanorods

It is a very idealized assumption that the nanorod would grow perfectly oriented along the YBCO c-axis. For unoptimized deposition conditions the formed nanorods are typically fragmented and their orientation might deviate significantly from the c-axis [9; 106]. Thus, recognizing the effects of nanorod splay and fragmentation on $J_c(\theta)$ is essential for analyzing the vortex pinning using experimental data. In [**VIII**], the effect of these parameters on the shape of the c-peak has been systematically studied using the simulation model introduced in [29]. All of the simulations were performed in a 200×200 nm^2 grid with a total of 32 nanorods. The magnetic field was set to 0.75 T corresponding to a total of 14 individual vortices.

The effect of nanorod splay was studied by modeling the nanorods using a total of 20 adjacent pinning site particles, corresponding to 20 distinct layers, positioned along a line that deviates 0°–30° from the c-axis. The direction of the splay along the ab-plane was chosen randomly. The obtained c-peaks are presented in Figure 8(a), where the tilting angle can be observed to have a significant effect on both the height and the shape of the c-peak. In particular, increasing the tilting angle above 20° is observed to decrease the height of the c-peak substantially. This can be attributed

to weak partial pinning resulting in substantially decreased P_{pin} at small values of θ. The double peak structures, on the other hand, result from optimal ratio between P_{cross} and P_{pin}.

The fragmented nanorods were modeled similarly to the 0° tilted nanorods, but the chain of adjacent pinning site particles was cut into 1–4 distinct pieces separated by single pinning site free layer. The number of layers was kept as close to 20 as possible, resulting in 20, $10+10=20$, $7+7+7=21$ and $5+5+5+5=20$ particles per nanorod. The nanorod fragments were independently positioned within their corresponding layers. The obtained c-peaks are presented in Figure 8(b). Increasing fragmentation results in substantially decreased magnitude of the c-peak while increasing the broadness of the peak. This particularly results from increased absolute values of the J_{c} for $\theta > 30°$ attributed to multicolumn pinning that increases both P_{cross} and P_{pin} for $\theta \gg 0$. These results coincide with the experimental observations presented in [9; 106].

4.1.4 Formation of the c-peak

In [**I**], the emergence of the c-peak for 4% BZO and BSO doped YBCO films has been studied as the magnetic field is increased from 0.5 T to 1 T. This is of particular interest because for the BZO nanorod the c-peak begins to emerge at 1 T field, while for BSO nanorods a prominent c-peak is present already at 0.5 T. Moreover, both the BZO and BSO nanorods are large enough to exclude the effects of natural pinning centers present in the surrounding YBCO lattice. The accessibility to TEM images along with the utilization of the vortex dynamics simulation model [29] enables one to rigorously study and explain of the origins of the experimentally observed $J_{\mathrm{c}}(\theta)$ curves under different magnetic fields on a microscopical level.

In order to effectively utilize the vortex dynamics simulation, the pinning structures of the associated films had to me modeled as accurately as possible. For this, the microstructure of the films was probed via BF-STEM, the resulting images of which are presented in Figure 9. The essential quantitative properties of the imaged nanorod lattices are summarized in Table 1. Although both of the nanorod types were observed to be fragmented, the individual fragments were positioned adjacent to each other effectively behaving as a single solid nanorod as seen from the images presented in 9. Thus, the effect of fragmentation in the simulations was neglected and only the differences in nanorod diameter and splay were taken into consideration. The essential simulation parameters are summarized in Table 2.

The simulated and experimentally measured $J_{\mathrm{c}}(\theta)$ curves for BZO and BSO doped YBCO films under 0.5 T and 1 T fields are presented in Figure 10. The simulation clearly captures the essential experimentally observed features and can consequently be used to analyze the underlying pinning mechanisms. In the case of the BZO nanorods, the absence of the c-peak under 0.5 T is due to dominating ef-

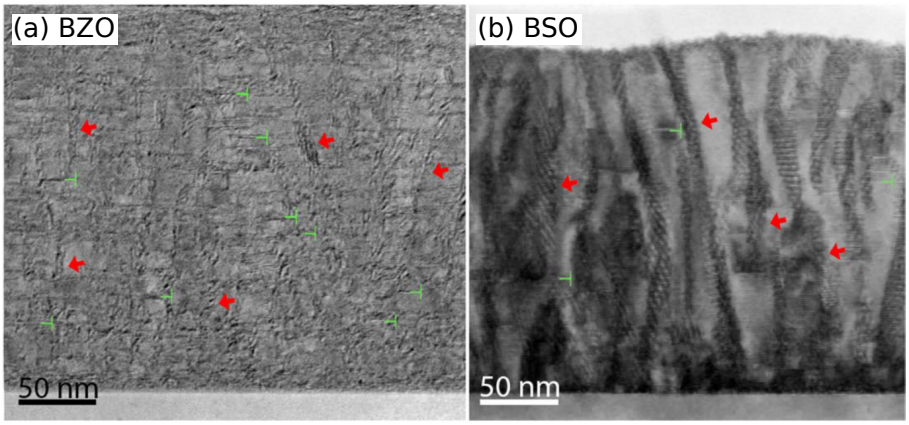

Figure 9. The cross-sectional BF-STEM images of YBCO films doped with 4% of (a) BZO, (b) BSO. The observed nanorods are pointed out as red arrows, while line defects are marked with green mark tones. Both figures are from **[I]**.

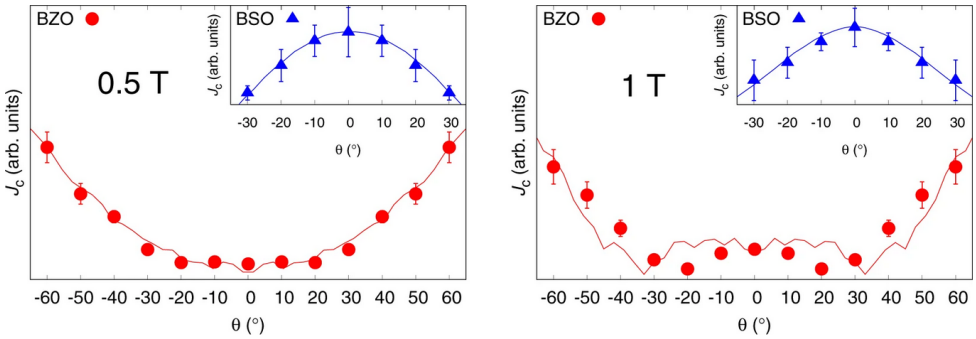

Figure 10. The simulated (points) and the experimentally measured (solid lines) $J_c(\theta)$ curves for 4% BZO and BSO doped YBCO films under 0.5 T and 1 T magnetic fields. The experimental data was measured at 10 K temperature. The nanorod lattices for the simulations were created according to the obtained BF-STEM images. Figure from **[I]**.

fect of P_{cross} over P_{pin} resulting from highly effective multicolumn pinning due to large nanorod areal density. That is, the evolution of $J_c(\theta)$ is mainly determined by

Table 1. A compilation of the nanorod parameters obtained from the BF-STEM images.

Nanorod	Diameter (nm)	Splay (°)	Length (nm)
BZO	6.8 ± 2.3	10.9 ± 0.3	29.1 ± 8.7
BSO	11.9 ± 3.2	8.8 ± 0.6	111.4 ± 17.6

$P_{\mathrm{cross}}(\theta)$, which vastly increases as a function of θ. The rise of the c-peak, on the other hand, is due to increased vortex-vortex interactions, that perturb the weak multicolumn pinning resulting in increased relevance of P_{pin} over P_{cross} in particular for high θ. In the case of the BSO nanorods, the presence of a prominent c-peak already under 0.5 T is explained by the reduced nanorod areal density, which makes the P_{pin} highly dominant over P_{cross}. The effect of P_{pin} is further increased by the strong pinning force resulting from the large radius of the BSO nanorods. Similar experimental observations for both BZO and BSO doped YBCO films have also been reported e.g. in [107; 52], respectively.

4.2 Optimizing nanorod areal density for pinning

As mentioned in section 2.4, the areal density of the nanorod lattice can be independently controlled from the associated nanorod radius by varying the dopant concentration of the PLD target. This raises a question, whether there exists a critical limit for the nanorod areal density, above which the pinning efficiency starts to degrade. In [**III**], the effect of areal density of BZO nanorods on the overall pinning performance of the YBCO film has been both theoretically and experimentally studied.

4.2.1 Theoretical approach

The presented study has been restricted by only considering vortices oriented parallel to the nanorods, that is along the c-axis of YBCO, as it is considered to be the limiting case when it comes to typical applications. In order to ease the theoretical treatment and the comparison to experimental observations, the nanorod areal density has been expressed in terms of a more profound measure, that is the average nanorod spacing (s) illustrated in Figure 11(a). It should be pointed out that there is not a simple proportionality between neither the dopant concentration in the target material and nanorod areal density nor s.

Firstly, a 1-dimensional potential energy distribution of a single vortex in the vicinity of two 3 nm radii BZO nanorods separated by varying distances s has been

Table 2. Parameters of the nanorod lattices used in the simulations.

Resembling nanorod	BZO	BSO
Diameter (nm)	3.4	6.0
Splay (°)	11	9
Number of nanorods	42	14
Number of vortices at 0.5 T	9	9
Number of vortices at 1 T	19	19

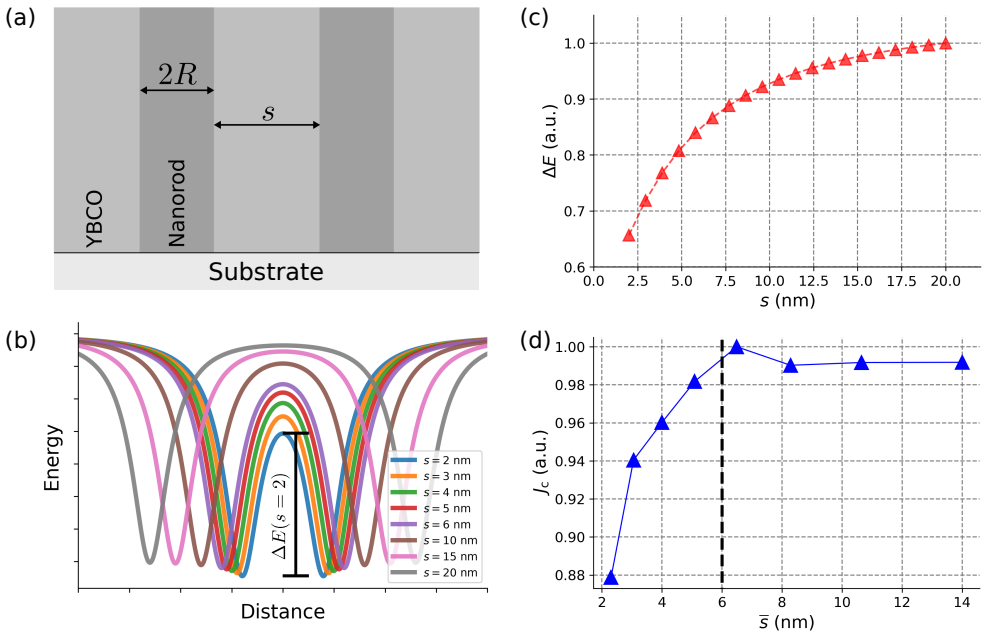

Figure 11. (a) A schematic illustration of the length scales associated with the nanorod lattice. (b) The 1-dimensional pinning potential experienced by a vortex in the vicinity of two nanorods with a radius $R = 3$ nm separated by varying distances (s). The vortex hopping potential (ΔE) is illustrated for the curve with $s = 2$. (c) The vortex hopping potentials as a function of s determined from the curves presented in (b). (d) The critical current density J_c as a function of average nanorod separation ($\bar{s}$) determined from the Metropolis simulations. The data points represent the minimum values observed for 30 independent statistical repeats for specific average s ($\bar{s}$). The dashed line illustrates the critical nanorod separation $\bar{s} = 2R$. Notice, that $\bar{s}$ is inversely proportional to the nanorod density or dopant concentration. Figures from **[III]**.

studied. The potential energy of the vortex was calculated using Eq. (10), or more explicitly as

$$\epsilon_{\mathrm{vp}}(r) = -\frac{\epsilon_0}{2} \sum_{i=0}^{N_{\mathrm{nr}}} \frac{R_i^2}{(r_i - r)^2 + 2\xi^2}, \tag{30}$$

where R_i and r_i are the radius and the position of the ith nanorod, respectively. The resulting potential energies as a function of spatial distance for different values of s are presented in Figure 11(b). The energy barrier between the nanorods, located at the center of the Figure 11(b), clearly decreases as the s is decreased. The height of this energy barrier evidently corresponds to the energy required for the pinned vortex to thermally hop between the nanorods and is thus from now onward referred to as the *hopping potential* (ΔE). The evolution of ΔE as a function of s is illustrated in Figure 11(c), where one observes that $\Delta E(s)$ decreases at a substantially greater

slope for lower values of s. Since $\Delta E(s)$ limits the pinning energy in Eq. (28), one can expect a rapid decrease of J_c as s is decreased sufficiently.

The s dependence of the J_c under 1 T applied field at 10 K temperature has been studied by simulating the vortex dynamics using the Metropolis-Hastings algorithm described in the section 3.6.2. The simulations were run within a $A = 100 \times 100\,\mathrm{nm}^2$ sized grid resembling the ab-plane of YBCO along which periodic boundary conditions were applied. The grid was initialized by positioning a total of N_nr nanorods with $R = 3\,\mathrm{nm}$ semi-randomly within the grid, so that the minimum distance between the nanorods was greater than $0.7 \cdot \sqrt{A/N_\mathrm{nr}}$. Thus, the nanorods form a periodic lattice with some random variation corresponding to experimental observations. Since the distances between the nanorods are not exactly fixed, one has to use average nanorod separation calculated as $\overline{s} = \sqrt{A/N_\mathrm{nr}} - 2R$.

After positioning of the nanorods, a total of $N_\mathrm{v} = BA/\Phi_0$ vortices were accommodated one at a time to the minimum energy positions of the grid. These initial positions were determined as the positions at which the sum of the pinning potential (Eq. (30)) and the vortex-vortex interaction potential, given by

$$\epsilon_\mathrm{vv}(\mathbf{r}) = \sum_{i=0}^{N_\mathrm{v}} \epsilon_0 \begin{cases} \mathrm{K}_0\left(\frac{|\mathbf{r}_i - \mathbf{r}|}{\lambda(T)}\right), & \text{when } |\mathbf{r}_i - \mathbf{r}| > \xi \\ 2 \cdot \mathrm{K}_0\left(\frac{\xi(T)}{\lambda(T)}\right), & \text{when } |\mathbf{r}_i - \mathbf{r}| \leqslant \xi \end{cases}, \tag{31}$$

in accordance with the previously introduced Eq. (7), has a global minimum.

After the above described initialization of the grid, a potential of the form

$$\epsilon_\mathrm{appl} \sim Jx \tag{32}$$

was applied to the vortices resulting from the applied current density (J) through the superconducting lattice. The parameter x represents the projection of the vortex position vector $\mathbf{r}$ along the x-axis of the grid. The total potential experienced by a vortex at position $\mathbf{r}$ thus becomes the sum of the potentials (30), (31) and (32). The system was then evolved according to the Metropolis-Hastings algorithm with the excitation parameter Δr (see section 3.6.2) set to 0.037 nm so that the acceptance probability for $J = 0$ was around 10% and for $J \sim J_\mathrm{c}$ around 50%. The J_c was searched using the bisection method with the criterion that for $J = J_\mathrm{c}$ the average position of the vortices has changed more than R over a total of $N_\mathrm{v} \cdot 500$ iterations. The J_c for specific $\overline{s}$ was determined as the minimum of 30 statistical repetitions.

The obtained $J_\mathrm{c}(\overline{s})$ curve is presented in Figure 11(d), further confirming the previous expectation that s has a critical limit below which J_c starts to decrease. According to Figure 11(d), this limit corresponds to $\overline{s} \approx 2R$. In summary, the theoretical consideration suggests that the vortex pinning efficiency is maximized for nanorod lattices where, the average distance between the nanorods, as measured from edge to edge, equals to their corresponding diameter.

4.2.2 Experimental evidence

The effect of nanorod areal density on vortex pinning properties has been previously experimentally studied in [57] for PLD deposited BSO nanorods. However, the maximum concentration of BSO in the used PLD target was only 9%. Due to the significantly larger radius of BSO nanorods when compared with BZO, the proposed critical limit $\overline{s} \approx 2R$ was not reached. In [108] the effect of BZO nanorod concentration on pinning force has been carried out, but pinning force has been determined only under 1.5 T field, under which one is unable to make conclusions about the vortex pinning performance since the effect of zero field current density is significantly present.

In order to get reliable experimental evidence about the critical limit solely in terms of vortex pinning performance, a set of 0–14% BZO doped YBCO films were deposited. These films were expected to contain nanorod lattices with varying areal densities but with the same nanorod radii of $R \approx 3$ nm. This was further verified by imaging the microstructure of 4%, 8% and 12% BZO doped films with BF-STEM. The obtained results are summarized in Table 3. The nanorod radius was indeed observed to remain constant while the nanorod separation, corresponding to the parameter $\overline{s}$ in the previous section, decreases as a function of initial dopant concentration. For the 12% doped sample around 1/10 of the film was observed to contain anomalous regions inside which the BZO nanorods were aligned along the ab-plane of YBCO coinciding with the theoretical model presented in [16] along with similar experimental observations [109]. This suggests that there also exists a structural limit for the nanorod concentration, above which the c-axis oriented growth gets disturbed. It should be noted, that for the c-axis oriented nanorods in 12% doped sample, that still forms 9/10 of the film, the nanorod separation roughly equals to the diameter of the nanorods that was speculated to be the critical limit in terms of vortex pinning.

The original magnetically measured $J_c(B)$ curves for all of the grown films at 10 K are presented in Figure 12(a). In order to compare the pure pinning performance between the samples, the effect of reduced zero field critical current as a function of dopant concentration was neglected by normalizing the measured $J_c(B)$ curves so

Table 3. The average parameters of the nanorod lattices observed from the TEM images of 4%, 8% and 12% doped samples. For the 12% doped sample around 10% of the nanorods are abnormally aligned along the YBCO ab-plane.

Initial concentration (%)	Radius (nm)	Length (nm)	Separation (nm)	Splay (°)
4	2.95 ± 0.35	49.9 ± 4.7	17.6	16
8	2.75 ± 0.55	32.1 ± 7.9	7.1	14
12 (90% along c-axis)	2.7 ± 0.50	29.8 ± 15	5.6	10
12 (10% along ab-plane)	4.95 ± 0.65	25.5 ± 5.3	14.5	0–20

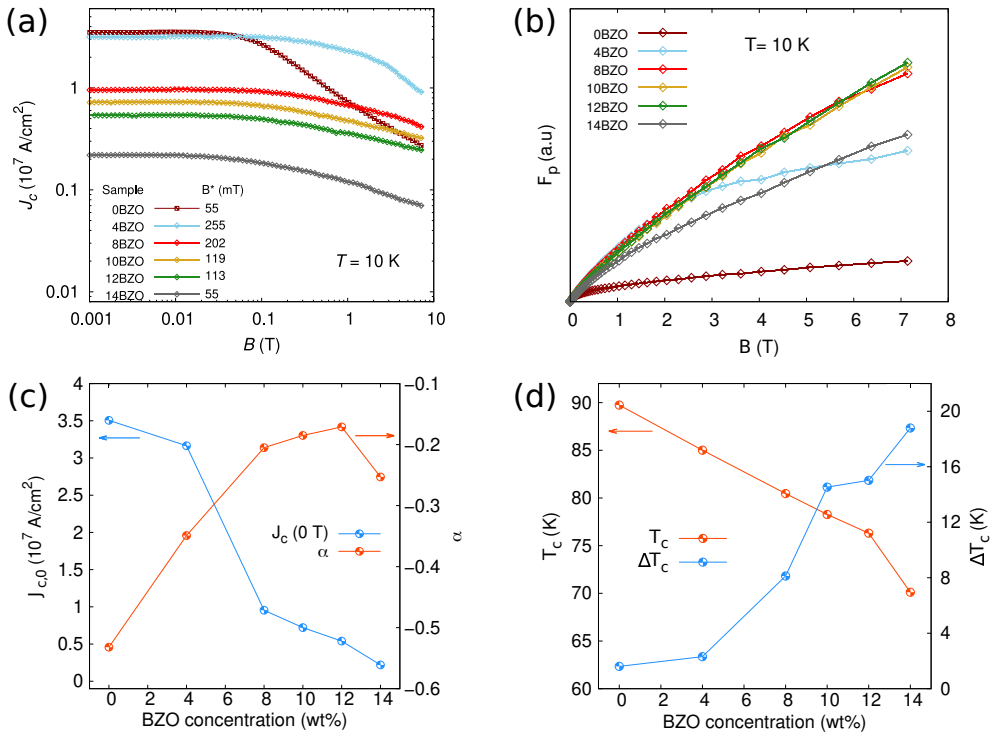

Figure 12. (a) The magnetically measured critical current field dependences at 10 K for samples with different BZO concentration- The applied magnetic field is oriented along the YBCO c-axis. (b) The calculated pinning forces $F_\mathrm{p} = J_\mathrm{c} \cdot B$ derived from the measured $J_\mathrm{c}(B)$ curves after normalization of $J_\mathrm{c}(B = 0)$ to 1. This was done in order to remove the effect of reduced zero field J_c as a function of nanorod concentration. (c) The zero field current and α-parameter determined from the $J_\mathrm{c}(B)$ curves. (d) The magnetically measured critical temperatures and the associated transition widths (ΔT_c). Figures from **[III]**.

that $J_\mathrm{c}(B = 0) = 1$ and calculating the corresponding pinning force $F_\mathrm{p} = J_\mathrm{c} \cdot B$ as a function of B. The obtained normalized $F_\mathrm{p}(B)$ curves are presented in Figure 12(b), where one can observe that F_p increases as a function of nanorod concentration up to $\sim$ 8% in a wide magnetic field range, above which it starts to even out. The F_p for the 14% BZO doped sample is substantially lower in the full magnetic field range when compared with 8–12% doped samples. However, whether this is due to increased aligment of BZO nanorods along the ab-plane of YBCO, as observed in the TEM images for the 12% doped sample, remains unclear. However, in the case of 12% doped sample it was observed that the regions of misaligned BZO nanorods consisted only a minor fraction of the film. Outside these regions, the BZO nanorods were aligned in a similar way, but denser, when compared with the samples of lower BZO concentrations. Since the regions of misaligned BZO nanorods were observed to be large when compared with the diameter of the vortex core, they should not

have a significant effect on vortex pinning along the c-direction. This suggests, that it is indeed the increased nanorod concentration that degrades F_{p} of the 14% doped sample.

The above conclusions were further confirmed by studying the vortex induced decay rate of J_{c} as a function of B above the low-field plateau. This is typically assumed to be of the form $J_{\mathrm{c}} \propto J_{\mathrm{c},0} \cdot B^{\alpha}$, where $J_{\mathrm{c},0}$ is the associated zero field current density. Taking 10-base logarithm of both sides gives $\log(J_{\mathrm{c}}) = \log(J_{\mathrm{c},0}) + \alpha \cdot \log(B)$, where the parameter α can be determined as a slope of the measured $J_{\mathrm{c}}(B)$ presented in a log-log scale as in Figure 12(a). Evidently α is negative and approaches zero for increased pinning performance. The evaluated α parameters and $J_{\mathrm{c},0}$s are presented in Figure 12(c) as a function of the dopant concentration associated with the corresponding sample. Here, the expected converse behaviour between α and $J_{\mathrm{c},0}$ is well illustrated as increasing the dopant concentration simultaneously improves the pinning performance and degrades $J_{\mathrm{c},0}$. In particular, α increases rapidly up to 8% above which it flattens, reaching maximum around 12% of BZO concentration. Most importantly, the α for 14% is substantially lower when compared with 8–10% concentrations. This is exactly similar tendency that was observed for the F_{p} further confirming the previous conclusions that the areal density of the nanorods has a critical limit above which the pinning performance is degraded. Based on the BF-STEM results presented in Table 3, this limit corresponds to the theoretically predicted average nanorod separation of $\overline{s} \approx 2R$.

It should be pointed out that the experimental results presented in Figures 12(b)–(c) suggest, that the pinning performance substantially increases as the nanorod concentration is increased up to the critical limit. However, this effect is not present in the results of the Metropolis-Hastings simulations presented in Figure 11(d), according to which the J_{c} remains somewhat constant below the critical nanorod density. Notice, that the nanorod average separation $\overline{s}$ used in Figure 11(d) is inversely proportional to the nanorod density or the dopant concentration. The observed discrepancy, however, can be explained by the initialization of the simulation grid described above. Since the vortices were initially positioned to the energy minima of the grid, that is within the nanorods, the presented simulation model neglects the effect of crossing probability (P_{cross}) discussed in section 4.1.4. Thus, the simulation expectedly results in constant J_{c} below the critical nanorod concentration.

4.2.3 Implications of the results

As concluded above, increasing the areal density of nanorods above a critical limit ultimately results in decreased pinning properties. Thus, the maximum achievable matching field and the associated pinning performance is fundamentally limited. The limit for the matching field can be easily approximated with the above presented results as

$$B_{\phi,\max} \approx \frac{\Phi_0}{(2R)^2}, \tag{33}$$

which in the case of BZO nanorods associated with $R = 3\,\text{nm}$ results in $B_{\phi,\max} \approx 57\,\text{T}$. Such a high matching field evidently does not limit the applications using HTS wires.

4.3 Study of a multilayer structure designed for high-field range

In **[II]**, the high-field performance of YBCO films have been tried to increase by applying ML structures consisting of alternating layers of 4% and 12% BZO doped YBCO. The specific dopant concentrations were chosen based on previous studies, in which the 4% concentration has been observed to result in the highest overall $J_\text{c}(B)$ while the 12% concentration maximises the pinning performance [**VII**]. Thus, the combination of these is an obvious initial guess for the optimal layer structure in the high-field range.

4.3.1 Experimental realization and measurements

The PLD method has been utilized to deposit a total of three ML structures with 4, 8, and 20 adjacent layers labeled as 4ML, 8ML and 20ML, respectively. A 4% and a 12% BZO doped single layer YBCO films, referred as 4BZO and 12BZO, have further been deposited in order to deduce whether the ML structures have increased J_c in the first place. All the samples were grown with the same number of laser pulses presumably resulting in films with similar overall thicknesses but varying individual layer thicknesses as illustrated in Figure 13. The presumed constant overall thicknesses of the films were further confirmed by AFM measurements.

The experimentally measured $J_\text{c}(\theta)$ curves at 40 K under 0.5–8 T applied magnetic fields are presented in Figure 14(a)–(f), respectively. The 4BZO film shows substantial c-peak in the full field range as expected. In the case of the 12% BZO doped single layer film, the c-peak emerges only above 6 T. This can be attributed to enhanced multicolumn pinning resulting from high areal density of the nanorods, which increases the J_c more prominently for higher θ in the absence of substantial vortex-vortex interactions. Moreover, the absolute value of J_c for the 12BZO is

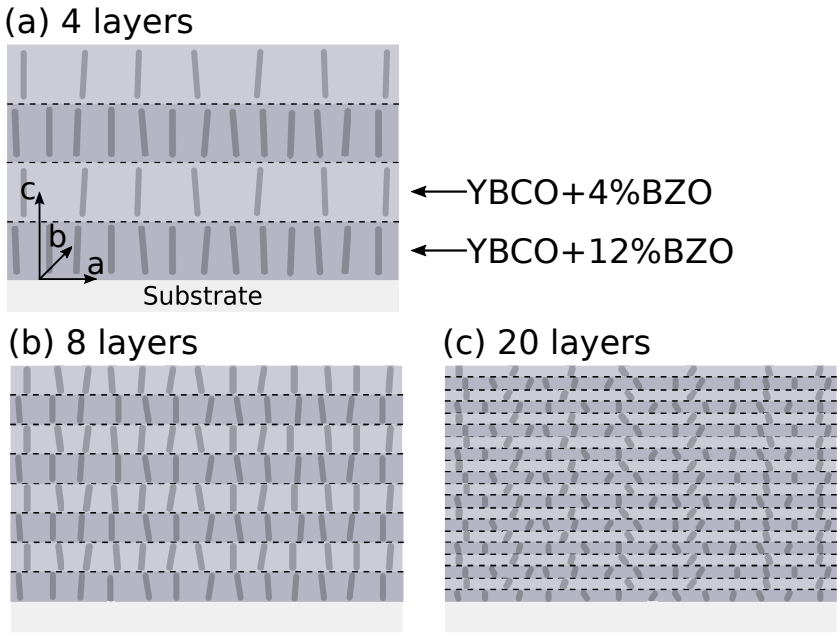

Figure 13. Schematic illustrations of (a) 4ML, (b) 8ML and (c) 20ML samples with alternating layers of 4% and 12% BZO doped YBCO (4BZO and 12BZO, respectively).

staggering $\sim$3 times lower in the full angular and field range when compared with 4BZO sample. This can be attributed to the effects discussed in section 2.4, that is reduced superconducting cross-sectional area and more pronounced strain fields within YBCO lattice due to doping.

There is no c-peak to be observed for any of the ML films. This can be associated with the presence of increased number of short randomly distributed nanorods, which highly favor multicolumn pinning at higher angles. More importantly, all of the ML films outperform the corresponding single layer films in full angular range above 6 T. Surprisingly, the 4ML film is observed to outperform the 4BZO under 0.5 T field. This rather contradictory result suggests that the improved J_c of the ML film does not result from enhanced pinning properties but from improved overall crystalline quality of the ML structures. Furthermore, increasing the number of layers systematically decreases the J_c without affecting the shape of the associated $J_c(\theta)$ curves. These observations allows one to make crucial conclusion about the underlying mechanisms behind the significantly improved current carrying properties for the studied ML films presented in the following sections.

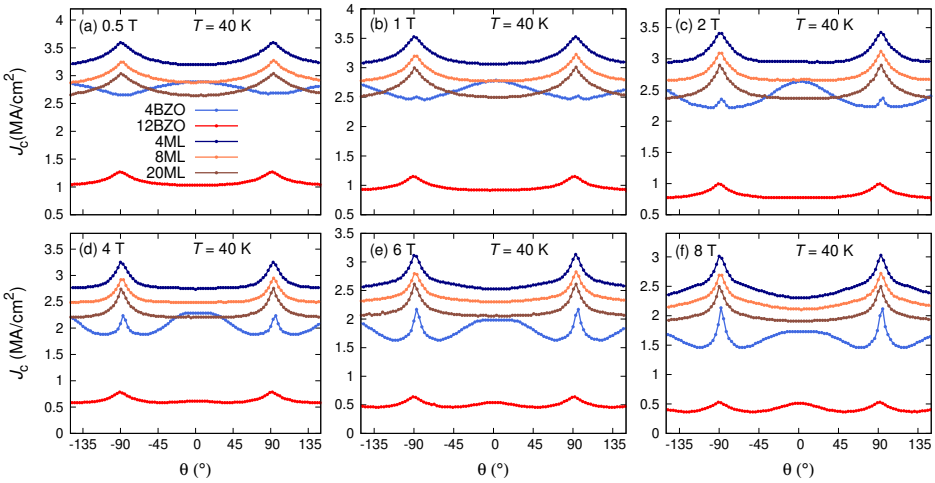

Figure 14. The experimentally measured critical current anisotropy curves for the single layer films of 4% and 12% BZO doped YBCO (4BZO and 12BZO, respectively) and the 4, 8 and 20 layer ML films (4ML, 8ML, 12ML, respectively) under various fields at 40 K temperature. The $\theta = 0$ corresponds to direction along the c-axis of YBCO unit cell. Figures from **[II]**.

4.3.2 Vortex dynamics in multilayer films

In order to explain the experimental observations presented above, the vortex dynamics limited critical current and the associated anisotropy of the ML structures has been studied using the simulation presented in [29]. The simulations were performed for 4BZO, 12BZO and 4ML. The pinning structures were modelled according to the microstructural information obtained from BF-STEM images of single layer films 4BZO and 12BZO. Details of the used pinning structures are summarized in Table 4 and further visualized in Figure 15. The simulated normalized vortex dynamics limited critical current anisotropies for both of the single layer films under various magnetic fields are presented in Figure 16(a)–(b), respectively. The simulations correspond well to the experimentally measured $J_c(\theta)$ curves under 0.5–2 T fields presented in Figure 14(a)–(c). The main similarities between the simulations and experiments for the 4BZO are, in particular, the presence of the c-peak already in low magnetic fields, which quickly intensifies as the field is increased. For the 12BZO, on the other hand, the c-peak is absent in the low-field but slowly emerges as the field is increased. The good correspondence between the simulations and the experiments further validates the used model, which is to be applied to study the vortex dynamics within the 4ML sample.

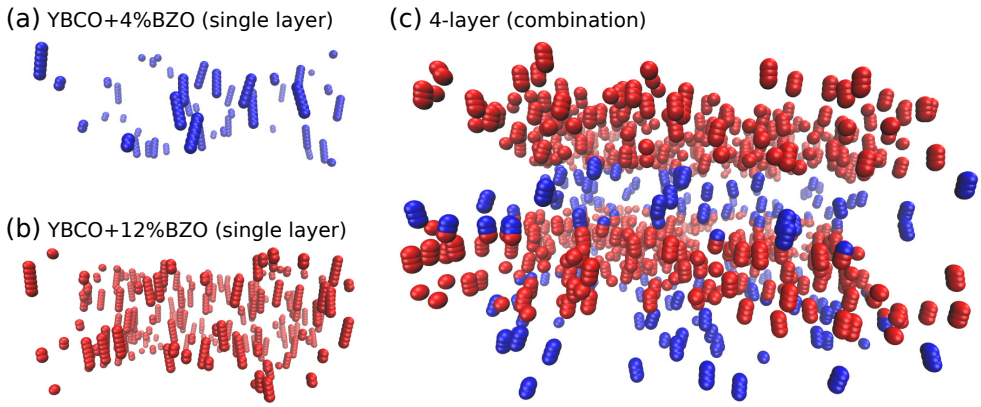

Figure 15. Schematic illustrations of the pinning structures used in the simulations of (a) 4BZO, (b) 12BZO and (c) 4ML film. The 4ML that is a combination of the structures presented in (a) and (b). Figures from **[II]**.

The simulated normalized $J_c(\theta)$ curves for the 4ML sample under 0.2 T and 1 T applied fields are presented in Figure 16(c). Unfortunately, technical reasons prevented the simulation of the $J_c(\theta)$ above 1 T. However, this turned out not to be a major issue since a lot can be deduced from the obtained curves as well. The shapes of the simulated and the measured $J_c(\theta)$ curves correspond to one another with good extent with the absence of the c-peak and broadening ab-peak as a function of applied field. To this extent, the simulation seems to capture the essential aspects of vortex dynamics within the 4ML structure. However, the experimentally observed absolute values of $J_c(\theta = 0)$ are inconsistent with the simulations. In particular, the simulations predict a substantially smaller $J_c(\theta = 0)$ for the 4ML when compared with the 4BZO in the low-field range. Furthermore, the simulation suggests that the $J_c(\theta = 0)$ of 4ML would be even smaller when compared with the 12BZO under 1 T field. Since the used simulation model addresses only the vortex dynamics limited J_c, the observed discrepancies suggest that the experimentally verified substantial enhancement of J_c for the ML structures results from increased zero field J_c. Since all the ML films contain 50% of both 4BZO and 12BZO, this improvement cannot be attributed to the increased cross-sectional area discussed in section 2.4. Thus, the improved J_c of the ML structures has to be a manifestation of increased crystalline quality. More quantitative arguments to further validate this conclusion are provided in the following section.

4.3.3 Improved crystalline quality of the multilayer films

In this section, the proposed improved crystalline quality associated with the ML films will be quantitatively addressed. A key observation regarding to this is that the

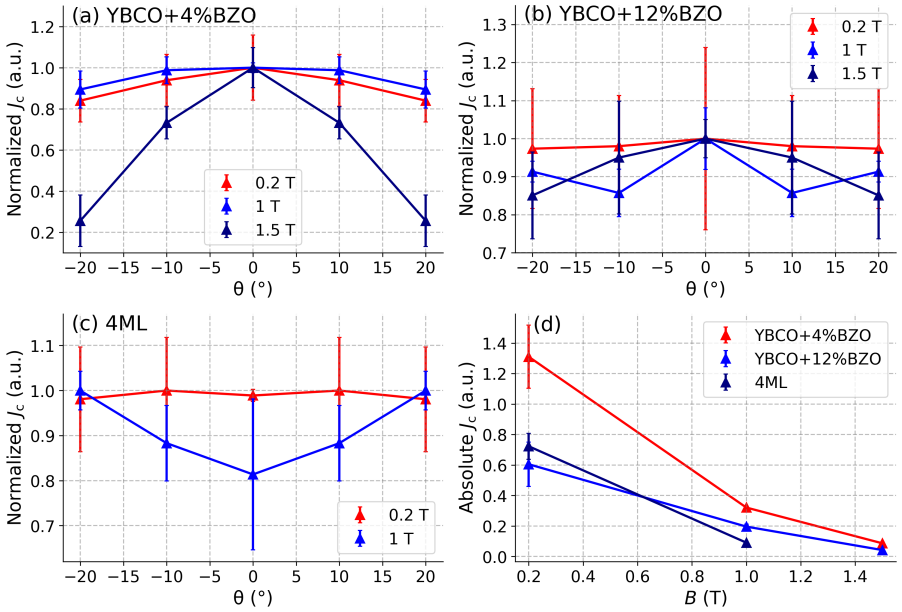

Figure 16. The normalized simulated vortex dynamics limited critical current anisotropies under various magnetic fields for (a) 4BZO, (b) 12BZO and (c) the 4ML cosisting of alternating layers of 4BZO and 12BZO. (d) The simulated absolute values of the vortex dynamics limited critical current as a function of magnetic field. Data for the figures is taken from **[III]**.

measured J_c for the ML structures is observed to decrease as a function of the layer thickness. This particular trait motivates one to explore the theory of film growth, in particular the concept of critical film thickness (t_c). The t_c is defined as the thickness above which it becomes energetically more favourable for the formed lattice to release substrate induced strain via formation of dislocations. The t_c can be evaluated

Table 4. The simulation parameters based on the TEM images of the 4% and 12% BZO doped single layer films (4BZO and 12BZO, respectively). *For the used simulation model, the parameter c also corresponds to the number of adjacent layers. †For the 4-layer structure (4ML), the pinning structure is a combination of the structures presented for the 4% and 12% BZO doped single layer films.

	4BZO	12BZO	4ML
Total grid size* $(a \times b \times c)$ nm^3	150×150× 30	150×150×30	200×200×60
Single layer size* $(a \times b \times c)$ nm^3	150×150× 30	150×150×30	200×200×15
Number of nanorods	41	186	combination†
Nanorod radius (nm)	2.95	2.7	combination†
Nanorod fragmentation	$c/5$	40% of $c/14$ and 60% of $c/5$	combination†
Nanorod splay	16°	10°	combination†

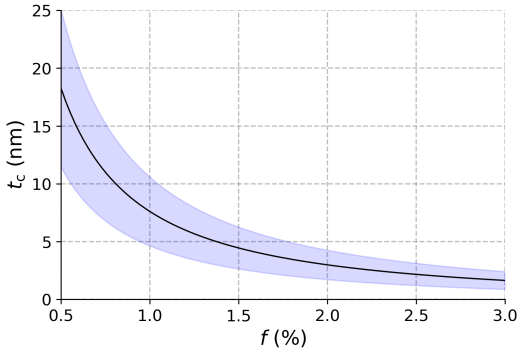

Figure 17. The numerically evaluated critical thickness as a function of lattice mismatch based on Eq. (34). The shaded region represents maximum variation of the critical thickness with respect to the parameters $b \in$ [2.34 Å, 5.34 Å], $\nu \in$ [0.2, 0.4], $\beta \in$ [3.5, 4.5] and $\theta \in$ [80°, 100°]. Figure from **[II]**.

by numerically solving the equation [110]

$$t_\mathrm{c} = \frac{(1 - \nu\cos^2\theta)b}{8\pi f(1+\nu)} \ln\left(\frac{\beta t_\mathrm{c}}{b}\right), \tag{34}$$

where f is the lattice mismatch between the unit cells of the deposited material and the substrate, ν is the Poisson ratio for the film, b is the magnitude of the Burgers vector associated with a dislocation, β is the cutoff radius of the dislocation core and θ is the angle between the dislocation line and Burgers vector. The length of the Burgers vector is typically on the scale of the lattice parameters of the material. Here, the average of the a and b-lattice parameters of YBCO has been used resulting in $a_\mathrm{YBCO} = 3.84\,\text{Å}$. The Burgers vector was then estimated to be in the range of $b = a_\mathrm{YBCO} \pm 2.5\,\text{Å}$. The ranges for the rest of the parameters were deduced from the previous studies associated with similar crystal systems to that of YBCO, suggesting that $\nu = 0.3 \pm 0.1$, $\beta = 4 \pm 0.5$ and $\theta = 90° \pm 10°$ [110; 111; 112]. The resulting numerically evaluated t_c as a function of f is presented in Figure 17.

In order to evaluate t_c for the layers of the ML structures, that is for the 4BZO grown on top of the 12BZO and vice versa, one has to somehow evaluate the associated lattice mismatch. This is most conveniently done by first calculating an effective lattice parameter

$$\overline{a}(\rho) = \rho \cdot a_\mathrm{BZO} + (1-\rho)\cdot a_\mathrm{YBCO}, \tag{35}$$

where ρ is the associated dopant concentration and $a_\mathrm{BZO} = 4.17\,\text{Å}$ is the lattice parameter of BZO unit cell and $a_\mathrm{YBCO} = 3.84\,\text{Å}$ as stated above. One obtains effective lattice parameters of $\overline{a}_{4\%} = 3.85\%$ and $\overline{a}_{12\%} = 3.88\%$ for the 4BZO nad 12BZO, respectively. The associated lattice mismatch can be further calculated as

$f = (\overline{a}_{4\%} - \overline{a}_{12\%})/\overline{a}_{4\%}$, resulting in $f \approx 0.8\%$. One can then evaluate the corresponding t_c from Figure 17 to be around 10 nm.

Since the average total thicknesses of the ML films is around 200 nm, the associated layer thicknesses for the 4ML, 8ML and 20 ML films are 50 nm, 25 nm and 10 nm, respectively. As the t_c was estimated to be around 10 nm, it can be concluded that the layer thickness in the 20ML is far too small for the strain to relax. This is most likely the case for the 8ML sample as well. Thus, increasing the number of layers increases the lattice strain which ultimately results in observed decrease of J_c as the the total number of layers is increased above a threshold value. However, this conclusion assumes that the strain relaxation induced dislocations at the surface of the film have negligible effect on the growth of the above deposited layer. It has been proposed, that the surface epitaxy of an YBCO layer is improved as a function of heat conducted through the preceding layers [113]. This mechanism is likely to take place during the ~ 2 min time period between the deposition of adjacent layers associated with this work, among with several other studied where a similar effect has been observed [77; 114; 115]. This proposal is in line with the above presented results and it also explains why the ML films have higher J_c when compared with the single layer films in the first place. That is, as the single layer films are deposited in a single setting, the number of dislocations on the surface of the film increases as the thickness of the film grows. This increasingly aggravates the affiliation of new unit cells as the film thickness grows resulting in degrading crystalline quality with increasing film thickness as discussed in section 2.5.

In conclusion, the ML structures studied in this work provide higher J_c because the deposition of the ML structure happens to increase the average crystalline quality of the ML films when compared with the single layer films. This demonstrates the importance of computational methods to determine the true origin of the improved superconducting properties. Significantly greater improvement in superconducting properties can be expected for better optimized ML structures.

4.4 Optimization of a bilayer structure

As concluded in the section 2.4, the critical current of the superconductor can be potentially increased, in particular under mid-field range ($B \approx 0.1 - 2$ T), by applying ML structures for which the APC profiles within the superconducting lattices vary between the adjacent layers. In [**V**], a bilayer structure consisting of a single layer of intrinsic YBCO and another layer of BZO doped YBCO as illustrated in Figure 18 has been studied. Such a structure is arguably the simplest possible ML structure both in terms of analysis and experimental realization. The main objective of the associated work was to quantitatively study whether or not such a bilayer structure would have increased J_c in the mid-field range oriented along the c-axis of YBCO when compared with the corresponding single layer film and evaluate the optimal

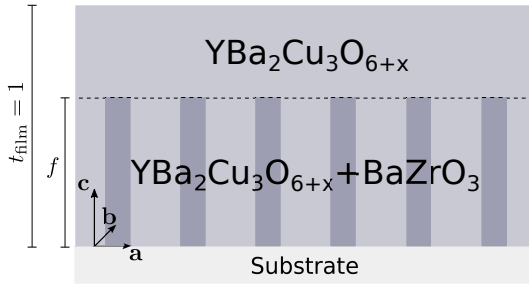

Figure 18. A schematic illustration of the proposed bilayer structure. Figure from **[V]**.

layer thicknesses.

The total thickness of the bilayer film (t_{film}) is ultimately an arbitrary quantity, since both the pinning force and the Lorentz force are directly proportional to it. Consequently, one can fix $t_{\mathrm{film}} = 1$ and express the thickness of the BZO doped layer with a dimensionless parameter $f \in [0, 1]$ representing the ratio between the thicknesses of the adjacent layers. The ultimate task is to find f for which the overall J_{c} of the bilayer structure has maximum value.

The overall J_{c} has to be limited by either the zero field critical current density ($J_{\mathrm{c},0}$) or the vortex dynamics limited critical current density ($J_{\mathrm{c,v}}$). Interestingly, both the $J_{\mathrm{c},0}$ and the $J_{\mathrm{c,v}}$ have strong dependence on f. In particular, since the presence of APCs decreases the cross-sectional area of the superconductor, $J_{\mathrm{c},0}$ evidently decreases when f is increased. Contrary to this, the pinning force is directly proportional to the length of the nanorod and thus $J_{\mathrm{c,v}}$ increases from $J_{\mathrm{c,v}}(f = 0) = 0$ to the maximum value $J_{\mathrm{c,v}}(f = 1)$ as a function of f. These observations already suggest that there should be an optimal f, which is found at the crossing points of the functions $J_{\mathrm{c},0}(f)$ and $J_{\mathrm{c,v}}(f)$, given that $J_{\mathrm{c,v}}(1) > J_{\mathrm{c},0}$. These ideas are schematically illustrated in Figure 19. In the following sections rigorous mathematical expressions for the aforementioned functions will be derived, ultimately enabling the evaluation of the optimal f.

4.4.1 Vortex dynamics limited critical current

The most reliable way to address the formula for the function $J_{\mathrm{c,v}}(f)$ is to utilize the 3D vortex dynamics simulation presented in section 3.6.1. In order to do this, the $J_{\mathrm{c,v}}$ has been simulated for grids corresponding to different values of f. The sizes of the grids were set to $200 \times 200 \times 45\,\mathrm{nm}^3$, where the number of particles per vortex line was set to 10. The f dependence of the grid was considered by limiting the number of particles per nanorod between 0 and 10, similarly as illustrated in Figure 20. The radius and the areal density of the nanorods were kept at constant values of $R = 3\,\mathrm{nm}$ and $\sigma = 22 \cdot 10^{-4}\,\mathrm{nm}^{-2}$, resembling the $\sim 4\%$ BZO doped YBCO films.

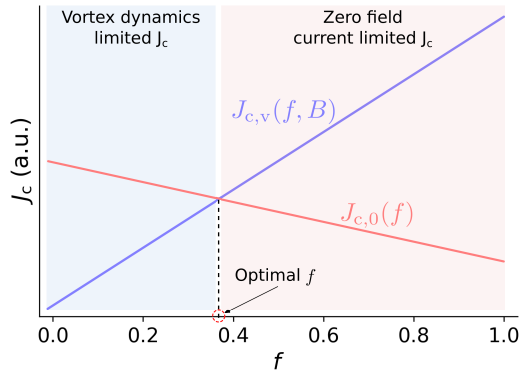

Figure 19. A schematic illustration of how the overall J_c is always limited by either $J_{c,0}(f)$ or $J_{c,v}(f)$. The optimal f can be found at the crossing point of the associated functions. Figure from **[V]**.

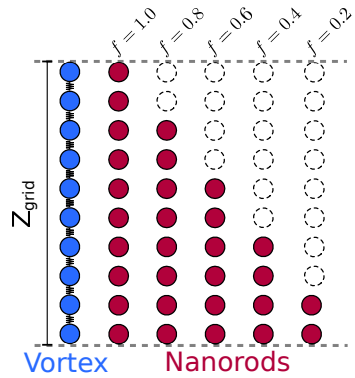

Figure 20. A schematic illustration of how the nanorods within a bilayer structure corresponding to specific f were implemented in the MD simulation. Figure from **[V]**.

All the used simulation parameters are presented in Table 5.

The simulated $J_{c,v}$s as a function of f under various magnetic fields in the mid-field range are presented in Figure 21(a). The shapes of the functions $J_{c,v}(f)$ seem to be linear in nature for small fields but start to show slight exponential features as the field is increased above 1 T. The observed partly linear-exponential behaviour of $J_{c,v}(f)$ is expected, since according to the Boltzmann statistics $J_c \propto e^{E_{vp}/kT}$, where E_{vp} is the associated pinning potential. The exponential function, which can be further approximated by the first term of the associated Taylor expansion, yields $J_c \propto E_{vp}$. Since the vortices in the simulations were oriented parallel to the nanorods, one can exclude the complex effects of partial and multicolumn pinning on the pinning potential E_{vp} evidently resulting in $E_{vp} \sim f$, where the observed results clearly

follow.

Based on the previous remarks, the simulated $J_{\mathrm{c,v}}(f)$ curves under all applied magnetic fields were approximated with a linear function $J_{\mathrm{c,v}} = \alpha \cdot f$. Most importantly, this function satisfies the evident boundary condition $J_{\mathrm{c,v}} = 0$ for $f = 0$. Note, that the slope $\alpha = \Delta J_{\mathrm{c,v}}/\Delta f$, which results in $\alpha = J_{\mathrm{c,v}}(f = 1)$ when estimating the change of the associated parameters over the whole range of $f \in [0, 1]$. Consequently, an empirical relation may be proposed

$$J_{\mathrm{c,v}}(f, B) = J_{\mathrm{c,v}}(f = 1, B) \cdot f, \tag{36}$$

where $J_{\mathrm{c,v}}(f = 1, B)$ ideally corresponds to $\alpha(B)$.

The main panel of Figure 21(b) presents the simulated $J_{\mathrm{c,v}}(f = 1)$ as a function of B. In order to find an analytic expression for $J_{\mathrm{c,v}}(f = 1, B)$, a function of the form $J_{\mathrm{c,v}}(f = 1) = (B/0.1\ \mathrm{T})^n$ was fitted to the corresponding data via parameter n. This particular function was chosen because it satisfies the condition $J_{\mathrm{c,v}}(f = 1) = 1$ for $B = 0.1$ T resulting from the initial normalization of the simulated $J_{\mathrm{c,v}}(f)$ by the maximum obtained $J_{\mathrm{c,v}}$ for $f = 1$ under $B = 0.1$ T. This also simplifies

Table 5. The parameters used in the simulations of the bilayer structures. *Varies according to desired f.

Parameter	Value
Grid (nm^3)	200×200×45
Particles per vortex line	10
Cut-off radius (nm)	50
Magnetic field (T)	0.1–2
Number of vortices	1–38
Density of nanorods (nm^{-2})	$22 \cdot 10^{-4}$
Number of nanorods	88
Nanorod radius (nm)	3
Particles per nanorod*	1–10
Time-step (s)	$2 \cdot 10^{-4}$
Iterations	6000
Statistical repeats	10
Mass (kg)	10^{-16}
Drag coef. (kg/s)	$2 \cdot 10^{-14}$
Spring constant k (N/m)	$1 \cdot 10^{-10}$
Penetration depth λ (nm)	150
Coherence length ξ (nm)	1.5
Anisotropy const. γ	5
Energy const. ϵ_0 (J/m)	$2.8 \cdot 10^{-11}$

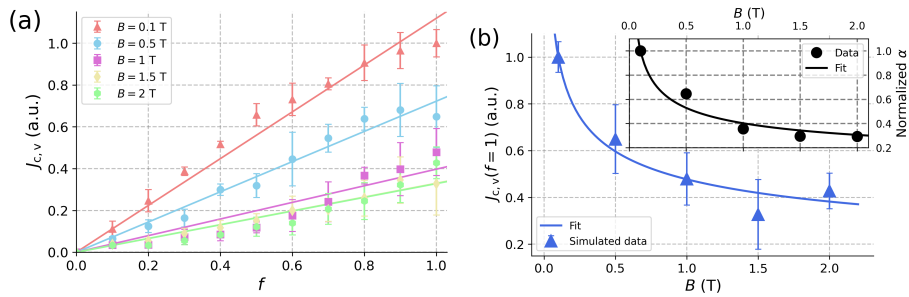

Figure 21. (a) The simulated $J_{\mathrm{c,v}}(f)$ curves under various magnetic fields. The data points and the error bars represent the average value and standard deviation of 10 statistically repeated simulations. For future convenience, the curves have been normalized by the highest simulated value of $J_{\mathrm{c,v}}$, which was obtained for $f = 1$ under 0.1 T. The solid lines represent the fits of a function $J_{\mathrm{c,v}} = \alpha \cdot f$ to the corresponding simulation data. (b) The main panel presents the simulated $J_{\mathrm{c,v}}(f = 1)$ as a function of the field. The inset illustrates the field dependency of the calculated fitting parameter α. The solid lines represent the fits of a function $J_{\mathrm{c,v}}(f = 1) = (B/0.1\ \mathrm{T})^n$ to the corresponding data points. Figures from **[V]**.

the necessary estimation of the absolute value of $J_{\mathrm{c,v}}(f = 1)$ in the future, since the simulation run under $B = 0.1\,\mathrm{T}$ contained only a single vortex. The fit of the associated function via parameter n to the simulated $J_{\mathrm{c,v}}(f = 1, B)$ data is illustrated as a solid line in Figure 21(b), for which the obtained value fitting parameter was $n = -0.32 \pm 0.03$.

The field dependence of the fitting parameter α has been further estimated. For this, the function $J_{\mathrm{c,v}} = \alpha \cdot f$ was first fitted to the simulation data under different magnetic fields via parameter the α as presented by the solid lines in Figure 21(a). The field dependence of the obtained fitting parameters are further illustrated in the inset of Figure 21(b), where the function $\alpha = (B/0.1\ \mathrm{T})^n$ has been fitted via parameter n similarly as was done for the previously discussed $J_{\mathrm{c,v}}(f = 1, B)$. In the case of α, one obtains the fitting parameter $n = -0.4 \pm 0.04$.

Since ideally $J_{\mathrm{c,v}}(f = 1, B) = \alpha(B) \approx (B/0.1\ \mathrm{T})^n$, the $J_{\mathrm{c,v}}(f = 1, B)$ in Eq. (36) was chosen to be modeled using the average of the fitting parameters n obtained independently for $J_{\mathrm{c,v}}(f = 1, B)$ and α. This results in the field dependence

$$J_{\mathrm{c,v}}(f = 1, B) = \left(\frac{B}{0.1\ \mathrm{T}}\right)^{-0.36}. \tag{37}$$

Note, that when deriving Eq. (37), the normalization $J_{\mathrm{c,v}}(f = 1, B = 0.1) = 1$ was used. Thus, in order to evaluate the absolute values of $J_{\mathrm{c,v}}(f, B)$, one has to rescale Eq. (37) by multiplying it by the value of $J_{\mathrm{c,v}}(f = 1, B = 0.1)$. This is where the above chosen normalization becomes handy, since the field $B = 0.1\,\mathrm{T}$ corresponded to a situation, where only a single vortex was present within the simulation grid

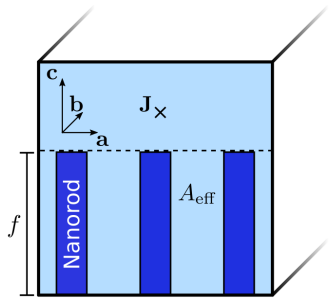

Figure 22. A schematic illustration of the effective superconducting cross-sectional area A_{eff} for the considered bilayer structure associated with f. Figure from **[V]**.

and the effect of vortex-vortex interaction was literally absent. Thus, the value of $J_{\mathrm{c,v}}(f = 1, B = 0.1)$ can be solved analytically as J for which the maximum pinning force equals to the Lorentz force resulting in

$$J_{\mathrm{c,v}}(f = 1, B = 0.1) = \frac{\Phi_0}{2\pi\mu\lambda^2} \cdot \frac{\xi\sqrt{2/3}R^2}{(2\xi^2/3 + 2\xi^2)^2}. \tag{38}$$

In the case of the BZO nanorods ($R = 3\,\mathrm{nm}$) in the low-temperature limit with $\lambda = 150\,\mathrm{nm}$ and the $\xi = 1.5\,\mathrm{nm}$ corresponding to the simulations, Eq. (38) yields $\sim 350\,\mathrm{MA/cm^2}$. Using this value to scale Eq. (37) and inserting it to Eq. (36), one obtains the final expression

$$J_{\mathrm{c,v}}(f, B) \approx 350\ \ \mathrm{MA/cm^2} \cdot \left(\frac{B}{0.1\ \ \mathrm{T}}\right)^{-0.36} \cdot f\,. \tag{39}$$

4.4.2 Zero field current

The simplest approach to model the evolution of $I_{\mathrm{c},0}$ as a function of f is to assume that the depairing current density (J_{dp}) is not affected by the inclusion of APCs within the superconducting lattice. Under this assumption, the experimentally observed degradation of $I_{\mathrm{c},0}$ simply results from the reduction of the effective superconducting cross-sectional area (A_{eff}) as the density of the APCs within the superconducting lattice is increased. The A_{eff} for the considered bilayer structure is illustrated in Figure 22, from which it becomes evident that the $A_{\mathrm{eff}} \propto f$. Since by definition $I_{\mathrm{c},0} = J_{\mathrm{dp}} \cdot A_{\mathrm{eff}}$, one concludes that the $I_{\mathrm{c},0}$ decreases linearly as a function of f.

In practice, one experimentally determines the J_{c} by measuring the critical current (I_{c}) and dividing it by the approximated total cross-sectional area of the current stripe neglecting the previously discussed effect of APCs. Thus, one automatically

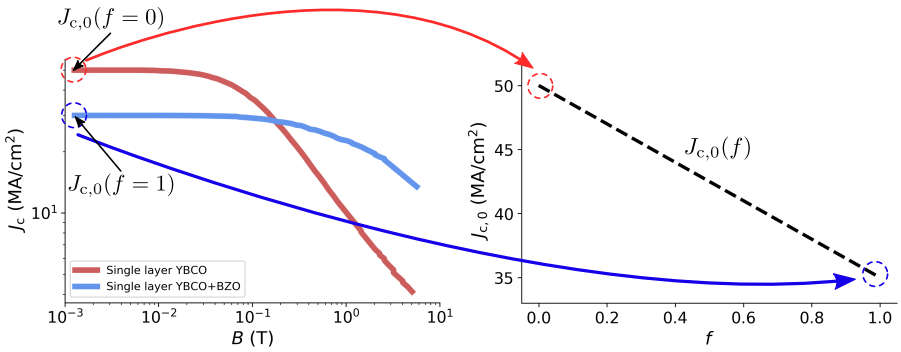

Figure 23. A schematic illustration of how to find numerical expression for the function $J_{c,0}(f)$. The numerical values of $J_{c,0}(f=0)$ and $J_{c,0}(f=1)$ can be determined from the experimentally measured $J_c(B)$ curves for intrinsic and BZO doped single layer films corresponding to the bilayer structure as illustrated in the figure. Assuming that $J_{c,0}(f)$ behaves linearly in the range $f \in [0,1]$, one can determine the associated slope as $\Delta Jc,0 = J_{c,0}(f=0) - J_{c,0}(f=1)$. Figure from **[V]**.

takes into account the reduced A_{eff} by the APCs and the above discussed I_c corresponds to the experimentally determined J_c in the above described way. This prompts one to write an empirical relation for the current density under zero field as

$$J_{c,0}(f) = J_{c,0}(f=0) - \Delta J_{c,0} \cdot f, \tag{40}$$

where $\Delta J_{c,0} = J_{c,0}(f=0) - J_{c,0}(f=1)$ represents the associated slope. The parameters $J_{c,0}(f=0)$ and $J_{c,0}(f=1)$ can be determined directly from e.g. magnetically measured $J_c(B)$ curves for the undoped and doped single layer films corresponding to the bilayer structure as illustrated in Figure 23. This has been done by using the previous studied **[III, VII]** suggesting that $J_{c,0}(f=0) \approx 50$ MA/cm^2 and $J_{c,0}(f=1) \approx 30$ MA/cm^2 resulting in

$$J_{c,0}(f) = 50 \ \text{MA/cm}^2 - 20 \ \text{MA/cm}^2 \cdot f\,. \tag{41}$$

It is evident that the underlying assumption about the constant J_{dp} is not completely valid as the inclusion of the APCs is known to also induce strain fields into the surrounding superconducting matrix and consequently lower the J_{dp} [15; 17]. However, the effects of crystalline structure on superconducting properties are extremely difficult, if not impossible, to model. Thus, the proposed assumption can be considered the only plausible way to quantitatively address the effects of APCs on $J_{c,0}$. Most importantly, the predictions of the proposed model coincide well with several experimental studies reporting a linear relationship between critical temperature or $J_{c,0}$ [56; 57; 59], **[III]**.

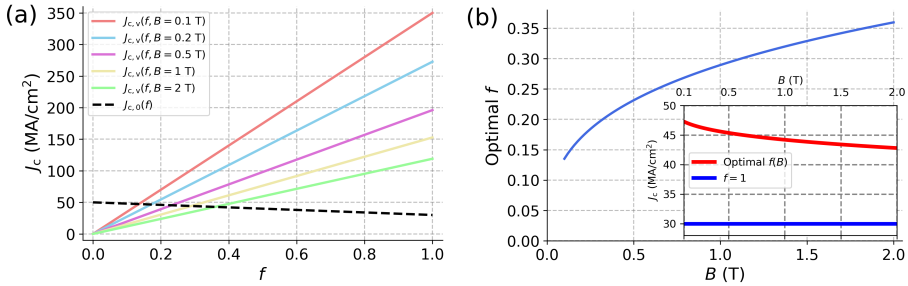

Figure 24. (a) Plots of the functions $J_{\mathrm{c,v}}(f, B)$ and $J_{\mathrm{c},0}(f)$ given by Eqs. (39) and (41) under various magnetic fields (b) Main: The optimal f as a function of the magnetic field obtained by solving the equation $J_{\mathrm{c,v}}(f, B) = J_{\mathrm{c},0}(f)$ for f. Inset: The J_{c} as a function of field for an optimized bilayer structure in the given field and for a fully doped single layer film. Figures from **[V]**.

4.4.3 Solving for optimal f

In the previous sections 4.4.1 and 4.4.2, numerical expressions for the functions $J_{\mathrm{c,v}}(f, B)$ and $J_{\mathrm{c},0}(f)$ have been derived, given by Eqs. (39) and (41), respectively. One is now able to estimate the optimal value of f for the proposed bilayer structure as the crossing point of the associated functions as explained in the beginning of this section. The functions $J_{\mathrm{c,v}}(f, B)$ and $J_{\mathrm{c},0}(f)$ are plotted in Figure 24(a) under various magnetic fields, suggesting that the optimal f for the proposed bilayer structure lies between 0.1–0.4 and increases as a function of the applied magnetic field. The evolution of optimal f as a function of field can be addressed more precisely by analytically solving the equation $J_{\mathrm{c,v}}(f, B) = J_{\mathrm{c},0}(f)$ for f. The resulting optimal f as a function of field is plotted in the main panel of Figure 24(b). The value of the optimal f more than doubles as the field is increased from 0.1 T to 2 T. However, even under 2 T field the optimal f is rather small, suggesting that the vast majority of the optimal bilayer structure should contain undoped YBCO. The inset of Figure 24(b) presents the resulting J_{c} of an optimal bilayer structure in a given field and the J_{c} of a fully doped single layer film as a function of magnetic field. According to the performed calculations, the optimized bilayer structures would have approximately 50% increased J_{c} over the fully doped single layer films at least up to 2 T field. However, the greatest benefit of the bilayer structures is seen under low magnetic fields as the difference between the associated J_{c}s decreases when the applied field is increased. It should be pointed out that the above presented results ideally apply to bilayer films of arbitrary thicknesses. This is because all of the associated forces scale according to the total thickness of the film. Consequently, only the relative thickness of the adjacent layer affect the overall J_{c} of the bilayer structure.

The obtained results are ultimately based on the theoretical evaluation of $J_{\mathrm{c,v}}(f = 1, B = 0.1, \ \mathrm{T})$ according to Eq. (38). However, this approach is susceptible to error

as Eq. (38) is lacking a solid empirical basis. Consequently, an extensive comparison to experimental data is required in order to comprehensively validate the presented results. Such experiments along with their implications are proposed and discussed in section 4.6.

4.5 Multilayer optimization using artificial intelligence

The main difficulty associated with broad-scale optimization of HTS ML films is the massive search space resulting from the wide range of plausible APC configurations within the practically limitless number of different ML structures. In addition, the optimal ML structure can be expected to be highly temperature and field dependent. Such broad-scale optimization problem is evidently to be addressed computationally, which needs to consider both $J_{\mathrm{c},0}$ and $J_{\mathrm{c,v}}$ as done in the previous section.

The evaluation of $J_{\mathrm{c,v}}$, in particular, requires a lot of computational effort. The most precise way to address this is to acquire numerical solutions of the Ginzburg-Landau equations as done in [116; 117; 118; 119; 120]. However, this approach takes tremendous computational effort thus making it unsuitable for the desired optimization purposes. So far, the upper-level models based on the MD method, such as the one presented in section 3.6.1, have proven to be the most efficient way to reliably simulate $J_{\mathrm{c,v}}$ within wide range of different pinning structures and environments [121; 122; 123; 124; 125; 29]. Yet still, the MD based models possess way too high computational cost to address the search space of the size associated with the broad-range ML optimization. In conclusion, the development of computationally lighter vortex pinning simulation models is a necessity for meticulous ML optimization.

The increasing prevalence of utilizing highly developed AI models (see section 3.6.3) in a broad range of science and technology provides new opportunities for the HTS community as well [126]. In particular, the AI models could be used together with vortex dynamics simulations to significantly reduce the number of computationally generated data required for the broad-scale optimization of the ML films. However, as the AI models need to be trained with a sufficient amount of data, their utility ultimately depends on the efficiency of evaluating $J_{\mathrm{c,v}}$.

In **[VI]**, the suitability of AI models to address the broad-scale optimization of HTS ML films has been studied. For this, a new vortex pinning simulation method enabling the efficient evaluation of $J_{\mathrm{c,v}}$ for complex pinning structures present in ML structures had to be proposed. This simulation model is then used to generate training data for the AI models, which are further to be used for predicting general properties of optimal ML structures in specific field and temperature ranges.

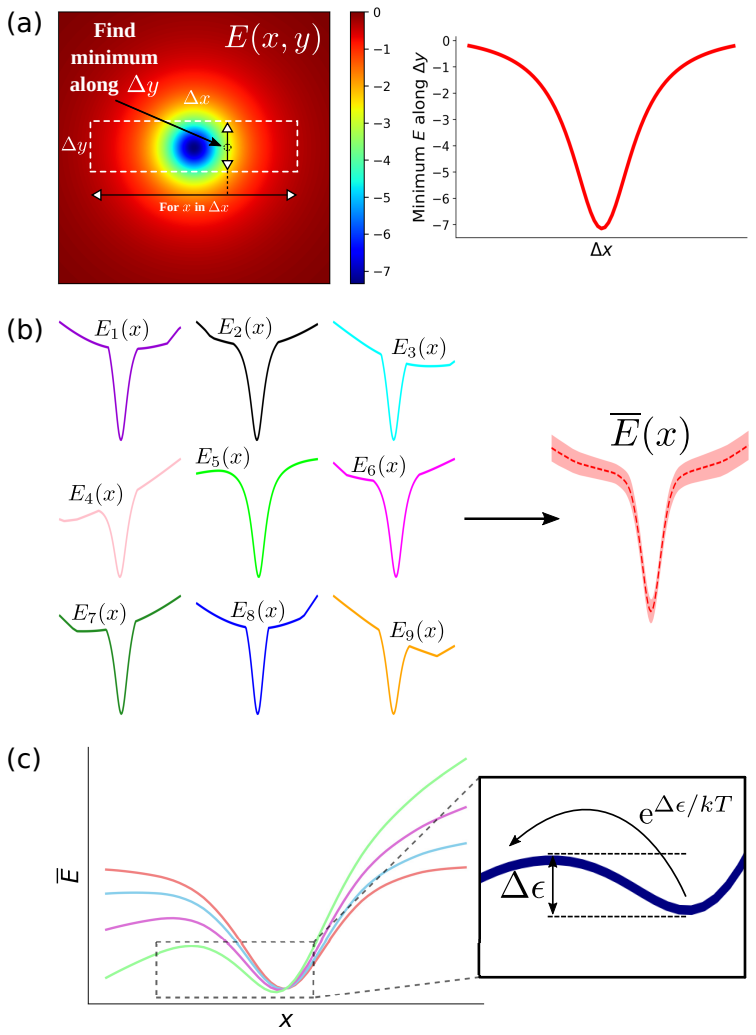

Figure 25. (a) A schematic illustration of how the individual pinning potentials of the vortices ($E_i(x)$) were calculated. (b) After the $E_i(x)$s have been calculated, one obtains the effective pinning potential ($\overline{E}_i(x)$) as the average of the $E_i(x)$s. (c) Determination of the $J_{\mathrm{c,v}}$ by applying linear potential ($\propto J$) to $\overline{E}_i(x)$ and checking when the vortex excitation probability $\exp(\Delta\epsilon/kT)$ exceeds a predetermined threshold value. Figures from **[VI]**.

4.5.1 Proposed simulation model

The proposed simulation model for $J_{\mathrm{c,v}}$, as it will be presented, is restricted for vortices oriented perpendicular to the surface of the film. In the case of YBCO, along with other HTS materials, this direction is along the c-axis (z-direction). The proposed model is based on calculating the vortex energy distribution along the ab-plane (xy-plane) of the HTS matrix. In the case of ML structures, the pinning landscapes of individual layers can be projected onto the ab-plane where the 2-dimensional potential energy distribution is to be calculated. In other words, the potential energy distributions of individual layers are simply summed together. Consequently, the order of the layer is completely arbitrary. In order to calculate this, one has to evaluate the pinning potential using the same equation as for the previous works (Eq. (10)), that is

$$E_{\mathrm{vp}}(\mathbf{r}) = -\frac{\epsilon_0}{2} \sum_{i=0}^{N_{\mathrm{ps}}} \frac{l_{z,i} R_i^2}{|\mathbf{r}_i - \mathbf{r}|^2 + 2\xi(T)^2}, \tag{42}$$

where the index i runs through a total of N_{ps} APCs within the ML structure projected on the ab-plane. Here, the size of the APC along the c-direction has to be taken explicitly into account by introducing a parameter $l_{z,i}$. In the case of nanorods, the $l_{z,i}$ evidently equals to the associated layer thickness. For spherically symmetric nanodots, on the other hand, the $l_{z,i}$ equals to the diameter of the associated defect.

One also has to consider the vortex-vortex interactions via the previously introduced Eq. (7). That is,

$$E_{\mathrm{vv}}(\mathbf{r}) = \sum_{i=0}^{N_{\mathrm{v}}} \epsilon_0 t_{\mathrm{f}} \begin{cases} \mathrm{K}_0\left(\frac{|\mathbf{r}_i - \mathbf{r}|}{\lambda(T)}\right), & \text{when } |\mathbf{r}_i - \mathbf{r}| > \xi \\ 2 \cdot \mathrm{K}_0\left(\frac{\xi(T)}{\lambda(T)}\right), & \text{when } |\mathbf{r}_i - \mathbf{r}| \leqslant \xi, \end{cases} \tag{43}$$

where the index i runs through a total of $N_{\mathrm{v}} = BA/\Phi_0$ c-axis oriented vortices, where A is the area of the ab-oriented simulation grid. In the case of vortices, the interaction energy has to be scaled by the total thickess of the film t_{f}, which in the case of ML structure is the sum of all individual layer thicknesses. Note, that the form of Eq. (43) allows the creation of giant vortex states, which are vortices associated with more than a single flux quantum.

The initial state of the system is created by placing the desired number of vortices one by one to the existent energy minimum of the grid. After this, the individual potential wells of the vortices along the x-direction ($E(x)$) are calculated. This is done by calculating the energies of a vortex along the x-direction in range $x \in [x_0 - \Delta x/2,\ \ x_0 + \Delta x/2]$. Each value of x was then associated with the energy minimum along the y-direction within the range $y \in [y_0 - \Delta y/2,\ \ y_0 + \Delta y/2]$, resulting in the pinning potential $E_i(x)$ for the ith vortex as illustrated in Fig. 25(a).

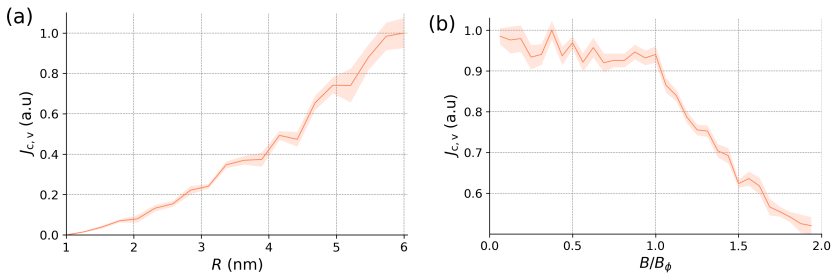

Figure 26. (a) The simulated $J_{c,v}$ associated with lattices of nanorods with varying radius. (b) The $J_{c,v}$ for a lattice of nanorods as a function of the associated matching field. Data for the figures is taken from **[VI]**.

Finally, one calculates the effective pinning potential ($\overline{E}(x)$) as an average of the previously determined individual $E_i(x)$s as illustrated in 25(b). The $\overline{E}(x)$ is then used to determine the $J_{c,v}$ by perturbing it with a linear potential

$$E(x, J) = \overline{E}(x) + Jx, \tag{44}$$

where J represents the applied current density along the y-direction. The $J_{c,v}$ is then determined as the J for which $\exp(-\Delta\epsilon/kT) > 10^{-2}$ using the bisection method, where the $\Delta\epsilon$ is the associated excitation energy illustrated in Fig. 25(c).

Validity

The validity of the above described simulation model has been tested by trying to reproduce the characteristic traits of vortex dynamics associated with the widely studied nanorod lattices. Firstly, a system of $N_{ps} = 25$ nanorods and $N_v = 5$ vortices at 10 K temperature confined within $X \times Y = 170 \times 170\,\text{nm}^2$ grid has been studied. The $E_i(x)$s were calculated using $\Delta x = X/2$ nm and $\Delta y = Y/\sqrt{N_{ps}}$ nm with a 0.2 nm accuracy. Fig. 26(a) presents the obtained $J_{c,v}$ as the radius of the associated nanorods was varied. The observed increase of $J_{c,v}$ as a function of R is in line with the observations presented in section 4.1.2.

Secondly, the evolution of $J_{c,v}$ as a function of the matching field $B_\phi = N_v/N_{ps}$ at 10 K temperature was studied. For this, a $150 \times 150\,\text{nm}^2$ sized grid with a total of 16 nanorods was used. Rest of the parameters were chosen similarly to the case described above. The results are presented in Fig. 26(b), where the $J_{c,v}$ can be observed to remain somewhat constant below B_ϕ but degrades vastly after the B_ϕ is exceeded. This is in line with the general understanding of vortex dynamics, as above the B_ϕ the vortices can only get weakly trapped within the superconducting matrix via natural defects and vortex-vortex interactions resulting in lower $J_{c,v}$.

Limitations

The computational performance of a model typically goes hand in hand with the associated physical accuracy. This is also the case for the presented model, which is build on some major simplifications. Thus, the flaws of the proposed model should be thoroughly discussed so that the associated limitations, depending on the situation, could be recognized.

In section 4.1.1 it was proposed that the $J_{\mathrm{c,v}}$ is proportional to the probability of a vortex encountering an APC, which is evidently proportional to the associated density. This is effectively taken into account in MD based models, where the vortices are set to dynamical initial state. However, this is completely neglected in the presented model which assumes a static initial state, where all of the vortices are set to the minimum energy positions. As both the dynamical and static pictures can be somewhat equally justified, the question whether one reflects the reality better than the other remains open.

Another issue to be pointed out is that the presented model does not take into account the elastic properties of the vortices [21; 127]. In favor of the proposed model, it is worth mentioning that the overall elasticity of the vortices under magnetic fields oriented parallel to the c-axis of YBCO is rather questionable due to the substantial line tension force discussed in section 3.6.1. However, this might be something that one should consider for particularly complex ML structures associated with high concentrations of APCs. On the other hand, based on the discussion in section 4.4, the high APC concentrations can be associated with increased flux creep which to some extent compensates used assumption of inelastic vortices.

4.5.2 Addressing the $J_{\mathrm{c},0}$

The degradation of $J_{\mathrm{c},0}$ as a function of dopant concentration is most easily addressed by the method introduced in section 4.4.2. That is, the seeming experimentally observed decrease of $J_{\mathrm{c},0}$ as a function of increasing APC concentration results from the reduced cross-sectional area for the supercurrent to pass through. As one only has to consider simple surface geometry, the evaluation of $J_{\mathrm{c},0}$ for any ML structure is easy and computationally efficient.

As the critical current density is experimentally determined as $J_{\mathrm{c}} = I_{\mathrm{c}}/A_{\mathrm{cross}}$, where the cross-sectional area A_{cross} is considered independent of APC morphology, it follows that the APC morphology dependence of the $J_{\mathrm{c},0}$ can be written as

$$J_{\mathrm{c},0}(\sigma) = J_{\mathrm{c},0}(\sigma = 0) \cdot (A_{\mathrm{cross}} - a(\sigma, R)) \,, \tag{45}$$

where σ represents the APC concentration in terms of volume percentage, $J_{\mathrm{c},0}(\sigma = 0)$ is the zero field current density associated with undoped single layer film and $a(\sigma, R)$ is a function that outputs the reduced cross-sectional area of the film. In the

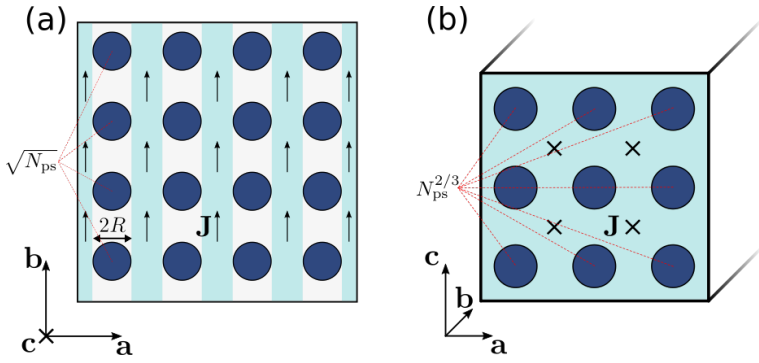

Figure 27. A schematic illustration of how to calculate the the reduced cross-sectional area due to (a) a 2-dimensional square lattice of nanorods along the ab-plane and (b) a 3-dimensional cubic lattice of nanodots.

case of nanorods that form a 2-dimensional square lattice within the ab-plane of the HTS matrix, the corresponding function can be written as

$$a(\sigma, R) = \sqrt{N_{\rm nr}} \cdot 2R, \tag{46}$$

where $N_{\rm nr}$ is the number of nanorods as easily deduced from the schematic illustration in Fig. 27(a). The $N_{\rm nr}$ can be further solved from the definition of σ for nanorods

$$\sigma = \frac{N_{\rm nr} \cdot \pi R^2}{A_{ab} - N_{\rm nr} \cdot \pi R^2}\,. \tag{47}$$

The parameter A_{ab} represents the surface area of the film along the ab-plane.

Correspondingly for nanodots, which are assumed to form a 3-dimensional cubic lattice, one can write

$$a(\sigma, R) = N_{\rm nd}^{2/3} \cdot \pi R^2, \tag{48}$$

where the number of nanodots $N_{\rm nd}$ as illustrated in Fig. 27(b). The $N_{\rm nd}$ can be solved from the definition of σ for nanodots

$$\sigma = \frac{N_{\rm nd} \cdot 4\pi R^3/3}{V_{\rm film} - N_{\rm nd} \cdot 4\pi R^3/3}, \tag{49}$$

where $V_{\rm film}$ represents the total volume of the film.

4.5.3 Dataset

The generated dataset consists of randomly sampled ML structures and their associated $J_{\rm c,v}$s and $J_{\rm c,0}$s evaluated by the above described methods. The total thickness

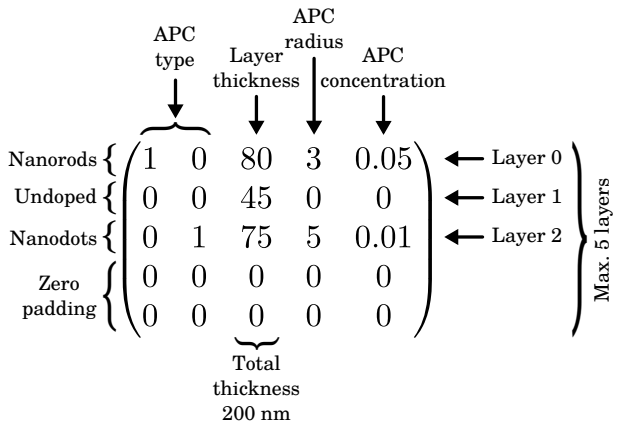

Figure 28. A schematic illustration of an descriptor used for the randomly sampled ML structures. Figure from **[VI]**.

of the ML film is arbitrary since the pinning potential of a nanorod is scaled according to the associated layer thickness while the strength of the vortex-vortex and the Lorentz interactions are determined by the total thickness of the film. Thus, the total thickness of the randomly generated ML film was simply chosen to be limited to 200 nm, while the total number of individual layers was chosen between 2–5. Each of the generated layers were then randomly chosen to be either undoped or doped. If the layer was chosen to be doped, the APC type, size and concentration were further randomized. The possible APC types included both nanorod and nanodots, while the associated choices for radii and concentrations are listed in Table 6. The length of the nanorod along the c-direction was determined by the associated layer thickness, while in the case of nanodots the length simply equals to the diameter of the nanodot. The generated ML structures were described using a 5×5 matrix schematically illustrated in Figure 28. Each row of the descriptor matrix represents an individual layer, while the columns encode information related to the layer thickness and the associated dopant concentrations. Zero padding was used to complete the matrix in the case of ML structures with less than five layers.

A total of 23,500 ML descriptors whose $J_{\mathrm{c},0}$ and $J_{\mathrm{c,v}}$ were evaluated at 10 K temperature under 1 T field with the methods described in sections 4.5.2 and 4.5.1

Table 6. The possible choices of parameters for the different APC-types.

APC-type	Radius (R)	Length along z-axis (l_z)	Concentrations (ρ)
Nanorod	1, 2,..., 6 nm	Layer thickness	0.01, 0.02,..., 0.12
Nanodot	3, 2,..., 6 nm	$2 \cdot R$	0.01, 0.02,..., 0.07

have been sampled. The comparison of the ML structures with each other naturally requires assigning a specific fitness value (F) for each descriptor based on the calculated $J_{\mathrm{c},0}$ and $J_{\mathrm{c,v}}$. Thus, one has to determine a fitness function according to which F is calculated. Following the outline used in the bilayer optimization discussed in section 4.4, the fitness function would be simply the smallest of the calculated $J_{\mathrm{c},0}$ and $J_{\mathrm{c,v}}$. However, this approach is not suited for desired broad-scale ML optimization since the fitness function is sensitive to the zero field values of the $J_{\mathrm{c},0}$ and $J_{\mathrm{c,v}}$ which are unknown. This problem can be circumvented by individually normalizing the calculated $J_{\mathrm{c},0}$s and $J_{\mathrm{c,v}}$s within the dataset. That is, the descriptor associated with highest zero field current has $J_{\mathrm{c},0} = 1$ and the one with highest vortex dynamics limited critical current has $J_{\mathrm{c,v}} = 1$. After the normalization the fitness of the descriptors is evaluated via equation

$$F = \alpha \cdot J_{\mathrm{c},0} + \beta \cdot J_{\mathrm{c,v}}, \tag{50}$$

where α and β serve as phenomenological constants that scale the importance of the $J_{\mathrm{c},0}$ and $J_{\mathrm{c,v}}$ under given environment. The phenomenological parameters need to be evaluated either with intuition, experimental data or both. For example, in the case of ML film operating under high-field range, one should evidently prioritize good vortex pinning properties by the maximization of $J_{\mathrm{c,v}}$ at the cost of $J_{\mathrm{c},0}$. Thus, one chooses $\alpha = 0$ and $\beta = 1$. On the contrary, under zero field a plausible choice would be $\alpha = 1$ and $\beta = 0$.

4.5.4 Comparison of AI models

The above described dataset was then divided into training and testing sets of size 20,000 and 3500, respectively. In order to find the generally best suitable model for the associated task, the model was trained using descriptors evaluated by a fitness function with $\alpha = 1$ and $\beta = 1$. A total of three different types of supervised AI models were compared with each other. These models included kernel rigde regression (KRR), gradient-boosted decision trees (GBDT) and neural networks (NN), which are respectively associated with increasing complexity. The used KRR and NN (multilayer perceptron) models were provided by the Scikit-learn library, while for the GBDT a library provided by XGBoost was utilized.

Significant effort has been put in optimizing the HPs of the studied models. The simplest AI model within the corresponding work is the KRR, the hyperparameters of which were optimized using a simple brute-force method (grid search). The resulting performance of the KRR could be thus reliably maximized. However, the KRR by default is not as good in predicting complex relations for unseen data when compared with more complex models such as GBDT or NN. While the GBDTs and NNs can potentially acquire very high prediction accuracy even for very complex data, their maximum capacity is hard to achieve due to extensive number of HPs to be optimized

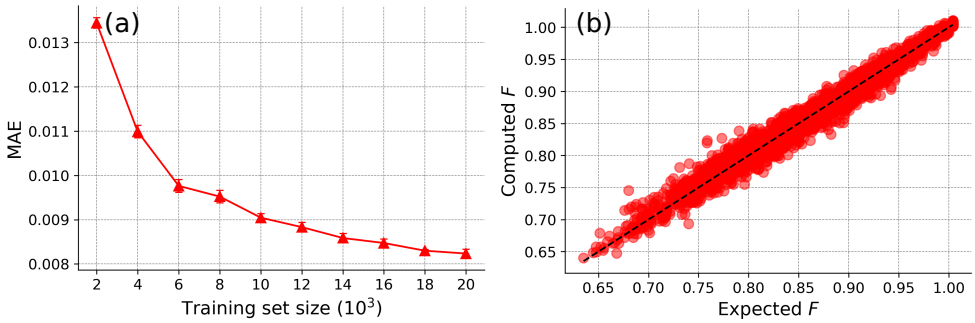

Figure 29. (a) The mean absolute error of prediction for GBDT as a function of training set size (learning curve). The model was trained using the fitness function $F = 1 \cdot J_{\mathrm{c},0} + 0.1 \cdot J_{\mathrm{c,v}}$ to rank the descriptors. (b) The associated regression plot of GBDT trained with set of 20,000 data points. Data for the figures is taken from **[VI]**.

with respect to each other. Consequently, the number of HPs to be optimized was tried to be limited by identifying the most significant HPs through comprehensive understanding of the models, intuition and manual testing. Only the HPs that were concluded to have the greatest effect in terms of models learning efficiency were further rigorously optimized, while the rest of the HPs were kept at fixed values. In the case of GBDT, the chosen HPs were optimized using stochastic Bayesian optimization that is considered as effective and computationally cheap method.

After comprehensive HP optimization, the GBDT was determined to be the best performing model both in terms of prediction accuracy and computational efficiency. Consequently, it was chosen to be used to predict the general properties of the optimal ML structures at 10 K temperature under 1 T field corresponding to the generated dataset. In order to do this, the parameters α and β of the fitness function need to be evaluated. Here, the outline presented in section 4.4 was followed, where the $J_{\mathrm{c},0}$ was estimated to be ~ 10 times lower when compared with $J_{\mathrm{c,v}}$ under corresponding environment. Thus, the significance of $J_{\mathrm{c},0}$ and $J_{\mathrm{c,v}}$ within the fitness function was balanced by choosing $\alpha = 1$ and $\beta = 0.1$. Figure 29(a) presents the resulting prediction accuracy in terms of mean absolute error (MAE) of the GBDT trained with different dataset sizes (learning curve). The model gets exponentially more accurate as the training set size is increased ultimately leveling off around size of 20,000. For this, training set size, the accuracy of the model is definitely sufficient to be used for studying the properties of the optimal ML structures. The regression plot associated with the training set of size 20,000 is presented in Figure 29(b), which visualized the accuracy of the predictions using the assigned testing set. The prediction accuracy of the GBDT is adequate over the whole range of F as seen by the close proximity of the computed data points to the dashed line of Figure 29(b).

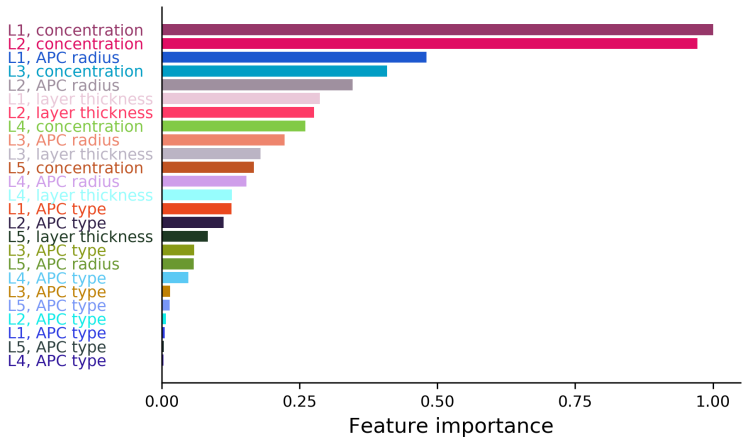

Figure 30. The results of the feature importance analysis. The L# labeling is used to indicate the associated layer. Figure from **[VI]**.

4.5.5 AI predicted optimal ML structures

Here, the previously described GBDT model will be utilized. To recap, the GBDT was trained with the dataset of size 20,000 evaluated at 10 K temperature and under 1 T field using the $F = 1 \cdot J_{c,0} + 0.1 \cdot J_{c,v}$ as a fitness function. An obvious choice for starting the investigation of optimal ML structure is to study the feature importances of the descriptor attributes. This was done by utilizing the built-in function of the XGBoost library. The results are presented in Figure 30, where the attributes associated with the first and second layers of the ML structure have significantly increased importance over further layers. The concentration and radius of the APCs associated with the first and second layers, in particular, turned out to have a great effect on the resulting fitness score. Since the order of the layers is completely arbitrary, the fact that the attributes of the first and the second layer, in particular, have substantially increased feature importances hints that simple bilayer structures would generally have better fitness scores when compared with more complex ML structures. Consequently, one progresses to study how exactly the number of layers within the ML structure affects the fitness score.

In order to study the effect of number of layers, a total of 5000 descriptors unseen by the trained GBDT have been randomly sampled. The pretrained GBDT was then used to predict the fitness of the associated structures. The average predicted F and the associated standard errors were then calculated as a function of number of layers. The results are presented in Figure 31(a), where the average fitness score can be observed to decrease as the number of layers in increased. This suggest that the optimal ML structure would be a simple bilayer film coinciding with the previously made conclusions in section 4.4. As a consequence, the properties of

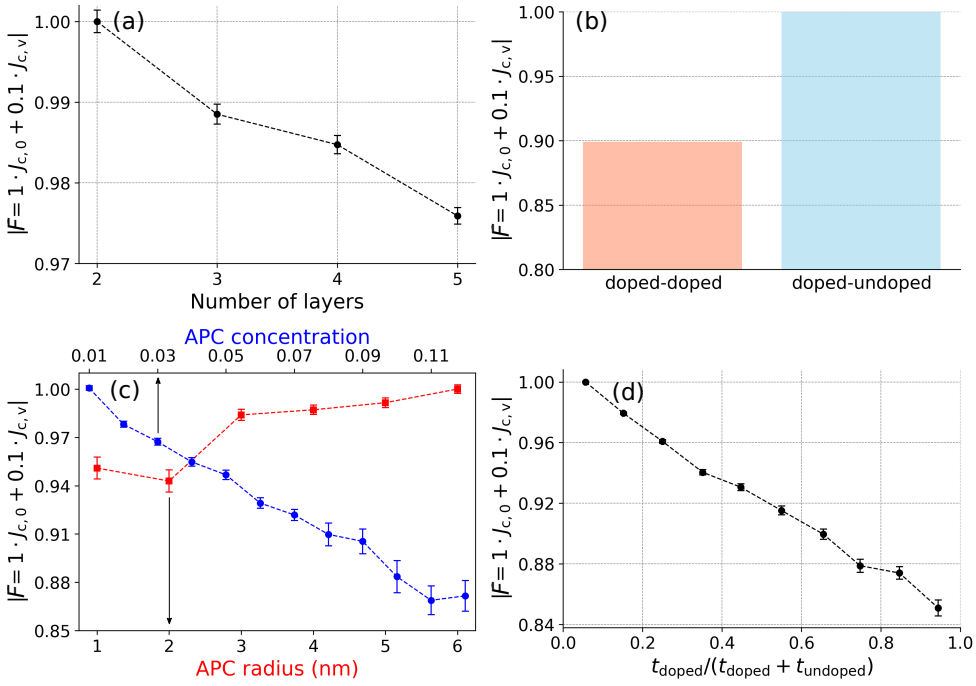

Figure 31. The GBDT predicted average (normalized) fitness values for a total of 5000 randomly generated (a) descriptors associated with different number of layers, (b) bilayer structures that consist either of two adjacent arbitrarily doped layers (doped-doped) or a single undoped layer adjacent to an arbitrarily doped layer (doped-undoped), (c) doped-undoped bilayer structures as a function of APC radius and concentration within the doped layer, (d) doped-undoped bilayer structures as a function of thickness fraction of the doped layer, explicitly defined as $t_{\mathrm{doped}}/(t_{\mathrm{doped}} + t_{\mathrm{undoped}})$, where t_{undoped} and t_{doped} are the thicknesses of the undoped and doped layers, respectively. The presented error bars correspond to the associated standard error of the mean. Data for the figures is taken from **[VI]**.

bilayer structures were further studied.

In order to get better comparison with the arguments related to the bilayer structures provided in section 4.4, a total of 5000 bilayer structures were randomly sampled for which the average predicted fitness scores among structures with both of the layers being doped (doped-doped) and only one of the layers being doped (doped-undoped) were calculated. The results visualized in Figure 31(b) reveal a significant 10% difference in the average fitness scores in favor for the doped-undoped bilayer films. This result, in particular, provides further justification for the arguments and results presented in section 4.4. Vice versa, the previous results further validate the current approach for finding the optimal ML structure.

Next, the effect of APC radius and concentration on the fitness score of the doped-undoped bilayer structure were independently studied. This was again done

by randomly sampling 5000 doped-undoped bilayer structures and calculating the average predicted fitness scores as a function of APC concentration and radius. The results are presented in Figure 31(c), where one can observe that increasing the radius of the APC also increases the fitness of the bilayer. This suggests that increasing the APC radius increases the pinning properties remarkably without significantly reducing the superconducting cross-sectional area of the film. Thus, ideally one should strive to use APCs with large radii. On the contrary, increasing the APC concentration is observed to decrease the associated fitness. This results from the vast reduction of the superconducting cross-sectional area, and thus $J_{\mathrm{c},0}$, as APC concentration is increased. As discussed in section 4.5.1, increasing the dopant concentration does not have significant effect on $J_{\mathrm{c,v}}$ under a field range for which $B < B_{\phi}$. As this is the case for the majority of the generated bilayers, the observed result evidently follows.

Finally, the relative thickness dependence of the predicted fitness scores within the doped-undoped bilayer structures were studied. In particular, one strives to express the GBDT predicted average fitness as a function of the relative thickness of the doped layer with respect to the whole film. That is, to calculate $t_{\mathrm{doped}}/(t_{\mathrm{doped}} + t_{\mathrm{undoped}})$, where t_{doped} and t_{undoped} are the thicknesses of the doped and undoped layers of the bilayer film, respectively. Note, that this quantity is the same the parameter f that was used in section 4.4, allowing us to further compare the obtained results. The results are presented in Figure 31(d), where the fitness of the doped-undoped bilayer structures is observed to linearly increase with decreasing relative thickness of the doped layer. Again, the obtained result coincides with the results of section 4.4, where the vast majority of an optimal doped-undoped bilayer film was concluded to consist of the undoped layer.

The good correspondence between the results presented here and section 4.4 further validate the presented approach to address the broad-scale optimization of ML structures. Similarly with the results regarding the optimal bilayer structure in section 4.4, the conclusion of this chapter ideally apply to films of arbitrary thicknesses. It can be concluded, that the use of AI models for the associated task provides a great benefit both in terms of computational cost along with diverse and rigorous possibilities for detailed analysis. However, it should be pointed out that the obtained results ultimately depend on the choice of the parameter α and β within the fitness function. These parameters were evaluated based on the approach presented in section 4.4, where the $J_{\mathrm{c},0}$ and $J_{\mathrm{c,v}}$ of undoped and doped single layer films were evaluated using experimental data and theoretical pinning model, respectively. As already concluded in section 4.4, the evaluation of the absolute value for the $J_{\mathrm{c,v}}$, in particular, is prone to error as the used equation (Eq. (38)) is lacking empirical basis. The reliable comparison to experimental results and the consequent implications are discussed in section 4.6.

4.6 Proposals for future experiments

The mutual agreement of the results presented in sections 4.4 and 4.5 suggest that simplistic pinning structures, such as the doped-undoped bilayer structures, would have increased critical current densities when compared with any other ML solution at low-temperature under mid-field range. The characteristic trait of such an optimal bilayer structure would be small thickness of the doped layer with respect to the total thickness of the film, as represented by the parameter f in the section 4.4. The greatest uncertainty on the validity of the presented results comes from the theoretical evaluation of the pinning energy. Due to the lack of empirical basis, validation of the proposed results with respect to experimental observations is required.

Unfortunately there exists very limited amount of studies against which these conclusions could be reliably validated. Comprehensive studies regarding internal comparison of different ML and corresponding single layer structures with each other under wide temperature and field ranges are nonexistent. Moreover, this type of comparison would be further aggravated by the complex deposition process induced deviations in crystalline structures between the ML and single layer films as discussed in section 4.3. Thus, the reliable validation of the proposed optimal ML structure cannot be done using the existing literature.

Consequently, an experiment that can soundly be used to validate the obtained results is proposed. Firstly, the validation of the proposed optimal thickness ratio ($f \approx 0.3$) of the bilayer structure in section 4.4 will be addressed. For this, a set of 11 films illustrated in Figure 32(a) should be deposited. These include bilayer structures associated with $f = 0.1, 0.2, ..., 1$ along with the corresponding single layer films for which $f = 0$ and $f = 1$. The type of nanorod and the associated density within the doped layer is arbitrary as long as measurements are carried out under $B < B_\phi$. Attention should be put in choosing the order of the layers to be deposited. There is strong experimental evidence that BZO nanorods would grow coherently on top of pre-deposited YBCO layer [34]. Under this assumption, the undoped layer should be always deposited first in order to maximize the associated crystalline quality and the resulting superconducting properties. In order to circumvent the ML deposition related deviations in the crystalline structure of the resulting films, the single layer film corresponding to $f = 0$ and $f = 1$ should be deposited in two intervals between which similar amount of time is passed as for the deposition of the actual bilayer structures.

Conducting magnetic measurements for the previously described set of samples reveals the J_c as a function of f determining the optimal f as schematically illustrated in Figure 32(b). Such a graph should be experimentally measured in order to have a reliable comparison between the proposed results of section 4.4. In the case of discrepancies as illustrated in 32(b), one would be able to empirically re-evaluate the numerical value of the pinning potential corresponding to the associated nanorods

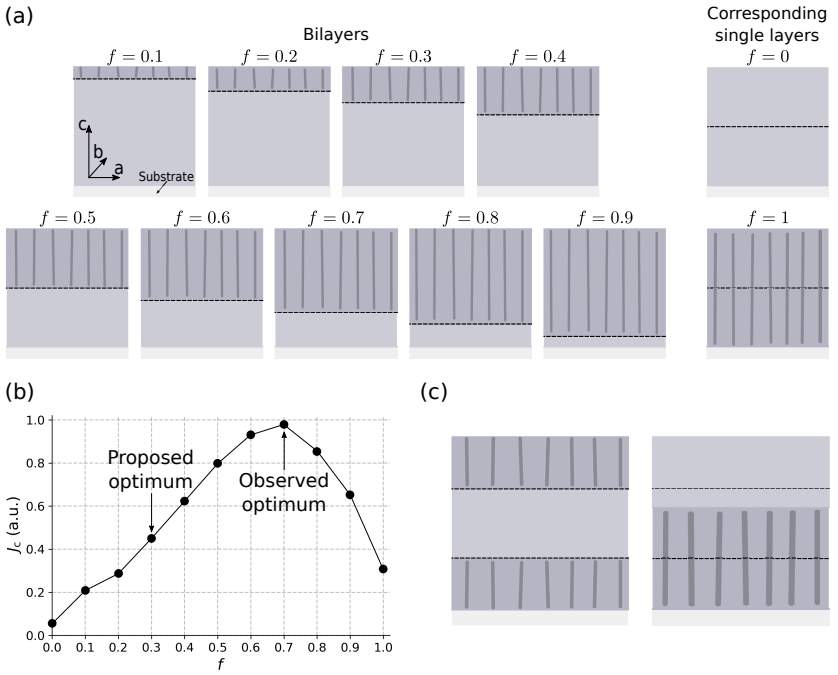

Figure 32. (a) The proposed films to be deposited consisting of adjacent layers of undoped and doped YBCO. (b) An example of a possible experimentally measured critical current densities as a function of f for the previously described set of films. The associated data is fabricated and does not reflect any computational or experimental results. (c) A trilayer and bilayer structure corresponding to the experimentally determined optimal f. The black dashed lines illustrate the intervals of the deposition process.

using the formulas presented is section 4.4.

Another experiment of interest would be to compare the J_c of the previously determined optimal bilayer with corresponding trilayer illustrated in Figure 32(c). In order to achieve a reliable comparison, the bilayer would also have to be deposited in three intervals so that the effects of ML deposition on the crystalline structure would be equally prominent. This obtained result could be used to further validate the proposals of section 4.5, where it was argued that simplistic ML structures, in particular bilayers, would be associated with increased J_c under the specified field and temperature ranges. Here, the possible discrepancies would hint towards incorrect assumptions underlying in the proposed simulation model presented in section 4.5.2, including the assumed staticity and inelasticity the vortices.

5 Conclusions

The mechanisms and implications of vortex pinning within HTS thin films have been comprehensively studied. The use of both experimental and computational techniques has enabled one to obtain a general picture of pinning mechanisms associated with given APC morphologies, in particular for nanorods, under specified ranges of magnetic field magnitudes and orientations. The recognition of different pinning mechanisms, such as partial and multicolumn pinning, and knowing how to associate them with the discussed pinning related probabilities under a given magnetic environment is crucial for efficient tailoring of new generation HTS films for specific applications.

The magnetic field tolerance of a HTS film is mainly governed by the density of the APC lattice which is fortunately also the most easily tunable parameter associated with APC morphology. It was found that there exists a critical limit for the density of the nanorod lattice within the HTS matrix above which the vortex pinning performance of the film cannot be improved. This limit is reached when the average separation between the nanorods equals their associated diameter. In conclusion, the achievable matching field is fundamentally limited. However, the limit for the matching field is significantly higher than what is required for any plausible practical application of HTS films.

Striving to increase the current carrying properties of the HTS films via applying ML structures is an evident continuation after acquiring general knowledge about the vortex pinning mechanisms and the resulting fundamental limits. This is of particular interest since many previous studies have already reported improved superconducting properties for the studied ML films proposed without any systematic motivation. Moreover, whether the observed improvements result from the APC morphology itself or from some other aspect of the deposition process has not been comprehensively discussed. Such a study has been repeated by proposing a ML film consisting of alternating layers of 4% and 12% BZO doped YBCO that was considered to be a good candidate for achieving improved critical current under high field range **[II]**. By varying the associated layer thicknesses and comparing the experimentally measured critical currents with the simulations, it was concluded that in this case the observed improvement cannot result from the APC morphology and thus has to be due to modified crystalline structure during the deposition process. This further motivates the use of computational methods for searching optimal ML structures as they allow the

study of APC morphology, independent from the deposition process.

As a consequence, the developed MD based vortex dynamics simulation has been used for rigorous optimization of layer thicknesses associated with a bilayer structure consisting of adjacent layers of pure and BZO doped YBCO. Such bilayer films are of particular interest since they are generally the simplest possible ML structures both in terms of modeling and experimental realization. Based on the performed calculations, the relative thickness of the doped layer for the optimal bilayer structure under the mid-field range is around 30% of the total film thickness. For such a bilayer film, the overall critical current can be increased up to 50% when compared with the corresponding single layer structures. The obtained results are ultimately based on theoretical evaluation of the absolute value of the pinning force experienced by a vortex. In the lack of existing experimental literature considering such bilayer structures, an experiment that can be reliably used to validate the presented results has been proposed. In the case of discrepancies between the proposed theoretical results and experiments,one would be able to calculate an empirical estimation of the pinning energy associated with the nanorods in question.

Finally, the possibility to utilize the AI models for broad-scale ML structure optimization considering both nanodots and nanorods associated with a wide range of diameters and concentrations along with layer thicknesses has been studied. For this, a new simulation method that can be used to evaluate the vortex-dynamics-limited critical current with minimal computational cost has been proposed. The simulation is used for efficient generation of training data for the studied AI models that are intended to learn how to associate a given ML structure with a specified fitness value in a generalized manner. The performance of a total of three different types of AI models including kernel ridge regression, gradient-boosted decision trees and neural networks has been studied. The gradient-boosted decision trees were observed to perform best considering the accuracy of the predictions and the computational cost associated with the training of the model. The benefits for the use of the AI models have been demonstrated by studying the general properties of the ML structures associated with the highest predicted fitness scores by the trained AI model. The obtained results coincided well with the previous study considering the bilayer film optimization further validating the presented approach for the broad-scale optimization of the ML structures. The utilization of AI models was concluded to provide great opportunities for the community involved with the HTS materials.

List of References

[1] J. G. Bednorz and K. A. Müller. Possible high T_c superconductivity in the Ba-La-Cu-O system. *Zeitschrift für Physik B Condensed Matter*, 64(2):189–193, 1986.

[2] C. P. Poole, Farach H. A., Creswick R. J., and Prozorov R. *Superconductivity, 2nd edition*. Elsevier, 2009.

[3] J. L. MacManus-Driscoll and S. C. Wimbush. Processing and application of high-temperature superconducting coated conductors. *Nature Reviews Materials*, 6(7):587–604, 2021.

[4] J. Zhang, H. Wu, G. Zhao, L. Han, and J. Zhang. Progress in the study of vortex pinning centers in high-temperature superconducting films. *Nanomaterials*, 12(22):4000, 2022.

[5] K. Tsuchiya, X. Wang, S. Fujita, A. Ichinose, K. Yamada, A. Terashima, and A. Kikuchi. Superconducting properties of commercial REBCO-coated conductors with artificial pinning centers. *Superconductor Science and Technology*, 34(10):105005, 2021.

[6] T. J. Haugan and T. Puig. Artificial pinning centers in (Y, RE)-Ba-Cu-O superconductors: recent progress and future perspective. *Superconductor Science and Technology*, 33, 2019.

[7] S. R. Foltyn, L. Civale, J. L. MacManus-Driscoll, Q. X. Jia, B. Maiorov, H. Wang, and M. Maley. Materials science challenges for high-temperature superconducting wire. In *Materials For Sustainable Energy: A Collection of Peer-Reviewed Research and Review Articles from Nature Publishing Group*, pages 299–310. World Scientific, 2011.

[8] A. Goyal, S. Kang, K. J. Leonard, P. M. Martin, A. A. Gapud, M. Varela, M. Paranthaman, A. O. Ijaduola, E. D. Specht, J. R Thompson, D. K. Christen, S. J. Pennycook, and F. A. List. Irradiation-free, columnar defects comprised of self-assembled nanodots and nanorods resulting in strongly enhanced flux-pinning in $YBa_2Cu_3O_{7-\delta}$ films. *Superconductor Science and Technology*, 18(11):1533, 2005.

[9] B. Maiorov, S. A. Baily, H. Zhou, O. Ugurlu, J. A. Kennison, P. C. Dowden, T. G. Holesinger, S. R. Foltyn, and L. Civale. Synergetic combination of different types of defect to optimize pinning landscape using $BaZrO_3$-doped $YBa_2Cu_3O_7$. *Nature materials*, 8(5):398–404, 2009.

[10] J. L. MacManus-Driscoll, S. R. Foltyn, Q. X. Jia, H. Wang, A. Serquis, L. Civale, B. Maiorov, M. E. Hawley, M. P. Maley, and D. E. Peterson. Strongly enhanced current densities in superconducting coated conductors of $YBa_2Cu_3O_{7-x}$+ $BaZrO_3$. *Nature Materials*, 3(7):439–443, 2004.

[11] W. H. Fietz, R. Heller, S. I. Schlachter, and W. Goldacker. Application of high temperature superconductors for fusion. *Fusion Engineering and Design*, 86(6):1365–1368, 2011. ISSN 0920-3796. Proceedings of the 26th Symposium of Fusion Technology (SOFT-26).

[12] P. Bruzzone, W. H. Fietz, J. V. Minervini, M. Novikov, N. Yanagi, Y. Zhai, and J. Zheng. High temperature superconductors for fusion magnets. *Nuclear Fusion*, 58(10):103001, 2018.

[13] S. M. Anlage. Microwave superconductivity. *IEEE Journal of Microwaves*, 1(1):389–402, 2021.

[14] J. Golm, S. Arguedas Cuendis, S. Calatroni, C. Cogollos, B. Döbrich, J.D. Gallego, J.M. García Barceló, X. Granados, J. Gutierrez, I.G. Irastorza, T. Koettig, N. Lamas, J. Liberadzka-Porret, C. Malbrunot, W.L. Millar, P. Navarro, C.P.A. Carlos, T. Puig, G.J. Rosaz, M. Siodlaczek, G. Telles, and W. Wuensch. Thin film (high temperature) superconducting radiofrequency cavities for the search of axion dark matter. *IEEE Transactions on Applied Superconductivity*, 32(4): 1–5, 2022.

[15] J. Z. Wu, J. J Shi, J. F. Baca, R. Emergo, T. J. Haugan, B. Maiorov, and T Holesinger. The effect of lattice strain on the diameter of $BaZrO_3$ nanorods in epitaxial $YBa_2Cu_3O_{7-\delta}$ films. *Superconductor Science and Technology*, 27(4):044010, 2014.

[16] J. Z. Wu, J. J. Shi, F. J. Baca, R. Emergo, J. Wilt, and T. J. Haugan. Controlling $BaZrO_3$ nanostructure orientation in YBa_2Cu_3O films for a three-dimensional pinning landscape. *Superconductor Science and Technology*, 28(12):125009, 2015.

[17] J. Wu and J. Shi. Interactive modeling-synthesis-characterization approach towards controllable in situ self-assembly of artificial pinning centers in RE-123 films. *Superconductor Science and Technology*, 30(10):103002, 2017.

[18] M. Tachiki and S. Takahashi. Strong vortex pinning intrinsic in high-T_c oxide superconductors. *Solid State Communications*, 70(3):291–295, 1989.

[19] M. Tachiki and S. Takahashi. Anisotropy of critical current in layered oxide superconductors. *Solid State Communications*, 72(11):1083–1086, 1989.

[20] G. Blatter, V. B. Geshkenbein, and A. I. Larkin. From isotropic to anisotropic superconductors: A scaling approach. *Physical Review Letters*, 68(6):875, 1992.

[21] G. Blatter, M. V. Feigel'man, V. B. Geshkenbein, A. I. Larkin, and V. M. Vinokur. Vortices in high-temperature superconductors. *Reviews of Modern Physics*, 66:1125–1388, 1994.

[22] N. J. Long, N. M. Strickland, and E. F. Talantsev. Modeling of vortex paths in HTS. *IEEE Transactions on Applied Superconductivity*, 17(2):3684–3687, 2007.

[23] M. Buchacek, R. Willa, V. B. Geshkenbein, and G. Blatter. Strong pinning theory of thermal vortex creep in type-II superconductors. *Physical Review B*, 100(1):014501, 2019.

[24] L. Civale, B. Maiorov, A. Serquis, J. O. Willis, J. Y. Coulter, H. Wang, Q. X. Jia, P. N. Arendt, J. L. MacManus-Driscoll, M. P. Maley, and S. R. Foltyn. Angular-dependent vortex pinning mechanisms in $YBa_2Cu_3O_7$ coated conductors and thin films. *Applied Physics Letters*, 84(12): 2121–2123, 2004.

[25] L. Civale, B. Maiorov, A. Serquis, J. O. Willis, J. Y. Coulter, H. Wang, Q. X. Jia, P. N. Arendt, M. Jaime, J. L. MacManus-Driscoll, M. P. Maley, and M. P. Foltyn. Understanding high critical currents in $YBa_2Cu_3O_7$ thin films and coated conductors. *Journal of Low Temperature Physics*, 135:87–98, 2004.

[26] P. Paturi. The vortex path model and angular dependence of J_c in thin YBCO films deposited from undoped and $BaZrO_3$-doped targets. *Superconductor Science and Technology*, 23(2): 025030, 2010.

[27] L. Civale, B. Maiorov, J. L. MacManus-Driscoll, H. Wang, T. G. Holesinger, S. R. Foltyn, A. Serquis, and P. N. Arendt. Identification of intrinsic ab-plane pinning in $YBa_2Cu_3O_7$ thin films and coated conductors. *IEEE Transactions on Applied Superconductivity*, 15(2):2808–2811, 2005.

[28] T. Puig, J. Gutiérrez, A. Pomar, A. Llordés, J. Gazquez, S. Ricart, F. Sandiumenge, and X. Obradors. Vortex pinning in chemical solution nanostructured YBCO films. *Superconductor Science and Technology*, 21(3):034008, 2008.

[29] P. Paturi, M. Malmivirta, T. Hynninen, and H. Huhtinen. Angle dependent molecular dynamics simulation of flux pinning in ybco superconductors with artificial pinning sites. *Journal of Physics: Condensed Matter*, 30(31):315902, 2018.

[30] A. Ichinose, K. Naoe, T. Horide, K. Matsumoto, R. Kita, M. Mukaida, Y. Yoshida, and S. Horii. Microstructures and critical current densities of YBCO films containing structure-controlled $BaZrO_3$ nanorods. *Superconductor Science and Technology*, 20(12):1144, 2007.

[31] A. Kiessling, J. Hänisch, T. Thersleff, E. Reich, M. Weigand, R. Hühne, M. Sparing, B. Holzapfel, J. H. Durrell, and L. Schultz. Nanocolumns in $YBa_2Cu_3O_{7-x}$/$BaZrO_3$ quasi-multilayers: formation and influence on superconducting properties. *Superconductor Science and Technology*, 24(5):055018, 2011.

[32] K. Matsumoto, I. Tanaka, T. Horide, P. Mele, Y. Yoshida, and S. Awaji. Irreversibility fields and critical current densities in strongly pinned $YBa_2Cu_3O_{7-x}$ films with $BaSnO_3$ nanorods: The influence of segmented $BaSnO_3$ nanorods. *Journal of Applied Physics*, 116(16):163903, 2014.

[33] T. Horide, N. Sakamoto, A. Ichinose, K. Otsubo, T. Kitamura, and K. Matsumoto. Hybrid artificial pinning centers of elongated-nanorods and segmented-nanorods in $YBa_2Cu_3O_7$ films. *Superconductor Science and Technology*, 29(10):105010, 2016.

[34] M. Malmivirta, H. Rijckaert, V. Paasonen, H. Huhtinen, T. Hynninen, R. Jha, V. S. Awana, I. Van Driessche, and P. Paturi. Enhanced flux pinning in YBCO multilayer films with BCO nanodots and segmented BZO nanorods. *Scientific Reports*, 7(1):1–8, 2017.

[35] J. L. Smith, J. S. Brooks, C. M. Fowler, B. L. Freeman, J. D. Goettee, W. L. Hults, J. C. King, P. M. Mankiewich, E. I. De Obaldia, M. L. O'Malley, et al. Low-temperature critical field of YBCO. *Journal of Superconductivity*, 7(2):269–270, 1994.

[36] M. Cyrot. Ginzburg-Landau theory for superconductors. *Reports on Progress in Physics*, 36(2): 103, 1973.

[37] T. P. Orlando and K. A. Delin. *Foundations of applied superconductivity*. Addison-Wesley Publishing Company, Inc., 1991.

[38] O. M. Auslaender, L. Luan, E. W. J. Straver, J. E. Hoffman, N. C. Koshnick, E. Zeldov, D. A. Bonn, R. Liang, W. N. Hardy, and K. A. Moler. Mechanics of individual isolated vortices in a cuprate superconductor. *Nature Physics*, 5(1):35–39, 2009.

[39] E. H. Brandt. Elastic and plastic properties of the flux-line lattice in type-II superconductors. *Physical Review B*, 34:6514–6517, 1986.

[40] F. C. Klaassen, G. Doornbos, J. M. Huijbregtse, R. C. F. Van der Geest, B. Dam, and R. Griessen. Vortex pinning by natural linear defects in thin films of $YBa_2Cu_3O_{7-\delta}$. *Physical Review B*, 64 (18):184523, 2001.

[41] N-C Yeh. Vortex phases and dissipation in high-temperature superconducting oxides. *Physical Review B*, 40(7):4566, 1989.

[42] D. R. Nelson and V. M. Vinokur. Boson localization and correlated pinning of superconducting vortex arrays. *Physical Review B*, 48(17):13060, 1993.

[43] K. Momma and F. Izumi. Vesta 3 for three-dimensional visualization of crystal, volumetric and morphology data. *Journal of Applied Crystallography*, 44(6):1272–1276, 2011.

[44] M. A. Beno, L. Soderholm, D. W. Capone, D. G. Hinks, J. D. Jorgensen, J. D. Grace, I. K. Schuller, C. U. Segre, and K. Zhang. Structure of the single-phase high-temperature superconductor $YBa_2Cu_3O_{7-\delta}$. *Applied Physics Letters*, 51(1):57–59, 1987.

[45] J. D. Jorgensen, B. W. Veal, A. P. Paulikas, L. J. Nowicki, G. W. Crabtree, H. Claus, and W. K. Kwok. Structural properties of oxygen-deficient $YBa_2Cu_3O_{7-\delta}$. *Physical Review B*, 41(4): 1863, 1990.

[46] R. Liang, D. A. Bonn, and W. N. Hardy. Evaluation of CuO_2 plane hole doping in $YBa_2Cu_3O_{6+x}$ single crystals. *Physical Review B*, 73(18):180505, 2006.

[47] J. M. Huijbregtse, F. C. Klaassen, A. Szepielow, J. H. Rector, B. Dam, R. Griessen, B. J. Kooi, and J. Th. M. de Hosson. Vortex pinning by natural defects in thin films of $YBa_2Cu_3O_{7-\delta}$. *Superconductor Science and Technology*, 15(3):395, 2002.

[48] H. Wang, A. Serquis, B. Maiorov, L. Civale, Q. X. Jia, P. N. Arendt, S. R. Foltyn, J. L. MacManus-Driscoll, and X. Zhang. Microstructure and transport properties of Y-rich $YBa_2Cu_3O_{7-\delta}$ thin films. *Journal of Applied Physics*, 100(5):053904, 2006.

[49] A. Mahmood, S. D. Park, B. H. Jun, K. B. Kim, T. H. Sung, S. H. Lee, and C. J. Kim. Effect of $BaCeO_3$ addition on the microstructure and current density of melt-processed $Y_{1.5}Ba_2Cu_3O_x$ superconductors. *Physica C: Superconductivity*, 468(15-20):1355–1358, 2008.

[50] D. M. Feldmann, T. G. Holesinger, B. Maiorov, S. R. Foltyn, J. Y. Coulter, and I. Apodaca. Improved flux pinning in $YBa_2Cu_3O_7$ with nanorods of the double perovskite Ba_2YNbO_6. *Superconductor Science and Technology*, 23(9):095004, 2010.

[51] S. H. Wee, A. Goyal, E. D. Specht, C. Cantoni, Y. L. Zuev, V. Selvamanickam, and S. Cook. Enhanced flux pinning and critical current density via incorporation of self-assembled rare-earth barium tantalate nanocolumns within $YBa_2Cu_3O_{7-\delta}$ films. *Physical Review B*, 81(14):140503, 2010.

[52] C. V. Varanasi, J. Burke, L. Brunke, H. Wang, M. Sumption, and P. N. Barnes. Enhancement and angular dependence of transport critical current density in pulsed laser deposited $YBa_2Cu_3O_{7-x}$+$BaSnO_3$ films in applied magnetic fields. *Journal of Applied Physics*, 102(6): 063909, 2007.

[53] H. Tobita, K. Notoh, K. Higashikawa, M. Inoue, T. Kiss, T. Kato, T. Hirayama, M. Yoshizumi, T. Izumi, and Y. Shiohara. Fabrication of $BaHfO_3$ doped $Gd_1Ba_2Cu_3O_{7-\delta}$ coated conductors with the high ic of 85 A/cm-w under 3 t at liquid nitrogen temperature (77 k). *Superconductor Science and Technology*, 25(6):062002, 2012.

[54] V. Selvamanickam, D. W. Hazelton, L. Motowidlo, F. Krahula, J. Hoehn, M. S. Walker, and P. Haldar. High-temperature superconductors for electric power and high-energy physics. *Journal of Minerals, Metals and Materials Society*, 50(10):27–30, 1998.

[55] J. J. Shi and J. Z. Wu. Influence of the lattice strain decay on the diameter of self assembled secondary phase nanorod array in epitaxial films. *Journal of Applied Physics*, 118(16):164301, 2015.

[56] M. Peurla, P. Paturi, Y. P. Stepanov, H. Huhtinen, Y. Y. Tse, A. C.. Bódi, J. Raittila, and R. Laiho. Optimization of the $BaZrO_3$ concentration in YBCO films prepared by pulsed laser deposition. *Superconductor Science and Technology*, 19(8):767, 2006.

[57] P. Mele, K. Matsumoto, A. Ichinose, M. Mukaida, Y. Yoshida, S. Horii, and R. Kita. Systematic study of the $BaSnO_3$ insertion effect on the properties of $YBa_2Cu_3O_{7-x}$ films prepared by pulsed laser ablation. *Superconductor Science and Technology*, 21(12):125017, 2008.

[58] M. Irjala, H. Huhtinen, R. Jha, V. Awana, and P. Paturi. Optimization of the $baceo_3$ concentration in YBCO films prepared by pulsed laser deposition. *IEEE Transactions on Applied Superconductivity*, 21(3):2762–2766, 2011.

[59] H. Huhtinen, M. Irjala, P. Paturi, and M. Falter. Optimal BZO doping in YBCO films grown on single crystal STO and buffered NiW substrates. *IEEE Transactions on Applied Superconductivity*, 21(3):2753–2757, 2011.

[60] C. V. Varanasi, J. Burke, L. Brunke, H. Wang, J. H. Lee, and P. N. Barnes. Critical current density and microstructure variations in $YBa_2Cu_3O_{7-x}$+$BaSnO_3$ films with different concentrations of $BaSnO_3$. *Journal of Materials Research*, 23(12):3363–3369, 2008.

[61] F. J. Baca, T. J. Haugan, P. N. Barnes, T. G. Holesinger, B. Maiorov, R. Lu, X. Wang, J. N. Reichart, and J. Z. Wu. Interactive growth effects of rare-earth nanoparticles on nanorod formation in $YBa_2Cu_3O_x$ thin films. *Advanced Functional Materials*, 23(38):4826–4831, 2013.

[62] S. Chen, M. A. Sebastian, B. Gautam, J. Wilt, Y. Chen, L. Sun, Z. Xing, T. Haugan, and J. Wu. Generating mixed morphology $BaZrO_3$ artificial pinning centers for strong and isotropic pinning in $BaZrO_3$–Y_2O_3 double-doped YBCO thin films. *Superconductor Science and Technology*, 30 (12):125011, 2017.

[63] Y. Xu, H. L. Suo, J.-C. Grivel, M. Liu, X. Zhang, Y. Zhou, J. Liu, and Z. Zhang. Synergistic effects on the nanostrain in YBCO films double-doped with positive mismatch perovskite (Ba_2YNbO_6) and negative mismatch perovskite ($LaAlO_3$). *Crystal Growth & Design*, 20(5): 3449–3455, 2020.

[64] Y. Xu, H. Suo, T. Qureishy, J.-C. Grivel, P. Mikheenko, M. Liu, L. Ma, X. Zhang, Y. Zhou, J. Liu, L. Wang, Z. Zhang, and Q. Wang. Systematic research on the effect of both positive and negative mismatch dopants in double-doped YBCO superconducting films. *Journal of the European Ceramic Society*, 41(1):480–487, 2021.

[65] P. Paturi and H. Huhtinen. Roles of electron mean free path and flux pinning in optimizing the critical current in YBCO superconductors. *Superconductor Science and Technology*, 35(6): 065007, 2022.

[66] E. F. Talantsev and J. L. Tallon. Universal self-field critical current for thin-film superconductors. *Nature Communications*, 6(1):1–8, 2015.

[67] G. Majkic. Progress in thick film 2G-HTS development. In *Superconductivity*, pages 73–131. Springer, 2020.

[68] H. Zhou, B Maiorov, S. A. Baily, P. C. Dowden, J. A. Kennison, L. Stan, T. G. Holesinger, Q. X. Jia, S. R. Foltyn, and L. Civale. Thickness dependence of critical current density in $YBa_2Cu_3O_{7-\delta}$ films with $BaZrO_3$ and Y_2O_3 addition. *Superconductor Science and Technology*, 22(8):085013, 2009.

[69] X. Wang, F. J. Baca, R. L. S. Emergo, J. Z. Wu, T. J. Haugan, and P. N. Barnes. Eliminating thickness dependence of critical current density in $YBa_2Cu_3O_{7-x}$ films with aligned $BaZrO_3$ nanorods. *Journal of Applied Physics*, 108(11):113911, 2010.

[70] H. Huhtinen, M. Irjala, P. Paturi, and M. Falter. The effect of BZO doping concentration and thickness dependent properties of YBCO films grown by PLD on buffered NiW substrates. *Physica C: Superconductivity*, 472(1):66–74, 2012. ISSN 0921-4534.

[71] S. Holleis, I. A Shipulin, R. Hühne, J. Bernardi, and M. Eisterer. Reduced granularity in BHO-doped YBCO films on RABiTS templates. *Superconductor Science and Technology*, 35(10): 104001, 2022.

[72] R. Desfeux, J. F. Hamet, B. Mercey, C. Simon, M. Hervieu, and B. Raveau. Thin film deposition of a new cubic perovskite, $La_{4+x}Ba_{1-x}Cu_5O_{12+\delta}$ used for the realization of multilayers with YBCO. *Physica C: Superconductivity*, 221(1-2):205–214, 1994.

[73] Q. X. Jia, S. R. Foltyn, P. N. Arendt, and J. F. Smith. High-temperature superconducting thick films with enhanced supercurrent carrying capability. *Applied Physics Letters*, 80(9):1601–1603, 2002.

[74] S. R. Foltyn, H. Wang, L. Civale, Q. X. Jia, P. N. Arendt, B. Maiorov, Y. Li, M. P. Maley, and J. L. MacManus-Driscoll. Overcoming the barrier to 1000 A/cm width superconducting coatings. *Applied Physics Letters*, 87(16):162505, 2005.

[75] X. Wang and J. Z. Wu. Effect of interlayer magnetic coupling on the j_c of $YBa_2Cu_3O_7$/insulator/$YBa_2Cu_3O_7$ trilayers. *Applied Physics Letters*, 88(6):062513, 2006.

[76] S. Kang, K. J. Leonard, P. M. Martin, J. Li, and A. Goyal. Strong enhancement of flux pinning in $YBa_2Cu_3O_{7-\delta}$ multilayers with columnar defects comprised of self-assembled $BaZrO_3$ nanodots. *Superconductor Science and Technology*, 20(1):11, 2006.

[77] Y. Luo, R. A. Hughes, J. S. Preston, and G. A. Botton. Microstructure and current transport properties of single-layer $YBa_2Cu_3O_{7-x}$ and multiple-layer $YBa_2Cu_3O_{7-x}$/$(Ba_{0.05}, Sr_{0.95})TiO_3$ superconductor films. *Thin Solid Films*, 488(1):217–222, 2005. ISSN 0040-6090.

[78] Y. L. Cheung, I. P. Jones, J. S. Abell, T. W. Button, and E. F. Maher. Choice of insulating layer for YBCO in a multilayer architecture on buffered RABiTS. *Superconductor Science and Technology*, 20(3):216–221, 2007.

[79] Y. L. Cheung, E. F. Maher, J. S. Abell, I. P. Jones, and Y. Y. Tse. Microstructural study of a YBCO multilayer coated conductor cylinder. *Superconductor Science and Technology*, 20(6): 511–515, 2007.

[80] E. Backen, J. Hänisch, R. Huhne, K. Tscharntke, S. Engel, T. Thersleff, L. Schultz, and B. Holzapfel. Improved pinning in YBCO based quasi-multilayers prepared by on-and off-axis pulsed laser deposition. *IEEE Transactions on Applied Superconductivity*, 17(2):3733–3736, 2007.

[81] H. Huhtinen, K. Schlesier, and P. Paturi. Growth and c-axis flux pinning of nanostructured YBCO/BZO multilayers. *Superconductor Science and Technology*, 22(7):075019, 2009.

[82] T. J. Haugan, F. J. Baca, M. J. Mullins, N. A. Pierce, T. A. Campbell, E. L. Brewster, P. N. Barnes, H. Wang, and M. D. Sumption. Temperature and magnetic field dependence of critical current density of YBCO with varying flux pinning additions. *IEEE Transactions on Applied Superconductivity*, 19(3):3270–3274, 2009.

[83] T. S. Krylova, I. A. Chernykh, M. Y. Chernykh, E. P. Krasnoperov, and M. L. Zanaveskin. $YBa_2Cu_3O_x$-$SrTiO_3$ multilayer approach on textured Ni-W tapes: Morphology, structure and critical current density improvement. *Thin Solid Films*, 598:289–292, 2016. ISSN 0040-6090.

[84] J. Huang, L. Li, X. Wang, Z. Qi, M. A. P. Sebastian, T. J. Haugan, and H. Wang. Enhanced flux pinning properties of YBCO thin films with various pinning landscapes. *IEEE Transactions on Applied Superconductivity*, 27(4):1–5, 2016.

[85] V. Ogunjimi, M. A. Sebastian, D. Zhang, B. Gautam, J. Jian, J. Huang, Y. Zhang, T. Haugan, H. Wang, and J. Wu. Enhancing magnetic pinning by $BaZrO_3$ nanorods forming coherent interface by strain-directed Ca-doping in $YBa_2Cu_3O_{7-x}$ nanocomposite films. *Superconductor Science and Technology*, 34(10):104002, 2021.

[86] M. Panth, M. A. Sebastian, D. Zhang, V. Ogunjimi, B. Gautam, J. Jian, J. Huang, Y. Zhang, T. Haugan, H. Wang, and J. Wu. Multilayer $YBa_2Cu_3O_{7-x}$/$Ca_{0.3}YBa_2Cu_3O_{7-x}$ nanocomposite films with 2–8% $BaZrO_3$ doping for high-field applications. *IEEE Transactions on Applied Superconductivity*, 32(8):1–8, 2022.

[87] H. Kobayashi, Y. Yamada, A. Ibi, S. Miyata, Y. Shiohara, T. Kato, and T. Hirayama. Investigation of in-field properties of YBCO multi-layer film on PLD/IBAD metal substrate. *Physica C: Superconductivity and Its Applications*, 463:661–664, 2007.

[88] A. Sarkar, V. S. Dang, P. Mikheenko, M. M. Awang Kechik, J. S. Abell, and A. Crisan. Improved critical current densities in thick $YBa_2Cu_3O_{7-\delta}$ multilayer films interspaced with non-superconducting $YBa_2Cu_3O_x$ nanodots. *Thin Solid Films*, 519(2):876–879, 2010. ISSN 0040-6090. Special Section: Romanian Conference on Advanced Materials 2009.

[89] A. Usoskin and H. C. Freyhardt. YBCO-coated conductors manufactured by high-rate pulsed laser deposition. *MRS Bulletin*, 29(8):583–589, 2004.

[90] D. B. Chrisey and G. K Hubler. *Pulsed Laser Deposition of Thin Films*. John Wiley Sons, 1994.

[91] Y. Waseda, E. Matsubara, and K. Shinoda. *X-ray diffraction crystallography: introduction, examples and solved problems*. Springer Science & Business Media, 2011.

[92] W. H. Bragg and W. L. Bragg. The reflection of X-rays by crystals. *Proceedings of the Royal Society of London. Series A, Containing Papers of a Mathematical and Physical Character*, 88 (605):428–438, 1913.

[93] D. B. Williams, C. B. Carter, D. B. Williams, and C. B. C. *The transmission electron microscope*. Springer, 1996.

[94] D. Frenkel and B. Smit. *Understanding molecular simulation: from algorithms to applications*, volume 1. Elsevier, 2001.

[95] N. Metropolis, A. W. Rosenbluth, M. N. Rosenbluth, A. H. Teller, and E. Teller. Equation of state calculations by fast computing machines. *The Journal of Chemical Physics*, 21(6):1087–1092, 1953.

[96] C. P. Robert and G. Casella. *Monte Carlo statistical methods*, volume 2. Springer, 1999.

[97] E. Alpaydin. *Introduction to machine learning*. MIT press, 2020.

[98] F. Hutter, L. Kotthoff, and J. Vanschoren. *Automated machine learning: methods, systems, challenges*. Springer Nature, 2019.

[99] Y. Yeshurun and A. Malozemoff. Giant flux creep and irreversibility in an Y-Ba-Cu-O crystal: an alternative to the superconducting-glass model. *Physical Review Letters*, 60(21):2202, 1988.

[100] M. Safonchik, K. Traito, S. Tuominen, P. Paturi, H. Huhtinen, and R. Laiho. Magnetic field dependence of the optimal $BaZrO_3$ concentration in nanostructured $YBa_2Cu_3O_{7-\delta}$ films. *Superconductor Science and Technology*, 22(6):065006, 2009.

[101] P. Paturi, M. Irjala, A. B Abrahamsen, and H. Huhtinen. Defining B_c, B^* and B_ϕ for YBCO thin films. *IEEE Transactions on Applied Superconductivity*, 19(3):3431–3434, 2009.

[102] A. K. Jha, K. Matsumoto, T. Horide, S. Saini, P. Mele, A. Ichinose, Y. Yoshida, and S. Awaji. Tailoring the vortex pinning strength of YBCO thin films by systematic incorporation of hybrid artificial pinning centers. *Superconductor Science and Technology*, 28(11):114004, 2015.

[103] K. Matsumoto, T. Horide, A. K. Jha, P. Mele, Y. Yoshida, and S. Awaji. Irreversibility fields and critical current densities in strongly pinned $YBa_2Cu_3O_{7-x}$ films with artificial pinning centers. *IEEE Transactions on Applied Superconductivity*, 25(3):1–6, 2015.

[104] T. Horide, N. Matsukida, M. Ishimaru, R. Kita, S. Awaji, and K. Matsumoto. Pin potential effect on vortex pinning in $YBa_2Cu_3O_{7-\delta}$ films containing nanorods: Pin size effect and mixed pinning. *Applied Physics Letters*, 110(5):052601, 2017.

[105] L. M. Paulius, J. A. Fendrich, W.-K. Kwok, A. E. Koshelev, V. M. Vinokur, G. W. Crabtree, and B. G. Glagola. Effects of 1-GeV uranium ion irradiation on vortex pinning in single crystals of the high-temperature superconductor $YBa_2Cu_3O_{7-\delta}$. *Physical Review B*, 56(2):913, 1997.

[106] M. Malmivirta, L. D. Yao, H. Huhtinen, H. Palonen, S. Van Dijken, and P. Paturi. Three ranges of the angular dependence of critical current of $BaZrO_3$ doped $YBa_2Cu_3O_{7-\delta}$ thin films grown at different temperatures. *Thin Solid Films*, 562:554–560, 2014.

[107] S. Chen, M. A. Sebastian, B. Gautam, J. Wilt, T. Haugan, Z. Xing, and J. Wu. Enhancement of isotropic pinning force in YBCO films with $BaZrO_3$ nanorods and Y_2O_3 nanoparticles. *IEEE Transactions on Applied Superconductivity*, 27(4):1–5, 2016.

[108] J. Chen, Y. Zhou, S. Ghalsasi, I. Rusakova, and K. Salama. Study of columnar defect formation in MOD YBCO film using chemical doping. *IEEE Transactions on Applied Superconductivity*, 19(3):3254–3257, 2009.

[109] H. Yang, H. Wang, B. Maiorov, J. Lee, D. Talbayev, M. J. Hinton, D. M. Feldmann, J. L. MacManus-Driscoll, A. J. Taylor, L. Civale, T. R Lemberger, and Q. X. Jia. Self-assembled multilayers and enhanced superconductivity in $(YBa_2Cu_3O_{7-x})_{0.5}$:$(BaZrO_3)_{0.5}$ nanocomposite films. *Journal of Applied Physics*, 106(9):093914, 2009.

[110] J. He, R. F. Klie, G. Logvenov, I. Bozovic, and Y. Zhu. Microstructure and possible strain relaxation mechanisms of $La_2CuO_{4+\delta}$ thin films grown on $LaSrAlO_4$ and $SrTiO_3$ substrates. *Journal of Applied Physics*, 101(7):073906, 2007.

[111] A. Schulman, H. Palonen, V. Lähteenlahti, A. Beiranvand, H. Huhtinen, and P. Paturi. Metastable ferromagnetic flux closure-type domains in strain relaxed $Gd_{0.1}Ca_{0.9}MnO_3$ thin films. *Journal of Physics: Condensed Matter*, 33(3):035803, 2020.

[112] F. Sandiumenge, J. Santiso, L. Balcells, Z. Konstantinovic, J. Roqueta, A. Pomar, J. P. Espinós, and B. Martínez. Competing misfit relaxation mechanisms in epitaxial correlated oxides. *Physical Review Letters*, 110:107206, 2013.

[113] R. Zhao, F. Zhang, Q. Liu, Y. Xia, Y. Lu, C. Cai, J. Xiong, B. Tao, and Y. Li. MOCVD-derived multilayer $Gd_{0.5}Y_{0.5}Ba_2Cu_3O_{7-\delta}$ films based on a novel heating method. *Superconductor Science and Technology*, 30(2):025023, 2016.

[114] Y.. Chen, V. Selvamanickam, Y. Zhang, Y. Zuev, C. Cantoni, E. Specht, M. P. Paranthaman, T. Aytug, A. Goyal, and D. Lee. Enhanced flux pinning by $BaZrO_3$ and (Gd, $Y)_2O_3$ nanostructures in metal organic chemical vapor deposited GdYBCO high temperature superconductor tapes. *Applied Physics Letters*, 94(6):062513, 2009.

[115] T. G. Holesinger, B. Maiorov, O. Ugurlu, L. Civale, Y. Chen, X. Xiong, Y. Xie, and V. Selvamanickam. Microstructural and superconducting properties of high current metal–organic chemical vapor deposition $YBa_2Cu_3O_{7-\delta}$ coated conductor wires. *Superconductor Science and Technology*, 22(4):045025, 2009.

[116] H. Palonen, J. Jäykkä, and P. Paturi. Modeling reduced field dependence of critical current density in $YBa_2Cu_3O_{6+x}$ films with nanorods. *Physical Review B*, 85(2):024510, 2012.

[117] P. Paturi, M. Malmivirta, H. Palonen, and H. Huhtinen. Dopant diameter dependence of $J_c(B)$ in doped YBCO films. *IEEE Transactions on Applied Superconductivity*, 26(3):1–5, 2016.

[118] G. W. Crabtree, D. O. Gunter, H. G. Kaper, A. E. Koshelev, G. K. Leaf, and V. M. Vinokur. Numerical simulations of driven vortex systems. *Physical Review B*, 61:1446–1455, 2000.

[119] W. D. Gropp, H. G. Kaper, G. K. Leaf, D. M. Levine, M. Palumbo, and V. M. Vinokur. Numerical simulation of vortex dynamics in type-II superconductors. *Journal of Computational Physics*, 123(2):254–266, 1996.

[120] T. Winiecki and C. S. Adams. Time-dependent ginzburg-landau simulations of the voltage-current characteristic of type-II superconductors with pinning. *Physical Review B*, 65(10): 104517, 2002.

[121] U. Dobramysl, H. Assi, M. Pleimling, and U. C. Täuber. Relaxation dynamics in type-II superconductors with point-like and correlated disorder. *The European Physical Journal B*, 86(5): 1–15, 2013.

[122] H. Assi, H. Chaturvedi, U. Dobramysl, M. Pleimling, and U. C. Täuber. Relaxation dynamics of vortex lines in disordered type-II superconductors following magnetic field and temperature quenches. *Physical Review E*, 92(5):052124, 2015.

[123] H. Chaturvedi, H. Assi, U. Dobramysl, M. Pleimling, and U. C. Täuber. Flux line relaxation kinetics following current quenches in disordered type-II superconductors. *Journal of Statistical Mechanics: Theory and Experiment*, 2016(8):083301, 2016.

[124] H. Assi, H. Chaturvedi, U. Dobramysl, M. Pleimling, and U. C. Täuber. Disordered vortex matter out of equilibrium: a Langevin molecular dynamics study. *Molecular Simulation*, 42(16): 1401–1409, 2016.

[125] U. Dobramysl, M. Pleimling, and U. C. Täuber. Pinning time statistics for vortex lines in disordered environments. *Physical Review E*, 90(6):062108, 2014.

[126] M. Yazdani-Asrami, A. Sadeghi, W. Song, A. Madureira, J. Murta-Pina, A. Morandi, and M. Parizh. Artificial intelligence methods for applied superconductivity: material, design, manufacturing, testing, operation, and condition monitoring. *Superconductor Science and Technology*, 35(12):123001, 2022.

[127] W. S. Seow, R. A. Doyle, J. D. Johnson, D. Kumar, R. Somekh, D. J. C. Walker, and A. M. Campbell. The elastic regime of vortices in superconducting YBCO and multilayer YBCO/PrBCO films. *Physica C: Superconductivity*, 241(1-2):71–82, 1995.